# Theoretical description of time-resolved photoelectron momentum microscopy of ultrafast photoexcited dynamics in molecular systems

Dissertation
zur Erlangung des Doktorgrades
an der Fakultät für Mathematik, Informatik und Naturwissenschaften
Fachbereich Physik
der Universität Hamburg

vorgelegt von
Marvin Reuner

Hamburg 2023

| | |
|---|---|
| Gutachter/innen der Dissertation: | Prof. Dr. Daria Gorelova<br>Prof. Dr. Robin Santra |
| Zusammensetzung der Prüfungskommission: | Prof. Dr. Daria Gorelova<br>Prof. Dr. Robin Santra<br>Prof. Dr. Alexander Lichtenstein<br>Prof. Dr. Daniela Pfannkuche<br>Prof. Dr. Francesca Calegari |
| Vorsitzende/r der Prüfungskommission: | Prof. Dr. Daniela Pfannkuche |
| Datum der Disputation: | 04.10.2023 |
| Vorsitzender Fach-Promotionsausschuss PHYSIK: | Prof. Dr. Markus Drescher |
| Leiter des Fachbereichs PHYSIK: | Prof. Dr. Wolfgang J. Parak |
| Dekan der Fakultät MIN: | Prof. Dr.-Ing. Norbert Ritter |

## Eidesstattliche Versicherung / Declaration on oath

Hiermit versichere ich an Eides statt, die vorliegende Dissertationsschrift selbst verfasst und keine anderen als die angegebenen Hilfsmittel und Quellen benutzt zu haben.

Hamburg, den 15.11.2023 Marvin Reuner

"And all this science I don't understand It's just my job five days a week"

Elton John, *Rocket Man*

# Abstract

The recent development in photoelectron momentum microscopy, covering light pulses and measurement instruments, brought orbital tomography into the time domain. Simultaneously the development of theoretical approaches is crucial for the interpretation and explanation of the data. In addition, simulations can guide the design of these expensive experiments. I extend photoelectron momentum microscopy to image excited state properties in molecular systems from a theoretical perspective. This work aims to capture and understand the dynamics of excited isolated molecules and molecules at interfaces down to attosecond time resolution and with atomic spatial resolution.

In particular, I describe excited states of isolated molecules with *ab initio* configuration interaction calculations. I consider the broad bandwidth of the probe pulse, where the interaction with the molecular system leads to the emission of photoelectrons. I demonstrate the opportunities of this developed framework by comparing my theoretical calculations with data from two experiments performed by our collaborators.

In the first experiment, the sample is a bilayer pentacene film adsorbed on a silver substrate. My calculations reveal electronic and structural dynamics observed in the experiment up to hundreds of femtoseconds after the excitation. The second experiment involves a thin film of copper phthalocyanine on $TiSe_2$. In this case, my calculations on angle-integrated C1s core spectra and angle-resolved photoelectron distributions from the valence states of neutral and ionized CuPc gain insights into the electronic and structural properties of the sample in the experiment after excitation. Furthermore, charge transfer properties between the substrate and the molecules could be investigated.

In a purely theoretical part, I studied the possibility of photoelectron momentum microscopy for imaging charge oscillations on the attosecond timescale in neutral photoexcited molecules. In particular, I considered charge migration, described by a superposition

of excited states, in pentacene induced by a pump pulse. The photoelectrons are emitted due to the interaction with an XUV probe pulse. I demonstrate that the excited-state dynamics of a neutral pentacene molecule in real space map onto unique features of photoelectron momentum maps.

Finally, my thesis shows the potential of photoelectron momentum microscopy for imaging processes upon photoexcitation in molecular systems. The findings of this study give a deeper understanding of the dynamics in different molecular systems.

# Zusammenfassung

Die aktuellsten Verbesserungen bei ultraschnellen Lichtquellen und geeigneten Messtechniken führten zu einer Weiterentwicklung in der Impulsmikroskopie von Photoelektronen. Dies ermöglicht es neuerdings, Wellenfunktionen von Elektronenorbitalen mit einer Zeitauflösung im Femtosekunden-Bereich zu messen. Gleichzeitig sind theoretische Methoden für die Interpretation und Erklärung der Daten von entscheidender Bedeutung. Darüber hinaus helfen Simulationen, neue Experimente vorzuschlagen und diese zu gestalten. In dieser Arbeit werden Impulsverteilungen von Photoelektronen berechnet, welche aus angeregten Zuständen in molekularen Systemen ausgelöst wurden. Das Ziel dabei ist die Erfassung und das Verständnis der Dynamiken angeregter isolierter Moleküle und Molekülen an Grenzflächen mit atomarer räumlicher Auflösung und Femto/Attosekunden-Zeitauflösung.

Ich beschreibe die angeregten Zustände in den isolierten Molekülen mithilfe der Methode „Configuration Interaction“. Für die Berechnung der Impulsverteilung der ausgelösten Photoelektronen berücksichtige ich die Wechselwirkung des Systems mit einem Probepuls mit großer Bandbreite. Ich demonstriere die umfangreichen Möglichkeiten der berechneten Impulsverteilungen von Photoelektronen angeregten molekulare Systeme zu beschreiben, indem ich meine Ergebnisse mit Daten zweier Experimente vergleiche.

Im ersten Experiment wurden durch Lichtimpulse angeregte Pentacen-Moleküle untersucht, die auf einem Silbersubstrat adsorbiert waren. Meine Berechnungen führten zur Entschlüsselung der im Experiment gemessenen elektronischen und strukturellen Dynamiken. Dadurch konnten wir die Reaktion des Systems bis ca. 500 Femtosekunden nach der Anregung verfolgen.

Bei dem zweiten Experiment wurde die Anregung eines dünnen Films aus Kupferphthalocyanin (CuPc) auf $TiSe_2$ analysiert. Hierbei berechnete ich für neutrales und ionisiertes CuPc Photoelektronenspektren von 1s-Orbitalen der Kohlenstoffatome und winkelaufgelöste

Photoelektronenspektren von herausgelösten Valenzelektronen. Dies offenbart neue Einblicke in die elektronischen und strukturellen Veränderungen der Probe im Experiment nach der Anregung. Darüber hinaus konnten Ladungstransfereigenschaften zwischen dem Substrat und den Molekülen untersucht werden.

In einer theoretischen Betrachtung untersuchte ich die Möglichkeit der Impulsmikroskopie von Photoelektronen zur Abbildung von Ladungsoszillationen in neutralen angeregten Molekülen auf der Attosekunden-Zeitskala. Hierbei wurden die durch einen Anregungsimpuls induzierten Ladungsänderungen in isoliertem Pentacen betrachtet, die durch eine Überlagerung angeregter Zustände beschrieben werden. Durch die Wechselwirkung mit einem EUV-Probepuls werden Photoelektronen aus dem Pentacen herausgelöst. Ich zeige, dass die Dynamik des angeregten Zustands in dem Molekül durch die Impulsverteilungen der Photoelektronen mit atomarer räumlicher und hunderten von Attosekunden zeitlicher Auflösung verfolgt werden können.

Meine Dissertation zeigt das Potenzial der Impulsmikroskopie von Photoelektronen, um angeregte elektronische und strukturelle Prozesse in molekularen Systemen zeitlich zu verfolgen. Mithilfe dieser Technik lassen sich Dynamiken in isolierten Molekülen sowie an hybriden Grenzflächen untersuchen und verstehen.

# Acknowledgements

First, I want to thank Prof. Dr. Daria Gorelova for her great support and supervision of my work. Thanks for all your patience, good advice, and discussion during my Ph.D. Without her help, this thesis would not have been possible. Further, I thank Prof. Dr. Robin Santra for being my second supervisor and his great input. I also want to thank all people who have been involved in the work, especially Kiana Baumgärtner, Christian Metzger, and Dr. Markus Scholz, for all the great meetings where we discussed the experimental and theoretical results and many other things. I thank the PIER Graduate School for all the possibilities to get in touch with people and the courses I could participate in.

Despite all the people who have been officially involved in this work, one of my biggest thanks to Mark James Prandolini, who always had good advice for me and not only in the case of scientific topics. Thanks for all the great discussions and lunches/dinners, bike rides, and other stuff we did together and for becoming a good friend. Thank you also for your huge affords to correct the orthography of this thesis. I want to thank all the members of our working group, Nasrin Farahani, Tatiana Bezriadina, Rosmaelle Kouemo, Maksim Radionov, and Fahimeh Norouzi. Despite the working group, I want to thank all the people with whom I got in touch on the DESY campus and curing conferences, namely Benoit Richard, Christian Weigelt, Mukhtar Singh, Gaia Giovannetti, and all the others I did not explicitly name. I especially want to thank Zhangatay Nurekeyev, Yashoj Shakya and Amir Kotobi for our great times together in Hamburg. I also want to thank Mark James Prandolini, Yashoj Shakya, Kiana Baumgärtner, Tatiana Bezriadina, Maksim Radionov, Amir Kotobi, Richard Hess, Hans-Georg Babin, Patrick Ahle and Katharina Knoche for reading parts of my thesis and helping to improve the quality of the text.

Last but definitely not least, I want to thank all the people who are important to me in my life, including my family and especially my parents, who have always been there for

me since the beginning of my life and always supported me in what I was doing. I want to thank all my friends for their wonderful support and time together. All of them shaped my personality, and without them, I would not be the person I am now, whether the question is if that's a good thing.

# List of Publications

- K. Baumgärtner, M. Reuner, C. Metzger, D. Kutnyakhov, M. Heber, F. Pressacco, C.-H. Min, T. R. F. Peixoto, M. Reiser, C. Kim, W. Lu, R. Shayduk, M. Izquierdo, G. Brenner, F. Roth, A. Schöll, S. Molodtsov, W. Wurth, F. Reinert, A. Madsen, D. Popova-Gorelova, and M. Scholz, Ultrafast orbital tomography of a pentacene film using time-resolved momentum microscopy at a FEL. *Nat. Commun.* 13, 2741 (2022). https://doi.org/10.1038/s41467-022-30404-6
- M. Reuner, D. Popova-Gorelova, Attosecond imaging of photoinduced dynamics in molecules using time-resolved photoelectron momentum microscopy. *Phys. Rev. A* 107, 023101 (2023). https://link.aps.org/doi/10.1103/PhysRevA.107.023101
- K. Baumgärtner, M. Nozaki, M. Reuner, N. Wind, M. Haniuda, C. Metzger, M. Heber, D. Kutnyakhov, F. Pressacco, L. Wenthaus, K. Hara, C.-H. Min, M. Beye, F. Reinert, F. Roth, S. K. Mahatha, A. Madsen, T. Wehling, K. Niki, D. Popova-Gorelova, K. Rossnagel, M. Scholz, Multiplex movie of concerted rotation of molecules on a 2D material, *submitted* (2023) https://arxiv.org/abs/2305.07773

# Contents

# Abbrevations

| | |
|---|---|
| **AO** | atomic orbital |
| **ARPES** | angle-resolved photoemission spectroscopy |
| **BO** | Born-Oppenheimer |
| **CASSCF** | complete active space self-consistent field |
| **CDW** | charge density wave |
| **CGTO** | contracted Gaussian-type orbital |
| **CI** | configuration interaction |
| **CIS** | configuration interaction singles |
| **CSF** | configuration state function |
| **CuPc** | copper phthalocyanine |
| **DFT** | density-functional theory |
| **EDC** | energy distribution curve |
| **EKT** | extended Koopmans' theorem |
| **EM** | electromagnetic |
| **FCI** | full configuration interaction |
| **FEL** | free-electron laser |
| **GTO** | Gaussian-type orbital |
| **HF** | Hartree–Fock |
| **HHG** | high harmonic generation |
| **HOMO** | highest occupied molecular orbital |
| **LCAO** | linear combination of atomic orbitals |
| **LEED** | low-energy electron diffraction |
| **LUMO** | lowest unoccupied molecular orbital |
| **ML** | monolayer |
| **MO** | molecular orbital |

**OLED** organic light-emitting diode
**OMBE** organic molecular beam epitaxy
**OSC** organic solar cell
**PCE** power conversion efficiency
**PES** potential energy surface
**PWA** plane-wave approximation
**PMM** photoelectron momentum map
**PTCDA** perylenetetracarboxylic dianhydride
**RASCI** restricted active space configuration interaction
**RASSCF** restricted active space self-consistent field
**SD** Slater determinant
**STO** Slater-type orbital
**TDSE** time-dependent Schrödinger equation
**TISE** time-independent Schrödinger equation
**$TiSe_2$** titanium diselenide
**tr-ARPES** time- and angle-resolved photoemission spectroscopy
**tr-PMM** time-resolved photoelectron momentum map
**tr-XPD** time-resolved X-ray photoelectron diffraction
**tr-XPS** time-resolved X-ray photoelectron spectroscopy
**UV** ultraviolet
**XPS** X-ray photoelectron spectroscopy
**XUV** extreme ultraviolet

# 1. Introduction

Today semiconductors play a fundamental role in the world. Their application range from efficient light generation in light-emitting diodes (LEDs) over energy conversion in solar cells to microchips and processors in smartphones and computers. The commercial market today is dominated by inorganic semiconductors, particularly semiconductors based on silicon. However, organic semiconductors have several advantages, such as the promise of low cost in production and the ability to be used in mechanically flexible devices [1, 2, 3]. The progress in the field of organic semiconductors leads to the development of, e.g., organic light-emitting diodes (OLEDs) or flexible organic electronic devices, which are both also used in commercial products today [4, 5, 6, 7].

Organic solar cells (OSCs), which are based on organic semiconductors, until now cannot compete with the power conversion efficiency (PCE) of their inorganic counterpart [8]. However, the PCE in OSCs has increased to over 17% in recent years. [9, 10, 11]. The general working principle in both types of solar cells is similar. First, light quanta are absorbed, creating electron-hole pairs in the solar cell. Second, the design of the device leads to a separation of the excited charges. However, while in inorganic semiconductors, the excitations create free charge carriers, in organic semiconductors, the excitations create localized bound electron-hole pairs (excitons), resulting in a much lower charge carrier mobility [12, 13]. In OSCs, the excitons are separated by interaction with another organic semiconductor at the interface. Avoiding the recombination of the excitons is necessary for higher efficiency of the OSCs.

For further development of new OSCs, understanding intra- and inter-molecular interactions is important [14]. Since the involved process in the whole device is complex, it makes sense to focus on specific isolated parts ranging from the interplay at the electron donor/acceptor interface to the excitation on a single molecular level. Therefore, imaging

and understanding single molecular dynamics up to the interplay of molecules on surfaces are important.

For imaging dynamical processes, the measurement has to have a higher time resolution than the dynamics one wants to resolve. Since the first snapshot photography of a galloping horse obtained by Eadweard Muybridge in the late 19th century, technological improvements have led to the ability to image faster dynamics down to the attosecond domain, which is the timescale of electronic motions [15, 16, 17, 18, 19]. An approach for measuring such fast dynamics is a pump-probe setup, where a pump pulse brings the system out of equilibrium, and the probe pulse, at a delayed time, makes snapshots of the system. Depending on the process triggered by the probe pulse, different measuring techniques are available, e.g., photoelectron spectroscopy, photon absorption, and scattering experiments [16]. The imaging of femtosecond and attosecond dynamics was driven by the development of ultrafast light sources, such as high harmonic generation (HHG) sources [20, 21, 22, 23, 24] and free-electron lasers (FELs) [25, 26, 27, 28, 29]. With ultrashort light pulses, it is possible to follow electronic motions [30, 18, 31, 32], structural changes of the nuclei [33, 34, 35], and chemical reactions [36, 37, 38], with the goal to image a complete "molecular movie".

Different measuring techniques have been established, which allow a spatial resolution down to interatomic distances, such as time-resolved X-ray absorption spectroscopy, X-ray scattering, or detecting emitted photoelectrons, while those methods also have different subclasses. The first two techniques can also involve other photon energies while imaging material properties with X-ray pulses gives angstrom spatial resolution. For example, X-ray absorption spectroscopy measures the energy-resolved intensity change of the light pulse when it passes through a sample, giving information about core excitations into unoccupied levels in the system [39, 40, 41, 42, 43]. In X-ray scattering, the analysis of the scattered light that can originate from the relaxation of occupied levels allows the determination of sample properties [44, 37, 45, 46, 47].

The technique used in this thesis is based on photoelectron spectroscopy. In photoelectron spectroscopy, the probe pulse removes an electron from the system, which encodes information about the state of the system from which it was emitted. Compared to X-ray scattering and X-ray absorption spectroscopy, the photon energy of the probe pulse

can be much less to achieve angstrom spatial resolution because the spatial resolution is related to the de Broglie wavelength of the photoelectrons. Depending on the energy of the probe pulse, different techniques exist. In time-resolved X-ray photoelectron spectroscopy (tr-XPS) electrons are removed from the core shells, obtaining information about the atoms by the binding energy of the electrons [48, 49]. In time-resolved X-ray photoelectron diffraction (tr-XPD), the scattered three-dimensional photoelectron momentum distribution is measured, obtaining multidimensional information [50, 51, 52]. Time- and angle-resolved photoemission spectroscopy (tr-ARPES) involves probe pulses with photon energies higher than the electron binding energy in the system. This technique can measure band structures in solids [53, 54, 55, 56] and also provide information about valence states in molecules [57, 32]. For imaging valence states in molecules, orbital tomography has emerged [58]. This approach is based on the fact that the angle-resolved photoemission spectroscopy (ARPES) signal from valence states in molecules is directly related to the Fourier transformation of the molecular orbitals (MOs) if the outgoing photoelectron can be described by a plane wave [57]. Therefore for constant kinetic energies of the photoelectrons, the two-dimensional photoelectron momentum distribution (photoelectron momentum map (PMM)) is related to Fourier transformations of the MOs. The advantage of tr-ARPES is that it is sensitive to valence state dynamics relevant for OSCs, while the probe pulse energy is much less compared to X-rays.

All the techniques described above have in common that they present a time-resolved snapshot of the system. However, the interpretation of the signal can be a complicated task. In all these measurements, the phase of the probed electronic states is lost. Either phase retrieval techniques need to be applied, or theoretical calculations modeling the states of the system need to be taken into account [59, 60, 61]. In addition to the loss of phase information, the signals from different processes can be overlapped and need to be disentangled and assigned to different processes. Furthermore, if the obtained dynamics have to be related to relaxation dynamics inside the molecule, a comparison to theoretical calculations is crucial. Such experimental measurements can also be taken to test theoretical methods.

Recently orbital tomography has been extended into the time domain by measuring the momentum distribution of transiently excited electrons [32, 62, 63]. For example singlet fission has been observed on an orbital level with tr-ARPES [63], while singlet fission is the

process where an excited singlet state decays into two triplet states. This process increases the efficiency of solar cells [64]. The recent progress for imaging excited states within photoelectron momentum microscopy demonstrates the need for accurate theoretical models for interpretation of the data. Theoretically photoemission orbital tomography for excited states has been investigated very recently based on density-functional theory (DFT). In this thesis, I theoretically investigate the capabilities of tr-ARPES and tr-XPS measurements for probing photoexcited electron dynamics in molecules and molecules on surfaces. I use *ab initio* electronic structure theory (configuration interaction (CI)) for the description of the molecules.

In Ch. 2, I introduce the theoretical background for calculating ground and excited states in molecules and the description of light-matter interaction. In Ch. 3, I start with an introduction to photoemission spectroscopy. I summarize recent achievements in this field and show how to calculate the photoelectron distribution from the interaction with the probe pulse. In addition, I derive equations used in this thesis. I calculate photoelectron momentum distributions from excited states in molecules, which I implemented numerically to calculate the results of the following chapters. Moreover, I derive the difference between the electron density of the molecule in the ground state and a coherent superposition of excited states. In Ch. 4, I present my calculations on photoelectron distributions from the ground/excited states of isolated pentacene and from a model for pentacene on a substrate. The results are compared to experimentally obtained dynamics for a thin pentacene film on a substrate. In Ch. 5, I present my calculation on a different molecule, copper phthalocyanine (CuPc), where I calculate photoelectron distributions of photoelectrons emitted from excited and ionized states of the isolated molecule. I also calculate the structural properties of a mono-layer of CuPc. The results are compared to an experiment performed on a thin film of CuPc on a substrate. In Ch. 6, I present my theoretical study on imaging ultrafast photoinduced electronic charge oscillations initiated by a superposition of excited states with tr-ARPES. The opportunities of this technique are illustrated with the example molecule pentacene. With a conclusion and an outlook, I finish this thesis in Ch. 7.

# 2. Theoretical background

In this chapter, I give an overview of the theoretical approaches used in this thesis. Sec. 2.1 deals with calculating the electronic structure in molecules. I review the approach used in this thesis to calculate the ground and excited states of molecules. In Sec. 2.2, I describe the interaction between light and matter leading to the minimal coupling Hamiltonian.

Throughout the thesis, atomic units are used, where Planck's constant $\hbar$, the electron mass $m_e$, and the electron charge $e$ are $\hbar = 1$, $m_e = 1$, and $e = 1$. In this unit system, lengths are given in the unit of the Bohr radius $a_0 \approx 0.529$ Å and the energy in Hartree $E_h \approx 27.2$ eV.

## 2.1. *Ab initio* electronic structure theory

Further details on the presented and different quantum chemistry methods can be found in [65, 66].

The properties of the electrons and nuclei in molecules (containing $N_e$ electrons and $N_N$ nuclei) can be obtained by solving the non-relativistic time-dependent Schrödinger equation (TDSE). In the case of a time-independent molecular Hamiltonian, we can write down the time-independent Schrödinger equation (TISE)

$$\hat{H}_m(\mathbf{r}, \mathbf{R})\Psi(\mathbf{r}, \mathbf{R}) = E\Psi(\mathbf{r}, \mathbf{R}), \tag{2.1}$$

where $E$ is the energy of the system, $\Psi(\mathbf{r}, \mathbf{R})$ the time-independent wavefunction of the system, which depends on the coordinates $\mathbf{r}$ of the $N_e$ electrons and the coordinates $\mathbf{R}$ of the $N_N$ nuclei. The molecular Hamiltonian $\hat{H}_m$ contains the kinetic part of the electrons $\hat{T}_e(\mathbf{r})$ and the nuclei $\hat{T}_N(\mathbf{R})$ and Coulomb potential terms between electrons $\hat{V}_{ee}(\mathbf{r})$, between

nuclei $\hat{V}_{NN}(\mathbf{R})$ and between electrons and nuclei $\hat{V}_{eN}(\mathbf{r}, \mathbf{R})$

$$\hat{H}_m(\mathbf{r}, \mathbf{R}) = -\sum_{i=1}^{N_e} \frac{\nabla_{\mathbf{r}_i}^2}{2} - \sum_{I=1}^{N_N} \frac{\nabla_{\mathbf{R}_I}^2}{2M_I} + \sum_{i \neq j}^{N_e} \frac{1}{2|\mathbf{r}_i - \mathbf{r}_j|} + \sum_{I \neq J}^{N_N} \frac{Z_I Z_J}{2|\mathbf{R}_I - \mathbf{R}_J|} - \sum_{i}^{N_e} \sum_{I}^{N_N} \frac{Z_I}{|\mathbf{r}_i - \mathbf{R}_I|} \tag{2.2}$$

$$= \hat{T}_e(\mathbf{r}) + \hat{T}_N(\mathbf{R}) + \hat{V}_{ee}(\mathbf{r}) + \hat{V}_{NN}(\mathbf{R}) + \hat{V}_{eN}(\mathbf{r}, \mathbf{R}), \tag{2.3}$$

where $\nabla_{\mathbf{r}_i}$ is the nabla operator with respect to the electronic coordinate $\mathbf{r}_i$, $\nabla_{\mathbf{R}_I}$ is the nabla operator with respect to the nuclear coordinate $\mathbf{R}_I$ and $Z_I$ is the charge of the nuclei $I$. For separating the nuclear and electronic degrees of freedom in the TISE with the Hamiltonian $\hat{H}_m(\mathbf{r}, \mathbf{R})$ we first apply the Born-Oppenheimer (BO) approximation.

### 2.1.1. Born-Oppenheimer approximation

The BO approximation [67] is based on the assumption that the electrons move faster than the nuclei due to their mass being three orders of magnitude smaller. Therefore if the nuclei move, the electrons are assumed to react instantaneously (adiabatically).

To solve the Schrödinger equation, we first need a separation of the electrons and nuclei in the Schrödinger equation. Apart from the Coulomb potential term $\hat{V}_{eN}(\mathbf{r}, \mathbf{R})$ between the electrons and the nuclei, the Hamiltonian in Eq. (2.2) is already separated into a part depending on the nuclear coordinates $\hat{T}_N(\mathbf{R}) + \hat{V}_{NN}(\mathbf{R})$ and electronic coordinates $\hat{T}_e(\mathbf{r}) + \hat{V}_{ee}(\mathbf{r})$. Therefore we consider a separable ansatz for the wavefunction in the BO approximation

$$\Psi(\mathbf{r}, \mathbf{R}) = \Phi_e(\mathbf{r}; \mathbf{R}) \chi_N(\mathbf{R}), \tag{2.4}$$

where $\Phi_e(\mathbf{r}; \mathbf{R})$ is the electronic part of the wavefunction, which only parametrically depends on the nuclear coordinates $\mathbf{R}$ and $\chi_N(\mathbf{R})$ is the wavefunction of the nuclei.

With the ansatz in Eq. (2.4), the electronic Hamiltonian for a given set of nuclear positions becomes

$$\hat{H}_e = \hat{T}_e(\mathbf{r}) + \hat{V}_{eN}(\mathbf{r}, \mathbf{R}) + \hat{V}_{NN}(\mathbf{R}) + \hat{V}_{ee}(\mathbf{r}). \tag{2.5}$$

The BO approximation states that the kinetic energy of the nuclei $\hat{T}_N(\mathbf{R})$ can be neglected for solving the electronic Hamiltonian.

Finally, the BO approximation separates the TISE for the molecule into one for the electrons in Eq. (2.5) that can be solved for a given fixed set of nuclear coordinates $\mathbf{R}$

$$\hat{H}_e \Phi_e(\mathbf{r}; \mathbf{R}) = E_e \Phi_e(\mathbf{r}; \mathbf{R}). \tag{2.6}$$

For each fixed set of nuclear coordinates $\mathbf{R}$, an eigenenergy for the electronic states can be obtained with Eq. (2.6). This leads to the concept of the potential energy surfaces (PESs) (adiabatic PES in the BO approximation). The ansatz in Eq. (2.4) includes non-coupled single PESs. When the PESs of two different states become close in energy for the same nuclear coordinates, the BO approximation (adiabatic) breaks down, and non-adiabatic effects must be taken into account [68]. However, this thesis only considers adiabatic PESs in the BO approximation. With this, we have an equation to solve the electronic wavefunctions. Particular methods to solve it are presented in the next sections.

### 2.1.2. Hartree-Fock approximation

The Hartree–Fock (HF) approximation introduces a way to solve the many body problem in the TISE for the ground state of a given $N_e$-electron system. In this approach, the electron-electron interactions are considered in a mean-field approach, where each electron interacts with a mean field that results from the coulomb potential of all other electrons.

Similar to the ansatz in Eq. (2.4), the electronic wavefunction is assumed to be a product of single electronic wavefunctions, written as a Slater determinant (SD) to fulfill the anti-symmetry of the electronic wavefunction resulting from the Pauli-principle

$$\Phi_e(\mathbf{r}) = \frac{1}{\sqrt{N_e!}} \begin{vmatrix} \phi_1(\mathbf{r}_1) & \phi_2(\mathbf{r}_1) & \dots & \phi_N(\mathbf{r}_1) \\ \phi_1(\mathbf{r}_2) & \phi_2(\mathbf{r}_2) & \dots & \phi_N(\mathbf{r}_2) \\ \vdots & \vdots & \ddots & \vdots \\ \phi_1(\mathbf{r}_N) & \phi_2(\mathbf{r}_N) & \dots & \phi_N(\mathbf{r}_N) \end{vmatrix}, \tag{2.7}$$

where $N_e$ is the total number of electrons and $\phi_i(\mathbf{r}_j)$ is the $i^{\text{th}}$ one electron wavefunction (corresponding to one MO wavefunction multiplied by its spin component) with the coordinates $\mathbf{r}_j$.

With the SD approach based on single electronic wavefunctions and the Hamilton operator

in Eq. (2.5), the energy of the system is given by

$$E_e = \frac{\langle \Phi_e | \hat{H}_e | \Phi_e \rangle}{\langle \Phi_e | \Phi_e \rangle}, \tag{2.8}$$

where the wavefunction is assumed to be normalized $\langle \Phi_e | \Phi_e \rangle = 1$. The variational principle can minimize this energy while keeping the MO wavefunctions $\phi_i(\mathbf{r})$ orthogonal. This minimization leads to the HF equations which are eigenvalue equations for each electronic wavefunction

$$\hat{F}(\mathbf{r})\phi_i(\mathbf{r}) = \epsilon_i \phi_i(\mathbf{r}), \tag{2.9}$$

where $\epsilon_i$ is the energy of the electron in the orbital $i$ and $\hat{F}(\mathbf{r})$ is the Fock operator

$$\hat{F}(\mathbf{r}) = \hat{h}(\mathbf{r}) + \sum_{j}^{N_e} (\hat{J}_j(\mathbf{r}) - \hat{K}_j(\mathbf{r})), \tag{2.10}$$

with

$$\hat{h}(\mathbf{r}) = -\frac{1}{2}\nabla_{\mathbf{r}}^2 - \sum_{I}^{N_N} \frac{Z_N}{|\mathbf{r} - \mathbf{R}_I|}, \tag{2.11}$$

$$\hat{J}_j(\mathbf{r}) = \int d^3r' \, \frac{|\phi_j(\mathbf{r}')|^2}{|\mathbf{r} - \mathbf{r}'|}, \tag{2.12}$$

$$\hat{K}_j(\mathbf{r})\phi_i(\mathbf{r}) = \int d^3r' \, \frac{\phi_j^*(\mathbf{r}')\phi_i(\mathbf{r}')}{|\mathbf{r} - \mathbf{r}'|}\phi_j(\mathbf{r}). \tag{2.13}$$

In the Fock-operator $\hat{F}(\mathbf{r})$, $\hat{h}(\mathbf{r})$ is a one-electron operator describing the kinetic energy of the electrons and the Coulomb potential between the electrons and the nuclei, $\hat{J}_j(\mathbf{r})$ is the Coulomb operator and $\hat{K}_j(\mathbf{r})$ the exchange operator.

Eq. (2.9) needs to be solved with an iterative procedure (self-consistent) because the Fock-operator itself $\hat{F}(\mathbf{r})$ depends on the wavefunctions $\phi_i(\mathbf{r})$. A numerical calculation starts with an initial guess of orbital wavefunctions $\phi_i(\mathbf{r})$. With this guess, one solves Eq. (2.9) again, leading to new solutions of the wavefunctions $\phi_i(\mathbf{r})$. This procedure continues until the change in the wavefunctions is below a certain threshold and convergence is reached. If not stated otherwise, we assume a closed-shell restricted HF calculation in all our HF calculations, where the occupied orbitals are all restricted to be doubly occupied.

In the HF method, the electron-electron interactions are not treated exactly. Therefore the solution gives an upper bound to the exact energy of the system $E_{HF} \geq E_{total}$. The difference between these energies is called electron correlation energy.

### 2.1.3. Koopmans' theorem

Consider a system in the ground state described within the HF theory. Koopmans' theorem [69] relates the orbital energy $\epsilon_i$ to the energy of removing an electron from this system. The energy of the $N_e$ electron system is given in Eq. (2.8). Koopmans' theorem states that the ionization potential of the electron in orbital $i$ in this system is related to the energy of the orbital $\epsilon_i$

$$E_i^{N_e-1} - E^{N_e} = \left\langle \Phi_i^{N_e-1} \middle| \hat{H}_e \middle| \Phi_i^{N_e-1} \right\rangle - \left\langle \Phi^{N_e} \middle| \hat{H}_e \middle| \Phi^{N_e} \right\rangle = -\epsilon_i, \tag{2.14}$$

where $E_i^{N_e-1}$ is the energy of the system where the electron in orbital $i$ has been removed, with the corresponding state $\left|\Phi_i^{N_e-1}\right\rangle$. In calculations of the electronic structure of molecules, orbital energies for unoccupied orbitals are also obtained. However, Koopmans' theorem only applies to the energies of occupied orbitals.

### 2.1.4. Molecular orbitals

We can solve the electronic wavefunction with the HF method. However, we have not taken the wavefunction itself into account. This wavefunction, in principle, can be expanded in any basis set.

Here we expand the MO $\phi_i(\mathbf{r})$ in a basis of $N_{basis}$ atomic orbitals (AOs) $\varphi_i(\mathbf{r})$, leading to a linear combination of atomic orbitals (LCAO)

$$\phi_i(\mathbf{r}) = \sum_j^{N_{basis}} c_{ij}\varphi_j(\mathbf{r}), \tag{2.15}$$

where $c_{ij}$ are the expansion coefficients. The basis for the AO can be obtained from properties of atomic wavefunctions since they are located around the nuclei and decay exponentially for higher distances.

Exponential functions are analytical solutions for the wavefunction of the hydrogen atom. Therefore AO based on exponential functions, for example, Slater-type orbitals (STOs), can be a choice. However, evaluating the two-electron integrals with STO in a numerical calculation is time-consuming. Two-electron integrals have the form

$$\int d^3r_1 \int d^3r_2 \; \phi_i^*(\mathbf{r}_1)\phi_j(\mathbf{r}_1)\frac{1}{|\mathbf{r}_1 - \mathbf{r}_2|}\phi_k^*(\mathbf{r}_2)\phi_l(\mathbf{r}_2) \tag{2.16}$$

which are, e.g., necessary for evaluating the Coulomb and Exchange operator when solving Eq. (2.9). The numerical calculation involving AO based on Gaussian functions (Gaussian-type orbitals (GTOs), first proposed in 1950 [70]) has advantages in the calculation times. The GTOs in Cartesian coordinates for an atom at position $\mathbf{r}_0 = (x_0, y_0, z_0)$ are

$$g_\alpha(\mathbf{r}, l) = \frac{1}{\sqrt{N}}(x - x_0)^{l_1}(y - y_0)^{l_2}(z - z_0)^{l_3} e^{-\alpha(\mathbf{r}-\mathbf{r}_0)^2}, \tag{2.17}$$

where the sum over the variables $l = (l_1, l_2, l_3)$ define the angular momentum of the AO and $N$ is the normalization factor. However, a single GTO differs from STO, the cusp at the center of the nucleus is not given in a GTO, and the exponential decrease is much faster. Therefore a linear combination of several single GTOs (called primitive GTOs) is used to construct the so-called contracted Gaussian-type orbitals (CGTOs). With the contraction coefficients $d_{\mu,\nu}$, CGTOs are

$$\varphi_j(\mathbf{r}) = \varphi^{l(j)}_{\nu(j)}(\mathbf{r}) = \sum_\nu d_{j,\nu} g_{\alpha(\nu)}(\mathbf{r}, l), \tag{2.18}$$

where the index $j$ contains information about the index $l$ and $\nu$.

Different basis sets have been developed depending on the number of AO included for each occupied orbital in the atoms; common ones are reviewed, e.g., in [71]. The specific basis set used in this thesis is stated for each calculation.

With this introduction of the basis sets, the HF equation can be reformulated in terms of the AO. This results in the Roothaan-Haal equation for a closed-shell system [72]

$$\mathbf{FC} = \mathbf{SC}\boldsymbol{\epsilon}, \tag{2.19}$$

where $\mathbf{F}$ is the Fock matrix, the matrix $\mathbf{C}$ contains the expansion coefficients for the AO, $\mathbf{S}$ is the overlap matrix of different AO basis functions and $\boldsymbol{\epsilon}$ is the matrix with orbital energies $\epsilon_i$ on the diagonal. The coefficients $\mathbf{C}$ for the MO are obtained by solving Eq. (2.19).

### 2.1.5. Configuration interaction

HF theory can be used to calculate a closed-shell system in the ground state. However, for excited states, the single SD approach used in HF theory is generally inaccurate because the open-shell occupations lead to higher electronic correlations, which must be considered. For calculating systems where one needs to include electronic correlations, post-HF theories

have been employed, which can be used to calculate excited molecular states [73].

In CI, the wavefunction $|\Psi\rangle$ is constructed from a linear combination of electronic many-body basis states $|\Psi\rangle_n$. The many-body states $|\Psi\rangle_n$ can be constructed from the MOs obtained from a HF calculation, either as excited SD or configuration state function (CSF), which are eigenfunctions of the spin operators $\hat{S}^2$ and the projection $S_z$ (see Sec. 2.1.6). The wavefunction thus becomes

$$|\Psi\rangle = c_0 |\Phi_0\rangle + \sum_{i,a} c_i^a |\Phi_i^a\rangle + \sum_{ij,ab} c_{ij}^{ab} \left|\Phi_{ij}^{ab}\right\rangle + \dots, \tag{2.20}$$

where $|\Phi_0\rangle$ denote a wavefunction equal to the HF ground-state, in the single excited state $|\Phi_i^a\rangle$ the electron in orbital $i$ has been excited into orbital $a$, the state $\left|\Phi_{ij}^{ab}\right\rangle$ includes double excitations from orbital $i$ and $j$ into $a$ and $b$ and higher excitations are not written down explicitly. In this case, the orbitals $i, j$ and $a, b$ are singly occupied. Each state in the expansion has a specific orbital occupation. This set of occupied orbitals is called configuration. Thus we refer to the states $|\Phi_0\rangle$, $|\Phi_i^a\rangle$, $\left|\Phi_{ij}^{ab}\right\rangle$, ... as configurations. The expansion coefficients $c_0$, $c_i^a$, $c_{ij}^{ab}$, ... are obtained by minimizing the energy of the system, similar to the minimization of the energy in Eq. (2.8) carried out in the HF method.

If the expansion in the wavefunction forms a complete set of one-electron wavefunctions, the CI method leads to an exact solution of the TISE. All possible configurations from a given basis set are included in full configuration interaction (FCI). Nevertheless, dealing with a large basis set results in an intense numerical computation, therefore FCI is limited to atoms and small molecules [74, 75, 76]. Truncating the expansion space to single excitations leads to configuration interaction singles (CIS). CISD includes the expansion up to double excitations and so on.

The MOs can also be considered in different orbitals spaces. The orbitals are considered in five different spaces in the restricted active space self-consistent field (RASSCF) method [77, 78]. Orbitals in the inactive space are always doubly occupied. For orbitals in the active RAS2 space, all possible occupations are allowed. Orbitals in the RAS1 space are doubly occupied except for a maximum number of holes, while in the RAS3 space, the orbitals are unoccupied except for a maximum number of electrons. With a hole in an orbital, we mean an electronic vacancy. Orbitals in the virtual space are always unoccupied. In this thesis, we use the restricted active space configuration interaction (RASCI) method [79],

which similarly to the RASSCF method implies a restricted active space, but does not imply optimization of MOs.

The truncation of the active space in CI reduces the number of involved configurations, allowing the computation of larger molecules. In this thesis, we start from the ground state of the molecules. The excited states are obtained by performing single excitations on the ground state. This approach does not include all electronic correlations; however, they are treated in all excited states on a similar level [80, 81].

### 2.1.6. Configuration state functions

SD are eigenfunctions of the projected spin operator $\hat{S}_z$, but generally not of the total spin $\hat{S}^2$. Only for closed-shell systems (e.g., the HF ground state) and high spin states, where all the electrons in singly occupied orbitals have the same spin, the SD is an eigenfunction of the total spin operator $\hat{S}^2$ [82]. In this case, the SDs are also equal to the CSFs. CSFs are constructed as a linear combination of SDs to be eigenfunctions of both the spin projection and the total spin operator $\hat{S}_z$ and $\hat{S}^2$. The transformation between CSFs and SDs is given by the Clebsch-Gordan coefficients [82]. We explicitly derive the CSF for two and three electrons in Appendix A.1.

## 2.2. Interaction of light with matter

After discussing the electronic-structure theory for the ground and excited states of molecules, we deal with the interaction of light and matter. In this section, we derive the Hamiltonian for a system in an electromagnetic (EM) field leading to the minimal coupling Hamiltonian. With this, we can describe the system's interaction with a photoionizing probe pulse in the next section. We use the notation from [83]. Further details of the following derivations can also be found in [84, 85].

To derive the Hamiltonian we rewrite the EM field with a vector potential $\mathbf{A}$ and scalar field $\Phi$ which satisfies

$$\mathbf{E} = -\alpha \frac{\partial \mathbf{A}}{\partial t} - \nabla \Phi, \tag{2.21}$$

$$\mathbf{B} = \nabla \times \mathbf{A}, \tag{2.22}$$

where $\alpha = \frac{1}{c}$ is the fine structure constant, $\mathbf{E}$ is the electric and $\mathbf{B}$ the magnetic field. These potentials are not unique because any gauge transformation of the vector potential leaves the resulting electric and magnetic field unchanged. In the Coulomb-gauge $\nabla \cdot \mathbf{A} = 0$, and for a free EM field, we can set $\Phi = 0$. The classical energy of the EM field is

$$E_r = \frac{1}{8\pi} \int d^3r \ (\mathbf{E}^2 + \mathbf{B}^2) = \frac{1}{8\pi} \int d^3r \ \left[ \alpha^2 \left( \frac{\partial \mathbf{A}}{\partial t} \right)^2 + (\nabla \times \mathbf{A})^2 \right]. \tag{2.23}$$

This equation can be solved by expanding the vector potential in terms of modes in a cavity with volume $V$. A plane wave expansion of $\mathbf{A}$ leads to a Hamiltonian, which is a sum of uncoupled harmonic-oscillator Hamiltonians

$$\hat{H}_r = \sum_{\mathbf{k},\lambda} \omega_{\mathbf{k}} \hat{a}^\dagger_{\mathbf{k}\lambda} \hat{a}_{\mathbf{k}\lambda}, \tag{2.24}$$

where we neglected the zero-point energy. $\hat{a}^\dagger_{\mathbf{k},\lambda}(\hat{a}_{\mathbf{k},\lambda})$ creates(annihilates) a photon in the mode $(\mathbf{k}, \lambda)$, $\omega_{\mathbf{k}} = |\mathbf{k}|/\alpha$ is the energy of the photon mode with wave vector $\mathbf{k}$ and $\lambda$ is part of the polarization vector $\epsilon_{\mathbf{k},\lambda}$ of the EM field and can have the value 1 or 2. The polarization vectors are orthogonal

$$\epsilon^*_{\mathbf{k},1} \cdot \epsilon_{\mathbf{k},2} = 0, \tag{2.25}$$

and satisfies in the Coulomb gauge

$$\mathbf{k} \cdot \epsilon_{\mathbf{k},\lambda} = 0. \tag{2.26}$$

The photon creation and annihilation operators obey the commutation rules for bosons. The vector potential in the plane wave expansion in three dimensions is

$$\hat{\mathbf{A}}(\mathbf{r}) = \sum_{\mathbf{k},\lambda} \sqrt{\frac{2\pi}{V \omega_{\mathbf{k}} \alpha^2}} \left( \hat{a}_{\mathbf{k},\lambda} \boldsymbol{\epsilon}_{\mathbf{k},\lambda} e^{i\mathbf{kr}} + \hat{a}^\dagger_{\mathbf{k},\lambda} \boldsymbol{\epsilon}^*_{\mathbf{k},\lambda} e^{-i\mathbf{kr}} \right). \tag{2.27}$$

The Hamiltonian for the system interacting with a radiation field can now be obtained from the Hamiltonian of an electron

$$\hat{H}_0 = \frac{\hat{\mathbf{p}}^2}{2} + \hat{V}, \tag{2.28}$$

where $\hat{\mathbf{p}}$ is the momentum operator of an electron and $\hat{V}$ is the potential energy operator. By replacing $\hat{\mathbf{p}} \to (\hat{\mathbf{p}} - \alpha \hat{\mathbf{A}}(\mathbf{r}))$ we obtain the so-called minimal-coupling Hamilton operator

for a system interacting with an EM field, which is in the formalism of second quantization

$$\hat{H} = \hat{H}_0 + \hat{H}_r + \hat{H}_{int}, \tag{2.29}$$

$$\hat{H}_{int} = \alpha \int d^3r \; \hat{\psi}^\dagger(\mathbf{r}) \left[\hat{\mathbf{A}}(\mathbf{r}) \cdot \hat{\mathbf{p}}\right] \hat{\psi}(\mathbf{r}) + \frac{\alpha^2}{2} \int d^3r \; \hat{\psi}^\dagger(\mathbf{r}) \left[\hat{\mathbf{A}}(\mathbf{r})\right]^2 \hat{\psi}(\mathbf{r}), \tag{2.30}$$

where $\hat{\psi}^\dagger(\mathbf{r})$ is the electron creation and $\hat{\psi}(\mathbf{r})$ annihilation field operator. With the electron creation and annihilation operator $\hat{c}^\dagger_{\mu,\sigma}$ and $\hat{c}_{\mu,\sigma}$, which creates/annihilates an electron in orbital $\mu$ with spin $\sigma$, the creation and annihilation field operators are

$$\hat{\psi}^\dagger(\mathbf{r}) = \sum_{\mu,\sigma} \hat{c}^\dagger_{\mu,\sigma} \phi^*_{\mu\sigma}(\mathbf{r}), \tag{2.31}$$

$$\hat{\psi}(\mathbf{r}) = \sum_{\mu,\sigma} \hat{c}_{\mu,\sigma} \phi_{\mu\sigma}(\mathbf{r}), \tag{2.32}$$

where $\phi_{\mu\sigma}(\mathbf{r})$ is the wavefunction of the spin orbital $\mu, \sigma$.

The interaction Hamiltonian in Eq. (2.30) contains terms which are proportional to $\hat{\mathbf{A}}$ and those which are proportional to $\hat{\mathbf{A}}^2$. Both parts are discussed in detail in [83]. The vector potential $\hat{\mathbf{A}}$ changes the number of photons by one. Thus in the first order, the $\hat{\mathbf{A}}$ part describes processes where one photon is absorbed or emitted, such as photoabsorption or photoemission. In the first order, the part proportional to $\hat{\mathbf{A}}^2$ conserves the number of photons or changes them by two, which describes x-ray scattering or two-photon absorption or emission. In this thesis, we describe photoemission spectroscopy, which is triggered by one-photon absorption for our considered pulse intensities. Thus the interaction Hamiltonian reduces to

$$\hat{H}_{int} = \alpha \int d^3r \; \hat{\psi}^\dagger(\mathbf{r}) \left[\hat{\mathbf{A}}(\mathbf{r}) \cdot \hat{\mathbf{p}}\right] \hat{\psi}(\mathbf{r}). \tag{2.33}$$

# 3. Derivation of the photoelectron probability and excited state properties

In this chapter, I derive different properties needed for the rest of this thesis. In Sec. 3.1, I introduce photoelectron spectroscopy and review the theoretical description of tr-ARPES. I derive the photoelectron probability for electrons removed from different molecular states. I continue with the electron-hole density, where I calculate the difference between the electronic density of the molecule in the ground state and a coherent superposition of excited states.

## 3.1. Time- and momentum-resolved photoelectron spectroscopy

In the following section, we introduce photoelectron spectroscopy and review the derivation of the photoelectron probability for a system in a coherent superposition of states derived in [86]. We use the interaction Hamiltonian in Eq. (2.33) to describe the interaction of an ultrashort probe pulse with a system leading to the emission of photoelectrons.

### 3.1.1. Introduction

In photoemission spectroscopy (or photoelectron spectroscopy), the energy of the electrons is measured, which have been removed by a photon from a sample. It is based on the photoelectric effect, theoretically explained by Einstein in 1905 [87]. In the photoelectric effect, an electron in a sample absorbs a photon with an energy higher than the binding energy of the electron. The excited electron is removed from the system with the kinetic energy

$$\epsilon_e = \omega_{in} - E_B, \tag{3.1}$$

where $E_B$ is the binding energy of the electron in the system, which here includes the work function used in the description of solids, and $\omega_{in}$ is the energy of the light pulse. By measuring the energy of the outgoing electrons, one gets information about the energies of the occupied states in the system.

Depending on the photon energies of the light pulse (e.g., ultraviolet (UV), extreme ultraviolet (XUV), or X-ray pulses), different electrons can be removed from the system. Weaker-bound electrons in valence states contain information about, e.g., conductivity in solids or chemical bonding in molecules [88]. Stronger bound electrons in the core levels of the system can be removed with X-ray pulses leading to X-ray photoelectron spectroscopy (XPS), pioneered by Kai Siegbahn [89, 90, 91]. XPS allows obtaining information about the chemical environment of the atoms and is site specific [88, 92, 93].

Despite the binding energy, the full three-dimensional momentum of the emitted photoelectrons is measured by ARPES. Within a pump-probe setup, ARPES but also XPS can be extended to a time-resolved measurement leading to tr-ARPES and tr-XPS [86, 94, 95, 32]. ARPES measures band structures in solids [96, 97, 98] and also has been used to measure electron distributions in molecules [57, 99, 100]. Orbital tomography has emerged and allowed the mapping of MO to photoelectron momentum distributions for aligned molecules in thin films [57, 58]. Experimentally the photoelectron distribution can be measured with so-called momentum microscopes [101, 102]. In these, an objective lens creates a Fourier image of the photoelectrons from the sample in the back focal plane. The photoelectrons enter a time-of-flight drift tube after the lens (or a lens system) to obtain the photoelectron energies. Finally, a delay-line detector (DLD) measures the two-dimensional momentum of the photoelectrons. Therefore, such a time-of-flight momentum microscope detects the three-dimensional photoelectron momentum distribution. In analogy to a microscope, which creates a real space image, this technique is called momentum microscopy.

With the interaction Hamiltonian in Eq. (2.33) and the time-dependent perturbation theory, the photoelectron probability to obtain an electron with momentum $\mathbf{q}$ in the first order is (according to Fermi's golden rule [103])

$$P(\mathbf{q}) \propto \left( \langle \Psi_F(\mathbf{q}) | \, \hat{\mathbf{A}} \cdot \hat{\mathbf{p}} \, | \Psi_I \rangle \right)^2 \delta_{E_I^{N_e} + \omega_{in} - E_F^{N_e - 1}, \epsilon_e}, \tag{3.2}$$

where $|\Psi_I\rangle$ is the initial state of the system with energy $E_I^{N_e}$ before the interaction with the

light pulse (in our case, the probe pulse), $\epsilon_e$ is the energy of the outgoing photoelectron and $\langle\Psi_F(\mathbf{q})|$ is the final state after the interaction with the probe pulse with energy $E_F^{N_e-1}+\epsilon_e$. The $\delta$-function guarantees the conservation of energy. For the theoretical description of XPS, Eq. (3.2) has to be integrated over the photoelectron momentum.

For the description of the final state $\langle\Psi_F(\mathbf{q})|$ we use the sudden-approximation [104], leading to a decoupling of the molecular state after removing the photoelectron and the photoelectron wavefunction. This approximation is justified for high kinetic energies of the photoelectron emitted from free or adsorbed molecules [105].

The simplest approach for the photoelectron wavefunction is to approximate it with a plane wave, leading to the plane-wave approximation (PWA). This approximation was already proposed in the 1970s [106]. In general, the PWA could lead to incorrect results [107, 108, 109, 110] and more sophisticated methods like the independent atomic center (IAC) approximation has been developed [111]. However, it has been shown that the PWA is suitable for the emission of electrons from $\pi$-orbitals in planar molecules with light atoms (H, C, N, O), where the angle between the polarization of the probe pulse and the photoelectron momentum is small [57]. Therefore we use the PWA in this thesis.

As we will see in the derivations in Sec. 3.2, using the PWA leads to a photoelectron probability which is connected to the Fourier transform of the MOs. This led to the concept of orbital tomography, where the photoelectron momentum distribution at particular binding energies gives information about the Fourier transform of MOs [57, 60, 112, 113, 114].

### 3.1.2. Photoelectron probability involving ultrashort probe pulses

For the description of a system interacting with an ultrashort and broadband probe pulse, Eq. (3.2) is not correct, and a full quantum electrodynamic (QED) treatment of the interaction has to be taken into account [86]. We review the derivation of the photoelectron probability resulting from a system interacting with an ultrashort broadband probe pulse presented in [86] for studying charge migration dynamics. We will introduce the concept of coherent electronic motions and charge migration in Sec. 6.1.

We assume that the pump pulse triggered an excitation in the system at $t_0$. This excitation

could lead to a coherent superposition of excited states

$$|\Psi(t)\rangle = \sum_I C_I e^{-iE_I(t-t_0)} \left|\Phi_I^{N_e}\right\rangle, \tag{3.3}$$

where $\left|\Phi_I^{N_e}\right\rangle$ are eigenstates of the molecular Hamiltonian $\hat{H}_m$ with $N_e$ electrons and the corresponding energy $E_I$. We only consider excitations into spin-singlet states since the transition probability in the first order is zero for spin-triplet states. The probe pulse is assumed to not overlap with the pump pulse and can be treated separately. The Hamiltonian, including the interaction between the probe pulse and the molecule, is

$$\hat{H} = \hat{H}_m + \hat{H}_r + \hat{H}_{int}, \tag{3.4}$$

where the Hamilton operator of the probe pulse $\hat{H}_r$ is given in Eq. (2.24) and the Hamiltonian describing the interaction between the molecules and the probe pulse $\hat{H}_{int}$ in Eq. (2.33). The electronic creation and annihilation field operators are given in Eq. (2.31) and Eq. (2.32). The wavefunction of the system for a non-interacting probe pulse $\hat{H}_{int} = 0$ is

$$|\Psi_0(t)\rangle = |\Psi(t)\rangle\,|\{n\}\rangle = \sum_I C_I e^{-iE_I(t-t_0)} \left|\Phi_I^{N_e}\right\rangle |\{n\}\rangle, \tag{3.5}$$

where $|\{n\}\rangle$ is the photon state which is the eigenstate of $\hat{H}_r$. The interaction of the probe pulse is introduced with time-dependent perturbation theory. The wavefunction of the final state $\left|\Psi_f^{(1)}(t_f)\right\rangle$ at a specific time $t_f$ in first order becomes

$$\left|\Psi_{f,\{n\}}^{(1)}(t_f)\right\rangle = -i \int_{t_0}^{t_f} \mathrm{d}t\; e^{i\hat{H}_0(t-t_f)} \hat{H}_{int} e^{-i\hat{H}_0(t-t_0)} |\{n\}\rangle \sum_I C_I \left|\Phi_I^{N_e}\right\rangle, \tag{3.6}$$

where $\hat{H}_0 = \hat{H}_m + \hat{H}_r$ is the Hamiltonian of the unperturbed system. The corresponding density matrix correction in the first order is given by

$$\hat{\rho}^{(1,1)} = \sum_{\{n\},\{\tilde{n}\}} \rho^X_{\{n\},\{\tilde{n}\}} \left|\Psi_{f,\{n\}}^{(1)}(t_f)\right\rangle \left\langle \Psi_{f,\{\tilde{n}\}}^{(1)}(t_f)\right|, \tag{3.7}$$

where $\rho^X_{\{n\},\{\tilde{n}\}}$ describes the probability distribution of the modes in the incoming beam. The interaction of the molecule with the electric field leads to the emission of photoelec-

trons. Using the density matrix formalism, the photoelectron probability is

$$P = \lim_{t_f \to +t_f} \mathrm{Tr}\left[\hat{n}_{\mathbf{q}} \hat{\rho}_f^{(1,1)}(t_f)\right], \tag{3.8}$$

where $\hat{n}_{\mathbf{q}}$ is the occupation number operator for photoelectrons with momentum vector $\mathbf{q}$

$$\hat{n}_{\mathbf{q}} = \sum_{\sigma} \hat{c}^{\dagger}_{\mathbf{q},\sigma} \hat{c}_{\mathbf{q},\sigma}. \tag{3.9}$$

With Eq. (3.7) the photoelectron probability becomes

$$\begin{aligned} P = & \sum_{\sigma} \sum_{\{n\},\{\tilde{n}\}} \sum_{I,K} \rho^{X}_{\{n\},\{\tilde{n}\}} C_I C_K^{*} \sum_{F,\{n'\}} \int_{t_0}^{t_f} \mathrm{d}t_1 \int_{t_0}^{t_f} \mathrm{d}t_2 \\ & \times \left\langle \Phi_F^{N_e} \right| \hat{c}^{\dagger}_{\mathbf{q},\sigma} \hat{c}_{\mathbf{q},\sigma} \left\langle \{n'\} \right| e^{i\hat{H}_0(t_1-t_f)} \hat{H}_{int} e^{-i\hat{H}_0(t_1-t_0)} \left| \{n\} \right\rangle \left| \Phi_I^{N_e} \right\rangle \\ & \times \left\langle \Phi_K^{N_e} \right| \left\langle \{\tilde{n}\} \right| e^{i\hat{H}_0(t_2-t_0)} \hat{H}_{int} e^{-i\hat{H}_0(t_2-t_f)} \left| \{n'\} \right\rangle \left| \Phi_F^{N_e} \right\rangle. \end{aligned} \tag{3.10}$$

The probe pulse wavelength in this study is larger than the atomic scale. Therefore we use the dipole approximation $e^{-i\mathbf{kr}} \approx 1$. With $\hat{H}_{int}$ the probability results in

$$\begin{aligned} P = & \sum_{\sigma,F} \sum_{\{n\},\{\tilde{n}\}} \sum_{I,K} \rho^{X}_{\{n\}\{\tilde{n}\}} C_I C_K^{*} \sum_{\mathbf{k}_1\lambda_1,\mathbf{k}_2\lambda_2} \sum_{\{n'\}} \frac{2\pi}{V\sqrt{\omega_{\mathbf{k}_1}\omega_{\mathbf{k}_2}}} \int_{t_0}^{t_f} \mathrm{d}t_1 \int_{t_0}^{t_f} \mathrm{d}t_2 \\ & \times \left\langle \Phi_F^{N_e} \right| \left\langle \{n'\} \right| \hat{c}^{\dagger}_{\mathbf{q},\sigma} \hat{c}_{\mathbf{q},\sigma} e^{i(\hat{H}_m+\hat{H}_r)(t_1-t_f)} \left[\hat{a}_{\mathbf{k}_1,\lambda_1} \hat{T}_{\mathbf{k}_1,\lambda_1} + \hat{a}^{\dagger}_{\mathbf{k}_1,\lambda_1} \hat{T}^{\dagger}_{\mathbf{k}_1,\lambda_1}\right] \\ & \times e^{-i(\hat{H}_m+\hat{H}_r)(t_1-t_0)} \left| \{n\} \right\rangle \left| \Phi_I^{N_e} \right\rangle \\ & \times \left\langle \Phi_K^{N_e} \right| \left\langle \{\tilde{n}\} \right| e^{i(\hat{H}_m+\hat{H}_r)(t_2-t_0)} \left[\hat{a}_{\mathbf{k}_2,\lambda_2} \hat{T}_{\mathbf{k}_2,\lambda_2} + \hat{a}^{\dagger}_{\mathbf{k}_2,\lambda_2} \hat{T}^{\dagger}_{\mathbf{k}_2,\lambda_2}\right] \\ & \times e^{-i(\hat{H}_m+\hat{H}_r)(t_2-t_f)} \left| \{n'\} \right\rangle \left| \Phi_F^{N_e} \right\rangle, \end{aligned} \tag{3.11}$$

where

$$\hat{T}_{\mathbf{k},\lambda} = \int d^3r \; \hat{\psi}^{\dagger}(\mathbf{r}) \; \boldsymbol{\epsilon}_{\mathbf{k},\lambda} \mathbf{p} \; \hat{\psi}(\mathbf{r}). \tag{3.12}$$

We assume single photon absorption, which leads to the emission of the photoelectrons, thus the number of states in $|\{n'\}\rangle$ is one less compared to the number of photons in $|\{\tilde{n}\}\rangle$ and $|\{n\}\rangle$. Therefore in Eq. (3.11) the terms with $\hat{a}^{\dagger}_{\mathbf{k}_1,\lambda_1}$ and $\hat{a}_{\mathbf{k}_2,\lambda_2}$ are zero. The energies

of the photon state are

$$E_{n'} = E_r, \tag{3.13}$$

$$E_{\tilde{n}} = E_r + \omega_{\mathbf{k}_1}, \tag{3.14}$$

$$E_n = E_r + \omega_{\mathbf{k}_2}. \tag{3.15}$$

The photoelectron probability now results in

$$\begin{aligned} P = &\sum_{\sigma,F} \sum_{\{n\},\{\tilde{n}\}} \sum_{I,K} \rho^X_{\{n\}\{\tilde{n}\}} C_I C_K^* \sum_{\mathbf{k}_1\lambda_1,\mathbf{k}_2\lambda_2} \sum_{\{n'\}} \frac{2\pi}{V\sqrt{\omega_{\mathbf{k}_1}\omega_{\mathbf{k}_2}}} \int_{t_0}^{t_f} \mathrm{d}t_1 \int_{t_0}^{t_f} \mathrm{d}t_2 \\ &\times e^{-i\omega_{\mathbf{k}_1}(t_1-t_0)} e^{i\omega_{\mathbf{k}_2}(t_2-t_0)} \left\langle \{n'\} \right| \hat{a}_{\mathbf{k}_1,\lambda_1} \left| \{n\} \right\rangle \left\langle \{\tilde{n}\} \right| \hat{a}^\dagger_{\mathbf{k}_2,\lambda_2} \left| \{n'\} \right\rangle \\ &\times e^{i(E_F^{N_e-1}+\epsilon_e-E_I)(t_1-t_0)} e^{-i(E_F^{N_e-1}+\epsilon_e-E_K)(t_2-t_0)} \\ &\times \left\langle \Phi_F^{N_e} \right| \hat{c}^\dagger_{\mathbf{q},\sigma} \hat{c}_{\mathbf{q},\sigma} \hat{T}_{\mathbf{k}_1,\lambda_1} \left| \Phi_I^{N_e} \right\rangle \left\langle \Phi_K^{N_e} \right| \hat{T}^\dagger_{\mathbf{k}_2,\lambda_2} \left| \Phi_F^{N_e} \right\rangle, \end{aligned} \tag{3.16}$$

where $\epsilon_e$ is the energy of the photoelectron and $E_F^{N_e} = E_F^{N_e-1} + \epsilon_e$.

Following the argumentation in [44], we suppose an incident beam with a small spread around a mean value $\mathbf{k}_{in}$ and polarization $\boldsymbol{\epsilon}_{in}$, which leads to the assumption $\mathbf{k}_1 \approx \mathbf{k}_{in} \approx \mathbf{k}_2$ and $\boldsymbol{\epsilon}_{\mathbf{k}_1,\lambda_1} \approx \boldsymbol{\epsilon}_{in} \approx \boldsymbol{\epsilon}_{\mathbf{k}_2,\lambda_2}$. The electric field of the probe pulse has a Gaussian shape

$$E(\mathbf{r}_0, t) = \sqrt{(8\pi I_0(\mathbf{r}_0)/c)} e^{-2\ln(2)\left(\frac{t-t_p}{\tau_p}\right)^2}, \tag{3.17}$$

where $\mathbf{r}_0$ is the position, $t_p$ the arrival time of probe pulse, $\tau_p$ the pulse width and $I_0(\mathbf{r}_0) = cE^2(r_0, 0)$. Thus we can rewrite the photon expectation values as [84, 86]

$$\begin{aligned} &\frac{2\pi}{V} \sum_{\{n\},\{\tilde{n}\}} \sum_{\mathbf{k}_1\lambda_1,\mathbf{k}_2\lambda_2} \rho^X_{\{n\}\{\tilde{n}\}} \sum_{\{n'\}} \left\langle \{\tilde{n}\} \right| a^\dagger_{\mathbf{k}_2,\lambda_2} \left| \{n'\} \right\rangle e^{i\omega_{\mathbf{k}_2}(t_2-t_0)} \\ &\qquad \times \left\langle \{n'\} \right| a^\dagger_{\mathbf{k}_1,\lambda_1} \left| \{n\} \right\rangle e^{-i\omega_{\mathbf{k}_1}(t_1-t_0)} \end{aligned} \tag{3.18}$$

$$= \frac{2\pi}{V} \mathrm{Tr}\left( \hat{\rho}\ a^\dagger_{\mathbf{k}_2,\lambda_2} e^{i\omega_{\mathbf{k}_2}(t_2-t_0)} a_{\mathbf{k}_1,\lambda_1} e^{-i\omega_{\mathbf{k}_1}(t_1-t_0)} \right) \tag{3.19}$$

$$= \frac{2\pi I_0(\mathbf{r}_0)}{\omega_{in} c} e^{-2\ln 2\left(\frac{t_2-t_p}{\tau_p}\right)^2} e^{-2\ln 2\left(\frac{t_1-t_p}{\tau_p}\right)^2} e^{i\omega_{in}(t_2-t_1)}. \tag{3.20}$$

Inserting Eq. (3.20) into Eq. (3.16) leads to

$$\begin{aligned} P =& \frac{2\pi I_0(\mathbf{r}_0)}{\omega_{in}^2 c} \sum_{I,K} C_I C_K^* \sum_{\sigma,F} \left\langle \Phi_F^{N_e} \right| \hat{c}_{\mathbf{q},\sigma}^\dagger \hat{c}_{\mathbf{q},\sigma} \hat{T}_{\mathbf{k}_{in},\lambda_{in}} \left| \Phi_I^{N_e} \right\rangle \left\langle \Phi_K^{N_e} \right| \hat{T}_{\mathbf{k}_{in},\lambda_{in}}^\dagger \left| \Phi_F^{N_e} \right\rangle \\ & \times \int_{t_0}^{t_f} \mathrm{d}t_1 \; e^{-2\ln 2\left(\frac{t_1-t_p}{\tau_p}\right)^2} e^{i\tilde{\epsilon}_I(t_1-t_0)} \int_{t_0}^{t_f} \mathrm{d}t_2 \; e^{-2\ln 2\left(\frac{t_2-t_p}{\tau_p}\right)^2} e^{-i\tilde{\epsilon}_K(t_2-t_0)}, \end{aligned} \tag{3.21}$$

where $\tilde{\epsilon}_I = E_F^{N_e-1} + \epsilon_e - E_I - \omega_{in}$. The integral is

$$\begin{aligned} & \int_{t_0}^{t_f} \mathrm{d}t_1 \; e^{-2\ln 2\left(\frac{t_1-t_p}{\tau_p}\right)^2} e^{i\tilde{\epsilon}_I(t_1-t_0)} \\ & = -\frac{i\tau_p}{2}\sqrt{\frac{\pi}{\ln 4}} e^{i\tilde{\epsilon}_I(t_p-t_0)} e^{-\frac{\tau_p^2\tilde{\epsilon}_I^2}{8\ln 2}} \left[ \mathrm{erfi}\left( \frac{\tau_p^2\tilde{\epsilon}_I + 4i\ln 2(t_1-t_p)}{2\tau_p\sqrt{\ln 4}} \right) \right]_{t_0}^{t_f} \\ & = \tau_p \sqrt{\frac{\pi}{2\ln 2}} e^{i\tilde{\epsilon}_I(t_p-t_0)} e^{-\frac{\tau_p^2\tilde{\epsilon}_I^2}{8\ln 2}}. \end{aligned} \tag{3.22}$$

where it is assumed that the light pulse duration is in the range of femtoseconds, $(t_0 - t_p) < 0$ and $(t_f - t_p) > 0$ resulting in the approximation

$$\left[ \mathrm{erfi}\left( \frac{\tau_p^2\tilde{\epsilon}_I + 4i\ln 2(t_1-t_p)}{2\tau_p\sqrt{\ln 4}} \right) \right]_{t_0}^{t_f} \approx 2i. \tag{3.23}$$

Since we assume that the photoelectron and the remaining system do not interact, we can rewrite the final state $\left\langle \Phi_F^{N_e} \right| = \left\langle \Phi_F^{N_e-1} \right| \hat{c}_{\mathbf{q},\sigma}$. Therefore we obtain for the overlap of the eigenstate $\left| \Phi_I^{N_e} \right\rangle$ and the final state $\left\langle \Phi_F^{N_e} \right|$

$$\begin{aligned} \left\langle \Phi_F^{N_e} \right| \hat{T}_{\mathbf{k}_{in},\lambda_{in}} \left| \Phi_I^{N_e} \right\rangle &= \sum_\alpha \left\langle \Phi_F^{N_e-1} \right| \underbrace{\hat{c}_{\mathbf{q},\sigma}\hat{c}_\alpha^\dagger}_{\delta_{\mathbf{q},\sigma,\alpha}} \int d^3r \; \phi_\alpha^\dagger(\mathbf{r}) \; \boldsymbol{\epsilon}_{in}\mathbf{p} \; \hat{\psi}(\mathbf{r}) \left| \Phi_I^{N_e} \right\rangle \\ &= \int d^3r \; \phi_{e,\sigma}^\dagger(\mathbf{q},\mathbf{r}) \; \boldsymbol{\epsilon}_{in}\mathbf{p} \; \left\langle \Phi_F^{N_e-1} \right| \hat{\psi}(\mathbf{r}) \left| \Phi_I^{N_e} \right\rangle. \end{aligned} \tag{3.24}$$

According to Eq. (3.22) and (3.24) the probability can be written as

$$P = \frac{\pi^2\tau_p^2 I_0(\mathbf{r}_0)}{\ln 2 \omega_{in}^2 c} \sum_{\sigma,F} \left| \sum_I \nu_{I,F} \int d^3r \; \phi_{e,\sigma}^\dagger(\mathbf{q},\mathbf{r}) \; \boldsymbol{\epsilon}_{in}\mathbf{p} \; \left\langle \Phi_F^{N_e-1} \right| \hat{\psi}(\mathbf{r}) \left| C_I e^{-iE_I(t_p-t_0)} \Phi_I^{N_e} \right\rangle \right|^2, \tag{3.25}$$

$$\text{with } \nu_{I,F} = e^{-\frac{\tau_p^2}{8\ln 2}(E_F^{N_e-1}+\epsilon_e-E_I-\omega_{in})^2}.$$

If the probe pulse duration is shorter than the characteristic time of the system, we can ap-

proximate the energy $E_I$ in the factor $\nu_{I,F}$ with the mean energy of all involved eigenstates in the wavepacket in Eq. (3.3)

$$\langle E \rangle = \frac{1}{N_I} \sum_{I=1}^{N_I} E_I, \tag{3.26}$$

where $N_I$ is the number of eigenstates in the wavepacket. In this "frozen-density approximation", which only holds for a small energy splitting of the electronic states in comparison to the laser bandwidth, the photoelectron probability becomes

$$P = \frac{\pi^2 \tau_p^2 I_0(\mathbf{r}_0)}{\ln 2 \omega_{in}^2 c} \sum_{\sigma,F} \left| \nu_{m,F} \int d^3r \; \phi_{e,\sigma}^{\dagger}(\mathbf{q},\mathbf{r}) \left(\boldsymbol{\epsilon}_{in} \cdot \mathbf{p}\right) \left\langle \Phi_F^{N_e-1} \middle| \hat{\psi}(\mathbf{r}) \middle| \Psi(t_p) \right\rangle \right|^2, \tag{3.27}$$

$$\text{with } \nu_{m,F} = e^{-\frac{\tau_p^2}{8 \ln 2}\left(E_F^{N_e-1} + \epsilon_e - \langle E \rangle - \omega_{in}\right)^2}.$$

The result in Eq. (3.27) and the more general Eq. (3.25) are now depending on the initial wavefunction of the system, the final state, and the photoelectron wavefunction.

In the PWA, the photoelectron wavefunction is

$$\phi_{e,\sigma}^{\dagger}(\mathbf{q},\mathbf{r}) = \frac{1}{(2\pi)^{3/2}} e^{i\mathbf{q}\mathbf{r}} \chi_\sigma, \tag{3.28}$$

where $\chi_\sigma$ is the wavefunction of the photoelectron spin part.

For long probe pulse durations ($\frac{\tau_p}{2 \ln 2} >> 1$), the factor $\nu_{m,F}$ is approximatly a $\delta$-function. With this the photoelectron probability is [57, 115]

$$P \propto \left|\boldsymbol{\epsilon}_{in} \cdot \mathbf{q}\right|^2 \sum_{\sigma,F} \delta_{\epsilon_e, E_I^{N_e} - E_F^{N_e-1} + \omega_{in}} \left| \chi_\sigma^{\dagger} \int d^3r \; e^{-i\mathbf{q}\mathbf{r}} \phi_F^D(\mathbf{r}) \right|^2. \tag{3.29}$$

In the next chapter, we consider the ground and excited states of the molecules described within CI and evaluate the photoelectron probability for these cases in detail.

## 3.2. Distribution of photoelectrons emitted from molecules in the ground and excited state

We start with the photoelectron momentum distribution for photoelectrons emitted from the HF ground state. Afterward, we consider excited molecular states, including spin-singlet excited states, with the CI method introduced in Sec. 2.1.5. Based on these derived equations, I wrote a program that calculates the photoelectron momentum distribution

for molecular systems. The program takes the output files of the electronic structure calculation, which is performed with the software MOLCAS [116].

We use the equation for photoelectron momentum probability described in Sec. 3.1. It mainly depends on the overlap between the eigenstates of the system before $\left|\Phi_I^{N_e}\right\rangle$ and after removing the photoelectron $\left\langle\Phi_F^{N_e-1}\right|$, the so-called Dyson orbital

$$\phi_F^D(\mathbf{r}) = \left\langle\Phi_F^{N_e-1}\right| \hat{\psi}(\mathbf{r}) \left|\Phi_I^{N_e}\right\rangle . \tag{3.30}$$

Dyson orbitals are relevant for the description of photoionization processes [117]. Those already have been applied to photoionization from molecules based on different electronic structure theories (like CI or coupled cluster theory) [118, 119, 117]. Here we derive Dyson orbitals obtained from ionization of the HF ground state and excited states described within CI up to single excitation and apply them to calculate the three-dimensional photoelectron momentum distribution.

### 3.2.1. Photoelectrons emitted from the ground state

We approximate the ground state $|\Phi_0\rangle$ within the HF theory, where all orbitals are doubly occupied up to the highest occupied molecular orbital (HOMO) as shown in Fig. 3.1(A).

The wavefunction of the ground state is given by the CSF, where all orbitals up to the HOMO are doubly occupied. Since it is a closed-shell system, the CSF is equal to the SD (see Sec. 2.1.6). We describe the state starting from the occupied orbital with the lowest energy and write down each occupied orbital sorted as

$$|\Phi_0\rangle = |1\uparrow, 1\downarrow, \ldots, i\uparrow, i\downarrow, \ldots, H\uparrow, H\downarrow\rangle_{SD} = \hat{c}_{1\uparrow}^\dagger \hat{c}_{1\downarrow}^\dagger \ldots \hat{c}_{i\uparrow}^\dagger \hat{c}_{i\downarrow}^\dagger \ldots \hat{c}_{H\uparrow}^\dagger \hat{c}_{H\downarrow}^\dagger |0\rangle , \tag{3.31}$$

where $\hat{c}_{i\sigma}^\dagger$ is the creation operator for an electron in orbital $i$ with spin $\sigma$, and $|0\rangle$ is the vacuum state. $\hat{c}_{1\sigma}^\dagger$ creates an electron in the orbital with the lowest energy, while $\hat{c}_{H\sigma}^\dagger$ creates an electron in the HOMO. The anti-commutation relation of the operators contains the anti-symmetry properties of fermions.

Considering all possibilities to remove an electron from the ground state, several final states are obtained. With Koopmans' theorem (Sec. 2.1.3), the final states are described by the SD where one electron is removed from the orbital $i$ as depicted in Fig. 3.1(B) and (C), where the electron with spin down in (B) and spin up in (C) has been removed. In this

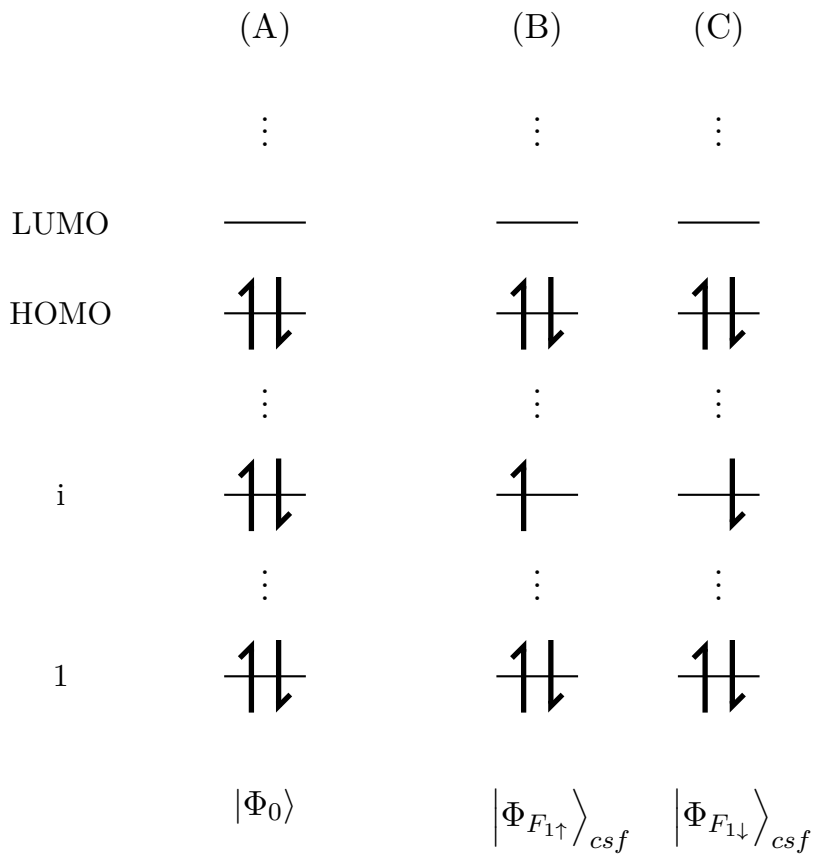


Figure 3.1.: Orbital occupation of the initial ground state (A) and the ionized final states (B)(C) in a schematic diagram.

case, the resulting CSF is again equal to the SD. The two different wavefunctions of the final states can be written as

$$|\Phi_{F_1\uparrow}\rangle_{csf} = \hat{c}^\dagger_{1\uparrow}\hat{c}^\dagger_{1\downarrow}\dots\hat{c}^\dagger_{i\uparrow}\dots\hat{c}^\dagger_{H\uparrow}\hat{c}^\dagger_{H\downarrow}\,|0\rangle = \hat{d}^\dagger_1\dots\hat{c}^\dagger_{i\uparrow}\dots\hat{d}^\dagger_H\,|0\rangle\,, \tag{3.32}$$

$$|\Phi_{F_1\downarrow}\rangle_{csf} = \hat{c}^\dagger_{1\uparrow}\hat{c}^\dagger_{1\downarrow}\dots\hat{c}^\dagger_{i\downarrow}\dots\hat{c}^\dagger_{H\uparrow}\hat{c}^\dagger_{H\downarrow}\,|0\rangle = \hat{d}^\dagger_1\dots\hat{c}^\dagger_{i\downarrow}\dots\hat{d}^\dagger_H\,|0\rangle\,, \tag{3.33}$$

where we introduced an operator for the creation of doubly occupied orbitals $\hat{d}^\dagger_i = \hat{c}^\dagger_{i\uparrow}\hat{c}^\dagger_{i\downarrow}$. This operator combines two creation operators for fermions and thus fulfills the commutation relations of bosonic operators. It commutes with other creation operators, excluding annihilation/creation operators from the same orbital. Acting on the vacuum state, the double occupation operator obeys $\langle 0|\dots\hat{d}_i\dots\hat{d}^\dagger_i\dots|0\rangle = \langle 0|\dots|0\rangle$. This relation is true if the operators in $(\dots)$ are not annihilation/creation operators of the same orbital $i$.

Now we can evaluate the Dyson orbitals involving the spin-up final state in Eq. (3.32)

$$\begin{aligned}
\langle\Phi_{F_1\uparrow}|_{csf}\,\hat{\psi}(\mathbf{r})\,|\Phi_0\rangle &= \langle 0|\,\hat{d}_H\dots\hat{c}_{i\uparrow}\dots\hat{d}_1\left(\sum_{\mu\sigma}\hat{c}_{\mu\sigma}\phi_\mu(\mathbf{r})\chi_\sigma\right)\hat{d}^\dagger_1\dots\hat{c}^\dagger_{i\uparrow}\hat{c}^\dagger_{i\downarrow}\dots\hat{d}^\dagger_H\,|0\rangle \\
&= \langle 0|\,\hat{d}_H\dots\hat{c}_{i\uparrow}\dots\hat{d}_1\hat{c}_{i\downarrow}\hat{d}^\dagger_1\dots\hat{c}^\dagger_{i\uparrow}\hat{c}^\dagger_{i\downarrow}\dots\hat{d}^\dagger_H\,|0\rangle\,\phi_i(\mathbf{r})\chi_\downarrow \\
&= -\langle 0|\,\hat{d}_H\dots\hat{c}_{i\downarrow}\hat{c}_{i\uparrow}\dots\hat{d}_1\hat{d}^\dagger_1\dots\hat{c}^\dagger_{i\uparrow}\hat{c}^\dagger_{i\downarrow}\dots\hat{d}^\dagger_H\,|0\rangle\,\phi_i(\mathbf{r})\chi_\downarrow \\
&= -\phi_i(\mathbf{r})\chi_\downarrow,
\end{aligned} \tag{3.34}$$

where the minus in the second last expression results from the different order of the creation and annihilation operators. Each term involving one particular part of the sum $\hat{c}_{\mu\sigma}\phi_\mu(\mathbf{r})\chi_\sigma$ is zero for all values of $\mu$, except if $\mu = i$, because the wavefunctions are orthogonal.

The Dyson orbital from the final state with spin down in Eq. (3.33) becomes

$$\begin{aligned}
\langle\Phi_{F_1\downarrow}|_{csf}\,\hat{\psi}(\mathbf{r})\,|\Phi_0\rangle &= \langle 0|\,\hat{d}_H\dots\hat{c}_{i\downarrow}\dots\hat{d}_1\left(\sum_{\mu\sigma}\hat{c}_{\mu\sigma}\phi_\mu(\mathbf{r})\chi_\sigma\right)\hat{d}^\dagger_1\dots\hat{c}^\dagger_{i\uparrow}\hat{c}^\dagger_{i\downarrow}\dots\hat{d}^\dagger_H\,|0\rangle \\
&= \langle 0|\,\hat{d}_H\dots\hat{c}_{i\downarrow}\dots\hat{d}_1\hat{c}_{i\uparrow}\hat{d}^\dagger_1\dots\hat{c}^\dagger_{i\uparrow}\hat{c}^\dagger_{i\downarrow}\dots\hat{d}^\dagger_H\,|0\rangle\,\phi_i(\mathbf{r})\chi_\uparrow \\
&= \langle 0|\,\hat{d}_H\dots\hat{c}_{i\uparrow}\hat{c}_{i\downarrow}\dots\hat{d}_1\hat{d}^\dagger_1\dots\hat{c}^\dagger_{i\downarrow}\hat{c}^\dagger_{i\uparrow}\dots\hat{d}^\dagger_H\,|0\rangle\,\phi_i(\mathbf{r})\chi_\uparrow \\
&= \phi_i(\mathbf{r})\chi_\uparrow.
\end{aligned} \tag{3.35}$$

Except for the minus and the spin function $\chi_\sigma$, the two calculated Dyson orbitals in Eq. (3.34) and Eq. (3.35) are the same, and are equal to a one-electron orbital wavefunction.

The energy of the initial state is the energy of the ground state $E_G$. The energy of the

final state is

$$E_{F(i)} = E_G - \epsilon_i, \tag{3.36}$$

where $\epsilon_i$ is the energy of the orbital $i$. With this, the photoelectron probability in Eq. (3.25) becomes

$$P_G(\mathbf{q}, t_p) = \frac{\tau_p^2 I_0 \left|\boldsymbol{\epsilon}_{in} \cdot \mathbf{q}\right|^2}{8\pi \ln 2 \omega_{in}^2 c} \sum_i e^{-\frac{\tau_p^2}{4\ln 2}(-\epsilon_i - \omega_{in} + \epsilon_e)^2} \left| \int d^3r \; e^{-i\mathbf{qr}} \phi_i(\mathbf{r}) \right|^2, \tag{3.37}$$

where we replaced the sum over the final states with a sum over orbitals $i$ and spin values $\sigma$. The probability of the photoelectrons emitted from the HF ground state is proportional to the sum of squared Fourier transformation orbital wavefunction. In the case where the duration of the probe pulse is long $\frac{\tau_p}{2\ln 2} >> 1$, the photoelectrons resulting from a transition to a particular final state have a sharp distribution in the energy. Thus the photoelectron probability is proportional to

$$P_G(\mathbf{q}, t_p) \propto \left|\boldsymbol{\epsilon}_{in} \cdot \mathbf{q}\right|^2 \sum_i \delta_{\omega_{in} + \epsilon_i, \epsilon_e} \left| \int d^3r \; e^{-i\mathbf{qr}} \phi_i(\mathbf{r}) \right|^2. \tag{3.38}$$

The photoelectron probability in Eq. (3.38) is similar to Fermi's golden rules. At a specific photoelectron energy, it is related to the Fourier transform of a single MO wavefunction. Therefore in such a case, a measurement of the two-dimensional photoelectron distribution at a specific photoelectron energy $\epsilon_e$ is a direct measurement of the absolute square of the Fourier-transformed orbital wavefunction. By changing the photoelectron energy $\epsilon_e$, one can obtain information about different orbitals in the system. This is used for obtaining information about the orbitals in the system in orbital tomography. In principle, one could also calculate the photoelectron distributions from unoccupied orbitals, but the interpretation of the orbital energy within Koopmans' theorem only applies to occupied orbitals.

### 3.2.2. Photoelectrons emitted from excited states

To evaluate the photoelectron probability involving excited states, we have to describe the excited state and the ionization from the excited states with the method of CI introduced in Sec. 2.1.5. Within this method, we calculate the spin-singlet excited eigenstates $|\Phi_I\rangle$ of the system by including all possible single excitations

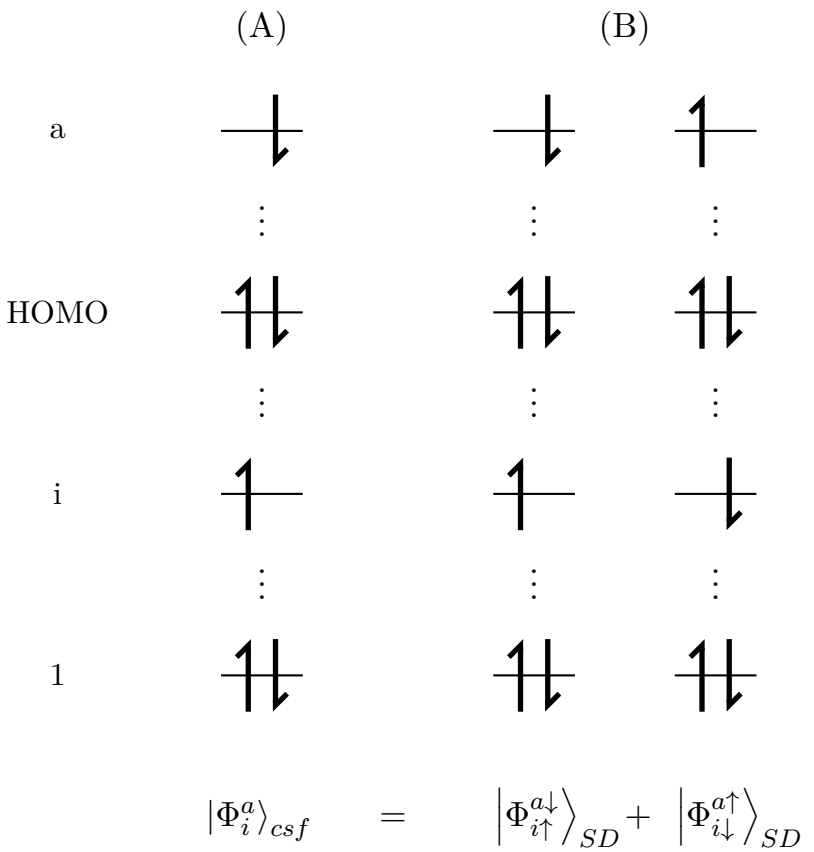


Figure 3.2.: Schematic orbital occupation of the singly excited CSFs $|\Phi_i^a\rangle_{csf}$ (A), which is a linear combination of the two SDs $\left|\Phi_{i\uparrow}^{a\downarrow}\right\rangle_{SD}$ (B) and $\left|\Phi_{i\downarrow}^{a\uparrow}\right\rangle_{SD}$ (C).

$$|\Phi_I\rangle = \sum_{i,a} c_i^a(I)\, |\Phi_i^a\rangle_{csf}\,, \tag{3.39}$$

where an electron in orbital $i$ has been excited from the HF ground state into the orbital $a$ and $c_i^a(I)$ is the expansion coefficient. The orbital occupation of the singly excited configuration $|\Phi_i^a\rangle_{csf}$ are graphically depicted in Fig. 3.2(A). According to Appendix A.1.1, the CSF, for such open-shell states, is a sum over two different SDs which are represented in Fig. 3.2(B), where the index $_{SD}$ describes a state based on a SD rather than a CSF. The two SDs differ by their spin component. Written out in an equation, the spin-singlet excited CSFs are

$$\begin{aligned} |\Phi_i^a\rangle_{csf} &= \frac{1}{\sqrt{2}} \big(|1\uparrow, 1\downarrow, \ldots, i\uparrow, \ldots, H\uparrow, H\downarrow, a\downarrow\rangle_{SD} \\ &\qquad - |1\uparrow, 1\downarrow, \ldots, i\downarrow, \ldots, H\uparrow, H\downarrow, a\uparrow\rangle_{SD}\big) \end{aligned} \tag{3.40}$$

$$= \frac{1}{\sqrt{2}} \left(\hat{d}_1^\dagger \ldots \hat{c}_{i\uparrow}^\dagger \ldots \hat{d}_H^\dagger \hat{c}_{a\downarrow}^\dagger\, |0\rangle - \hat{d}_1^\dagger \ldots \hat{c}_{i\downarrow}^\dagger \ldots \hat{d}_H^\dagger \hat{c}_{a\uparrow}^\dagger\, |0\rangle\right). \tag{3.41}$$

The final states after the photoelectron is removed are also described within CI. Those include all configurations possible by ionizing an electron from the configuration $|\Phi_i^a\rangle$ in the initial state.

We must consider different scenarios for removing electrons from the occupied orbitals in $|\Phi_i^a\rangle$. Suppose we remove the electron from the single occupied orbital above the HOMO (with index $a$). In that case, we end up in an electronic configuration that is the same as in the ionization from the ground state. Such states are given by Koopmans' theorem. This electronic configuration is shown in Fig. 3.3(A). When the electron is removed from the single occupied orbital below the lowest unoccupied molecular orbital (LUMO) (index $i$), we end up in an orbital occupation shown in Fig. 3.3(B). In the last case, the ionization of the molecule is achieved by removing one of the electrons in the initially doubly occupied orbitals. The resulting electronic configuration has three single occupied orbitals, and the state is described by two different CSF as shown in Fig. 3.3(C) and (D).

The whole final state with the spin projection value $S_z = +\frac{1}{2}$ can be written as a linear

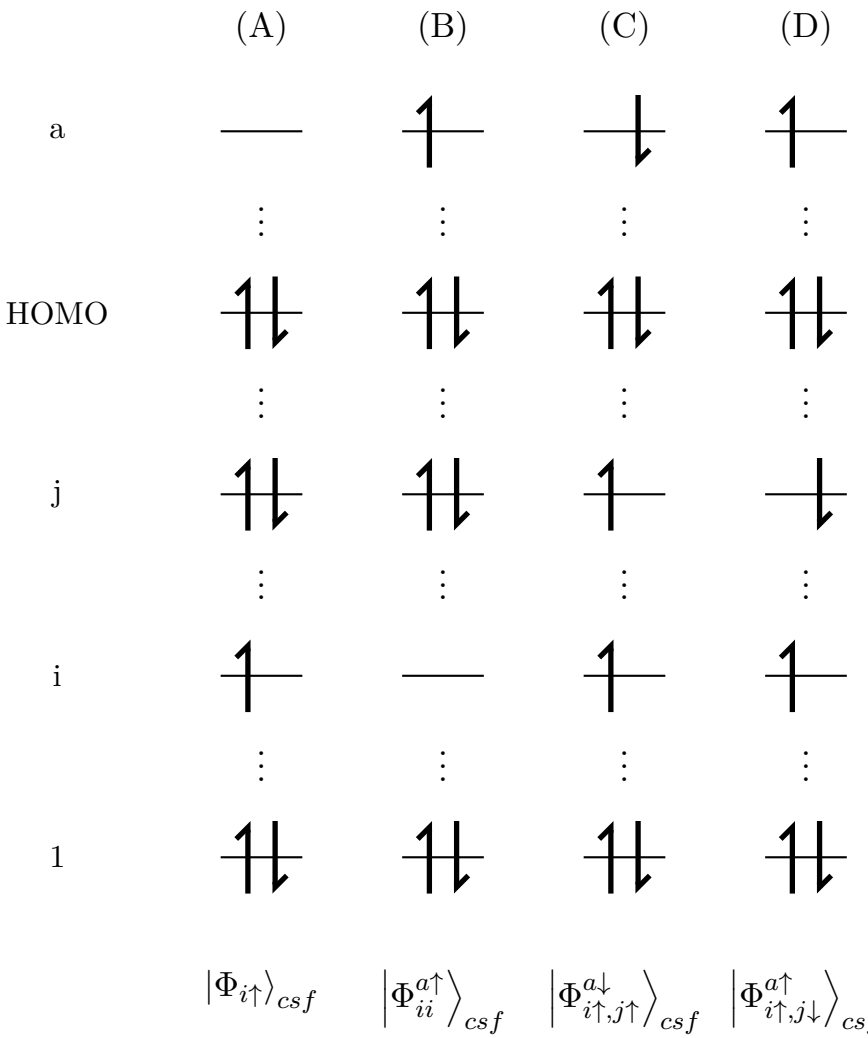


Figure 3.3.: Schematic orbital occupation of the different CSFs which are considered in the description of the final state $|\Phi_i^a\rangle_{csf}$. The orbital occupation for the configuration $|\Phi_{i\uparrow}\rangle_{csf}$ in (A), $\left|\Phi_{ii}^{a\uparrow}\right\rangle_{csf}$ in (B), $\left|\Phi_{i\uparrow,j\uparrow}^{a\downarrow}\right\rangle_{csf}$ in (C) and $\left|\Phi_{i\uparrow,j\downarrow}^{a\uparrow}\right\rangle_{csf}$ in (D).

combination of all of these discussed CSF

$$\begin{aligned}|\Phi_{F\uparrow}\rangle = &\sum_i c_i(F)\,|\Phi_{i\uparrow}\rangle_{csf} + \sum_{i,a} c_i^a(F)\left|\Phi_{ii}^{a\uparrow}\right\rangle_{csf} \\ &+ \sum_{i,j,a} c_{ij}^a(F)\left|\Phi_{i\uparrow,j\uparrow}^{a\downarrow}\right\rangle_{csf} + \sum_{i,j,a} c_{ij}^a(F)\left|\Phi_{i\uparrow,j\downarrow}^{a\uparrow}\right\rangle_{csf},\end{aligned} \tag{3.42}$$

where $\left|\Phi_{ii}^{a\uparrow}\right\rangle_{csf}$ describes a CSF where the orbital i is unoccupied. Note that in this approach, the index $i$ and $a$ can also differ from those describing the initial state.

According to Sec. 2.1.6, the CSFs in Fig. 3.3 (A) and (B) are equal to their SDs. Written out in equations these CSF for spin projection values $S_z = \pm\frac{1}{2}$ are

$$|\Phi_{i\uparrow}\rangle_{csf} = |1\uparrow, 1\downarrow, \ldots, i\uparrow, \ldots, H\uparrow, H\downarrow\rangle_{SD} = \hat{d}_1^\dagger \ldots \hat{c}_{i\uparrow}^\dagger \ldots \hat{d}_H^\dagger\,|0\rangle\,, \tag{3.43}$$

$$|\Phi_{i\downarrow}\rangle_{csf} = \hat{d}_1^\dagger \ldots \hat{c}_{i\downarrow}^\dagger \ldots \hat{d}_H^\dagger\,|0\rangle\,, \tag{3.44}$$

$$\begin{aligned}\left|\Phi_{ii}^{a\uparrow}\right\rangle_{csf} &= |1\uparrow, 1\downarrow, \ldots, i-1\uparrow, i-1\downarrow, i+1\uparrow, i+1\downarrow, \ldots, H\uparrow, H\downarrow, a\uparrow\rangle_{SD} \\ &= \hat{d}_1^\dagger \ldots \hat{d}_{i-1}^\dagger \hat{d}_{i+1}^\dagger \ldots \hat{d}_H^\dagger \hat{c}_{a\uparrow}^\dagger\,|0\rangle\,,\end{aligned} \tag{3.45}$$

$$\left|\Phi_{ii}^{a\downarrow}\right\rangle_{csf} = \hat{d}_1^\dagger \ldots \hat{d}_{i-1}^\dagger \hat{d}_{i+1}^\dagger \ldots \hat{d}_H^\dagger \hat{c}_{a\downarrow}^\dagger\,|0\rangle\,. \tag{3.46}$$

The other two CSF in Fig. 3.3 (C) and (D) are given by a sum over SDs as shown in

Appendix A.1.2 in the case where three spins couple

$$\begin{aligned}\left|\Phi^{a\downarrow}_{i\uparrow,j\uparrow}\right\rangle_{csf} &= \frac{1}{\sqrt{6}}\left[2\left|1\uparrow,1\downarrow,\ldots,i\uparrow,\ldots,j\uparrow,\ldots,H\uparrow,H\downarrow,a\downarrow\right\rangle_{SD}\right.\\ &\quad -\left|1\uparrow,1\downarrow,\ldots,i\uparrow,\ldots,j\downarrow,\ldots,H\uparrow,H\downarrow,a\uparrow\right\rangle_{SD}\\ &\quad \left.-\left|1\uparrow,1\downarrow,\ldots,i\downarrow,\ldots,j\uparrow,\ldots,H\uparrow,H\downarrow,a\uparrow\right\rangle_{SD}\right] \qquad (3.47)\\ &= \frac{1}{\sqrt{6}}\left[2(\ldots\hat{c}^\dagger_{i\uparrow}\ldots\hat{c}^\dagger_{j\uparrow}\ldots\hat{c}^\dagger_{a\downarrow})-(\ldots\hat{c}^\dagger_{i\uparrow}\ldots\hat{c}^\dagger_{j\downarrow}\ldots\hat{c}^\dagger_{a\uparrow})\right.\\ &\quad \left.-(\ldots\hat{c}^\dagger_{i\downarrow}\ldots\hat{c}^\dagger_{j\uparrow}\ldots\hat{c}^\dagger_{a\uparrow})\right]\left|0\right\rangle,\\ \left|\Phi^{a\uparrow}_{i\downarrow,j\downarrow}\right\rangle_{csf} &= -\frac{1}{\sqrt{6}}\left[2(\ldots\hat{c}^\dagger_{i\downarrow}\ldots\hat{c}^\dagger_{j\downarrow}\ldots\hat{c}^\dagger_{a\uparrow})-(\ldots\hat{c}^\dagger_{i\downarrow}\ldots\hat{c}^\dagger_{j\uparrow}\ldots\hat{c}^\dagger_{a\downarrow})\right.\\ &\quad \left.-(\ldots\hat{c}^\dagger_{i\uparrow}\ldots\hat{c}^\dagger_{j\downarrow}\ldots\hat{c}^\dagger_{a\downarrow})\right]\left|0\right\rangle, \qquad (3.48)\\ \left|\Phi^{a\uparrow}_{i\uparrow,j\downarrow}\right\rangle_{csf} &= \frac{1}{\sqrt{2}}\left[\left|1\uparrow,1\downarrow,\ldots,i\uparrow,\ldots,j\downarrow,\ldots,H\uparrow,H\downarrow,a\uparrow\right\rangle_{SD}\right.\\ &\quad \left.-\left|1\uparrow,1\downarrow,\ldots,i\downarrow,\ldots,j\uparrow,\ldots,H\uparrow,H\downarrow,a\uparrow\right\rangle_{SD}\right] \qquad (3.49)\\ &= \frac{1}{\sqrt{2}}\left[(\ldots\hat{c}^\dagger_{i\uparrow}\ldots\hat{c}^\dagger_{j\downarrow}\ldots\hat{c}^\dagger_{a\uparrow})-(\ldots\hat{c}^\dagger_{i\downarrow}\ldots\hat{c}^\dagger_{j\uparrow}\ldots\hat{c}^\dagger_{a\uparrow})\right]\left|0\right\rangle,\\ \left|\Phi^{a\downarrow}_{i\uparrow,j\downarrow}\right\rangle_{csf} &= \frac{1}{\sqrt{2}}\left[(\ldots\hat{c}^\dagger_{i\uparrow}\ldots\hat{c}^\dagger_{j\downarrow}\ldots\hat{c}^\dagger_{a\downarrow})-(\ldots\hat{c}^\dagger_{i\downarrow}\ldots\hat{c}^\dagger_{j\uparrow}\ldots\hat{c}^\dagger_{a\downarrow})\right]\left|0\right\rangle. \qquad (3.50)\end{aligned}$$

With this, we calculate the Dyson orbital between a configuration in the initial state and the different possible electronic configurations in the final state. The first Dyson orbital involves the configuration of the initial state in Eq. (3.41) and the configuration of the final state in Eq. (3.43)

$$\begin{aligned}\left\langle\Phi_{i'\uparrow}\right|_{csf}\hat{\psi}(\mathbf{r})\left|\Phi^a_i\right\rangle_{csf} = \frac{1}{\sqrt{2}}\left\langle 0\right|\hat{d}_H\ldots\hat{c}_{i'\uparrow}\ldots\hat{d}_1\left(\sum_{\mu,\sigma}\hat{c}_{\mu\sigma}\phi_\mu(\mathbf{r})\chi_\sigma\right)\\ \left(\hat{d}^\dagger_1\ldots\hat{c}^\dagger_{i\uparrow}\ldots\hat{d}^\dagger_H\hat{c}^\dagger_{a\downarrow}\left|0\right\rangle-\hat{d}^\dagger_1\ldots\hat{c}^\dagger_{i\downarrow}\ldots\hat{d}^\dagger_H\hat{c}^\dagger_{a\uparrow}\left|0\right\rangle\right).\end{aligned} \qquad (3.51)$$

Each spin-orbital must appear as a pair of creation and annihilation operators for a non-zero contribution, meaning that $i=i'$, $\mu=a$, $\sigma=\downarrow$. The matrix element thus is

$$\begin{aligned}\left\langle\Phi_{i'\uparrow}\right|_{csf}\hat{\psi}(\mathbf{r})\left|\Phi^a_i\right\rangle_{csf} &= \frac{1}{\sqrt{2}}\delta_{i,i'}\phi_a(\mathbf{r})\chi_\downarrow\left\langle 0\right|\hat{d}_H\ldots\hat{c}_{i\uparrow}\ldots\hat{d}_1\hat{c}_{a\downarrow}\hat{d}^\dagger_1\ldots\hat{c}^\dagger_{i\uparrow}\ldots\hat{d}^\dagger_H\hat{c}^\dagger_{a\downarrow}\left|0\right\rangle\\ &= -\frac{1}{\sqrt{2}}\delta_{i,i'}\phi_a(\mathbf{r})\chi_\downarrow\left\langle 0\right|\hat{c}_{a\downarrow}\hat{d}_H\ldots\hat{c}_{i\uparrow}\ldots\hat{d}^\dagger_1\hat{d}^\dagger_1\ldots\hat{c}^\dagger_{i\uparrow}\ldots\hat{d}^\dagger_H\hat{c}^\dagger_{a\downarrow}\left|0\right\rangle \qquad (3.52)\\ &= -\frac{1}{\sqrt{2}}\delta_{i,i'}\phi_a(\mathbf{r})\chi_\downarrow,\end{aligned}$$

where the minus results from the commutation of $\hat{c}_{i\uparrow}$ and $\hat{c}_{a\downarrow}$. With the two specific CSF in

Eq. (3.52), the Dyson orbital is equal to the orbital wavefunction with index $a$. Electrons in this orbital correspond to the electron the pump pulse initially photoexcited.

For the spin-down configuration in Eq. (3.44) of the final state, the Dyson orbital is

$$\begin{aligned}\langle\Phi_{i'\downarrow}|_{csf}\,\hat{\psi}(\mathbf{r})\,|\Phi_i^a\rangle_{csf} &= -\frac{1}{\sqrt{2}}\delta_{i,i'}\phi_a(\mathbf{r})\chi_\uparrow\,\langle 0|\,\hat{d}_H\ldots\hat{c}_{i\downarrow}\ldots\hat{d}_1\hat{c}_{a\uparrow}\hat{d}_1^\dagger\ldots\hat{c}_{i\downarrow}^\dagger\ldots\hat{d}_H^\dagger\hat{c}_{a\uparrow}^\dagger\,|0\rangle \\ &= \frac{1}{\sqrt{2}}\delta_{i,i'}\phi_a(\mathbf{r})\chi_\uparrow.\end{aligned} \tag{3.53}$$

With the configuration in Eq. (3.45) of the final state, we obtain the Dyson orbital

$$\begin{aligned}\left\langle\Phi_{i'i'}^{a'\uparrow}\right|_{csf}\hat{\psi}(\mathbf{r})\,|\Phi_i^a\rangle_{csf} = \frac{1}{\sqrt{2}}\,\langle 0|\,\hat{c}_{a\uparrow}\hat{d}_H\ldots\hat{d}_{i'+1}\hat{d}_{i'-1}\ldots\hat{d}_1\left(\sum_{\mu,\sigma}\hat{c}_{\mu\sigma}\phi_\mu(\mathbf{r})\chi_\sigma\right) \\ \left(\hat{d}_1^\dagger\ldots\hat{c}_{i\uparrow}^\dagger\ldots\hat{d}_H^\dagger\hat{c}_{a\downarrow}^\dagger\,|0\rangle - \hat{d}_1^\dagger\ldots\hat{c}_{i\downarrow}^\dagger\ldots\hat{d}_H^\dagger\hat{c}_{a\uparrow}^\dagger\,|0\rangle\right).\end{aligned} \tag{3.54}$$

With the same argument as in the previous evaluation $i = i'$ $a = a'$, $\mu = i$, $\sigma =\downarrow$

$$\begin{aligned}\left\langle\Phi_{i'i'}^{a'\uparrow}\right|_{csf}\hat{\psi}(\mathbf{r})\,|\Phi_i^a\rangle_{csf} &= -\frac{1}{\sqrt{2}}\delta_{a,a'}\delta_{i,i'}\phi_i(\mathbf{r})\chi_\downarrow \\ &\qquad \langle 0|\,\hat{c}_{a\uparrow}\hat{d}_H\ldots\hat{d}_{i'+1}\hat{d}_{i'-1}\ldots\hat{d}_1\hat{c}_{i\downarrow}\hat{d}_1^\dagger\ldots\hat{c}_{i\downarrow}^\dagger\ldots\hat{d}_H^\dagger\hat{c}_{a\uparrow}^\dagger\,|0\rangle \\ &= -\frac{1}{\sqrt{2}}\delta_{a,a'}\delta_{i,i'}\phi_i(\mathbf{r})\chi_\downarrow \\ &\qquad \langle 0|\,\hat{c}_{a\uparrow}\hat{d}_H\ldots\hat{d}_{i'+1}\hat{c}_{i\downarrow}\hat{d}_{i'-1}\ldots\hat{d}_1\hat{d}_1^\dagger\ldots\hat{c}_{i\downarrow}^\dagger\ldots\hat{d}_H^\dagger\hat{c}_{a\uparrow}^\dagger\,|0\rangle \\ &= -\frac{1}{\sqrt{2}}\delta_{a,a'}\delta_{i,i'}\phi_i(\mathbf{r})\chi_\downarrow.\end{aligned} \tag{3.55}$$

For the configuration in Eq. (3.46) of the final state with spin down, we get the Dyson orbital

$$\begin{aligned}\left\langle\Phi_{i'i'}^{a'\downarrow}\right|_{csf}\hat{\psi}(\mathbf{r})\,|\Phi_i^a\rangle_{csf} &= \frac{1}{\sqrt{2}}\delta_{a,a'}\delta_{i,i'}\phi_i(\mathbf{r})\chi_\uparrow \\ &\qquad \langle 0|\,\hat{c}_{a\uparrow}\hat{d}_H\ldots\hat{d}_{i'+1}\hat{d}_{i'-1}\ldots\hat{d}_1\hat{c}_{i\uparrow}\hat{d}_1^\dagger\ldots\hat{c}_{i\downarrow}^\dagger\ldots\hat{d}_H^\dagger\hat{c}_{a\uparrow}^\dagger\,|0\rangle \\ &= \frac{1}{\sqrt{2}}\delta_{a,a'}\delta_{i,i'}\phi_i(\mathbf{r})\chi_\uparrow \\ &\qquad \langle 0|\,\hat{c}_{a\uparrow}\hat{d}_H\ldots\hat{d}_{i'+1}\hat{c}_{i\uparrow}\hat{d}_{i'-1}\ldots\hat{d}_1\hat{d}_1^\dagger\ldots\hat{c}_{i\downarrow}^\dagger\ldots\hat{d}_H^\dagger\hat{c}_{a\uparrow}^\dagger\,|0\rangle \\ &= \frac{1}{\sqrt{2}}\delta_{a,a'}\delta_{i,i'}\phi_i(\mathbf{r})\chi_\uparrow.\end{aligned} \tag{3.56}$$

Now we deal with the configurations of the final state, which has three singly occupied

orbitals. For the first one in Eq. (3.47) the Dyson orbital is

$$\begin{aligned}\left\langle \Phi^{a'\downarrow}_{i'\uparrow,j'\uparrow}\right|_{csf}\hat{\psi}(\mathbf{r})\left|\Phi^{a}_{i}\right\rangle_{csf} = \frac{1}{\sqrt{12}}\langle 0|\,[2(\hat{c}_{a'\downarrow}\dots\hat{c}_{j'\uparrow}\dots\hat{c}_{i'\uparrow}\dots)-(\hat{c}_{a'\uparrow}\dots\hat{c}_{j'\downarrow}\dots\hat{c}_{i'\uparrow}\dots)\\ -(\hat{c}_{a'\uparrow}\dots\hat{c}_{j'\uparrow}\dots\hat{c}_{i'\downarrow}\dots)]\left(\sum_{\mu,\sigma}\hat{c}_{\mu\sigma}\phi_{\mu}(\mathbf{r})\chi_{\sigma}\right)\\ \left[\left(\dots\hat{c}^{\dagger}_{i\uparrow}\dots\hat{c}^{\dagger}_{a\downarrow}\right)-\left(\dots\hat{c}^{\dagger}_{i\downarrow}\dots\hat{c}^{\dagger}_{a\uparrow}\right)\right]|0\rangle\,,\end{aligned} \tag{3.57}$$

where from now on we did not write down $\hat{d}^{\dagger}_{1}$ and $\hat{d}^{\dagger}_{H}$ explicitly. For a non-zero contribution, the configurations in the initial and final state must share the same orbital index of the excited electron $a = a'$

$$\begin{aligned}&\left\langle \Phi^{a'\downarrow}_{i'\uparrow,j'\uparrow}\right|_{csf}\hat{\psi}(\mathbf{r})\left|\Phi^{a}_{i}\right\rangle_{csf} =\\ &\frac{1}{\sqrt{12}}\delta_{a,a'}\langle 0|\left[2(\hat{c}_{a\downarrow}\dots\hat{c}_{j'\uparrow}\dots\hat{c}_{i'\uparrow}\dots)\left(\sum_{\mu,\sigma}\hat{c}_{\mu\sigma}\phi_{\mu}(\mathbf{r})\chi_{\sigma}\right)\left(\dots\hat{c}^{\dagger}_{i\uparrow}\dots\hat{c}^{\dagger}_{a\downarrow}\right)\right.\\ &\quad+(\hat{c}_{a\uparrow}\dots\hat{c}_{j'\downarrow}\dots\hat{c}_{i'\uparrow}\dots)\left(\sum_{\mu,\sigma}\hat{c}_{\mu\sigma}\phi_{\mu}(\mathbf{r})\chi_{\sigma}\right)\left(\dots\hat{c}^{\dagger}_{i\downarrow}\dots\hat{c}^{\dagger}_{a\uparrow}\right)\\ &\quad\left.+(\hat{c}_{a\uparrow}\dots\hat{c}_{j'\uparrow}\dots\hat{c}_{i'\downarrow}\dots)\left(\sum_{\mu,\sigma}\hat{c}_{\mu\sigma}\phi_{\mu}(\mathbf{r})\chi_{\sigma}\right)\left(\dots\hat{c}^{\dagger}_{i\downarrow}\dots\hat{c}^{\dagger}_{a\uparrow}\right)\right]|0\rangle\,.\end{aligned} \tag{3.58}$$

Now we consider two different cases. In the first one, $\mu = i'$, and in the second, $\mu = j'$. These cases lead to different relations between $i$ and $i', j'$

$$\begin{aligned}&\left\langle \Phi^{a'\downarrow}_{i'\uparrow,j'\uparrow}\right|_{csf}\hat{\psi}(\mathbf{r})\left|\Phi^{a}_{i}\right\rangle_{csf} =\\ &\quad\frac{1}{\sqrt{12}}\delta_{a,a'}\phi_{i'}(\mathbf{r})\chi_{\downarrow}\langle 0|\left[2(\hat{c}_{a\downarrow}\dots\hat{c}_{j'\uparrow}\dots\hat{c}_{i'\uparrow}\dots)\hat{c}_{i'\downarrow}\left(\dots\hat{c}^{\dagger}_{i\uparrow}\dots\hat{c}^{\dagger}_{a\downarrow}\right)\right.\\ &\qquad+(\hat{c}_{a\uparrow}\dots\hat{c}_{j'\downarrow}\dots\hat{c}_{i'\uparrow}\dots)\hat{c}_{i'\downarrow}\left(\dots\hat{c}^{\dagger}_{i\downarrow}\dots\hat{c}^{\dagger}_{a\uparrow}\right)\\ &\qquad\left.+(\hat{c}_{a\uparrow}\dots\hat{c}_{j'\uparrow}\dots\hat{c}_{i'\downarrow}\dots)\hat{c}_{i'\downarrow}\left(\dots\hat{c}^{\dagger}_{i\downarrow}\dots\hat{c}^{\dagger}_{a\uparrow}\right)\right]|0\rangle\\ &+\frac{1}{\sqrt{12}}\delta_{a,a'}\phi_{j'}(\mathbf{r})\chi_{\downarrow}\langle 0|\left[2(\hat{c}_{a\downarrow}\dots\hat{c}_{j'\uparrow}\dots\hat{c}_{i'\uparrow}\dots)\hat{c}_{j'\downarrow}\left(\dots\hat{c}^{\dagger}_{i\uparrow}\dots\hat{c}^{\dagger}_{a\downarrow}\right)\right.\\ &\qquad+(\hat{c}_{a\uparrow}\dots\hat{c}_{j'\downarrow}\dots\hat{c}_{i'\uparrow}\dots)\hat{c}_{j'\downarrow}\left(\dots\hat{c}^{\dagger}_{i\downarrow}\dots\hat{c}^{\dagger}_{a\uparrow}\right)\\ &\qquad\left.+(\hat{c}_{a\uparrow}\dots\hat{c}_{j'\uparrow}\dots\hat{c}_{i'\downarrow}\dots)\hat{c}_{j'\downarrow}\left(\dots\hat{c}^{\dagger}_{i\downarrow}\dots\hat{c}^{\dagger}_{a\uparrow}\right)\right]|0\rangle\,.\end{aligned} \tag{3.59}$$

The parts in the sum which contain two times the same annihilation operator are zero.

Considering that either $i' = i$ or $j' = i$ we obtain

$$
\begin{aligned}
&\left\langle \Phi^{a'\downarrow}_{i'\uparrow,j'\uparrow}\right|_{csf} \hat{\psi}(\mathbf{r}) \left|\Phi^{a}_{i}\right\rangle_{csf} = \\
&= \frac{1}{\sqrt{12}}\delta_{a,a'}\delta_{i,j'}\phi_{i'}(\mathbf{r})\chi_{\downarrow} \langle 0| \left[2(\hat{c}_{a\downarrow}\dots\hat{c}_{j'\uparrow}\dots\hat{c}_{i'\uparrow}\dots)\hat{c}_{i'\downarrow}\left(\dots\hat{c}^{\dagger}_{i\uparrow}\dots\hat{c}^{\dagger}_{a\downarrow}\right)\right. \\
&\qquad\qquad \left. +(\hat{c}_{a\uparrow}\dots\hat{c}_{j'\downarrow}\dots\hat{c}_{i'\uparrow}\dots)\hat{c}_{i'\downarrow}\left(\dots\hat{c}^{\dagger}_{i\downarrow}\dots\hat{c}^{\dagger}_{a\uparrow}\right)\right]|0\rangle \\
&\quad + \frac{1}{\sqrt{12}}\delta_{a,a'}\delta_{i,i'}\phi_{j'}(\mathbf{r})\chi_{\downarrow} \langle 0| \left[2(\hat{c}_{a\downarrow}\dots\hat{c}_{j'\uparrow}\dots\hat{c}_{i'\uparrow}\dots)\hat{c}_{j'\downarrow}\left(\dots\hat{c}^{\dagger}_{i\uparrow}\dots\hat{c}^{\dagger}_{a\downarrow}\right)\right. \\
&\qquad\qquad \left. +(\hat{c}_{a\uparrow}\dots\hat{c}_{j'\uparrow}\dots\hat{c}_{i'\downarrow}\dots)\hat{c}_{j'\downarrow}\left(\dots\hat{c}^{\dagger}_{i\downarrow}\dots\hat{c}^{\dagger}_{a\uparrow}\right)\right]|0\rangle . \\
&= -\frac{1}{\sqrt{12}}\delta_{a,a'}\delta_{i,j'}\phi_{i'}(\mathbf{r})\chi_{\downarrow} \langle 0| \left[2(\hat{c}_{a\downarrow}\dots\hat{c}_{i\uparrow}\dots\hat{c}_{i'\downarrow}\hat{c}_{i'\uparrow}\dots)\left(\dots\hat{c}^{\dagger}_{i\uparrow}\dots\hat{c}^{\dagger}_{a\downarrow}\right)\right. \\
&\qquad\qquad \left. +(\hat{c}_{a\uparrow}\dots\hat{c}_{i\downarrow}\dots\hat{c}_{i'\downarrow}\hat{c}_{i'\uparrow}\dots)\left(\dots\hat{c}^{\dagger}_{i\downarrow}\dots\hat{c}^{\dagger}_{a\uparrow}\right)\right]|0\rangle \\
&\quad + \frac{1}{\sqrt{12}}\delta_{a,a'}\delta_{i,i'}\phi_{j'}(\mathbf{r})\chi_{\downarrow} \langle 0| \left[2(\hat{c}_{a\downarrow}\dots\hat{c}_{j'\downarrow}\hat{c}_{j'\uparrow}\dots\hat{c}_{i\uparrow}\dots)\left(\dots\hat{c}^{\dagger}_{i\uparrow}\dots\hat{c}^{\dagger}_{a\downarrow}\right)\right. \\
&\qquad\qquad \left. +(\hat{c}_{a\uparrow}\dots\hat{c}_{j'\downarrow}\hat{c}_{j'\uparrow}\dots\hat{c}_{i\downarrow}\dots)\left(\dots\hat{c}^{\dagger}_{i\downarrow}\dots\hat{c}^{\dagger}_{a\uparrow}\right)\right]|0\rangle . \\
&= -\frac{\sqrt{3}}{2}\delta_{a,a'}\delta_{i,j'}\phi_{i'}(\mathbf{r})\chi_{\downarrow} + \frac{\sqrt{3}}{2}\delta_{a,a'}\delta_{i,i'}\phi_{j'}(\mathbf{r})\chi_{\downarrow}.
\end{aligned}
\tag{3.60}
$$

These results show that the sign of the MO wavefunction in the Dyson orbital is different if $i' = i$ or $j' = i$.

The evaluation of the Dyson orbital resulting from the configuration in Eq. (3.48) of the final state is similar to the latter and only differs by the spin value

$$
\begin{aligned}
&\left\langle \Phi^{a'\uparrow}_{i'\downarrow,j'\downarrow}\right|_{csf} \hat{\psi}(\mathbf{r}) \left|\Phi^{a}_{i}\right\rangle_{csf} = \\
&\qquad = -\frac{1}{\sqrt{12}} \langle 0| \left[2(\hat{c}_{a'\uparrow}\dots\hat{c}_{j'\downarrow}\dots\hat{c}_{i'\downarrow}\dots) - (\hat{c}_{a'\downarrow}\dots\hat{c}_{j'\uparrow}\dots\hat{c}_{i'\downarrow}\dots)\right. \\
&\qquad\qquad \left. -(\hat{c}_{a'\downarrow}\dots\hat{c}_{j'\downarrow}\dots\hat{c}_{i'\uparrow}\dots)\right]\left(\sum_{\mu,\sigma}\hat{c}_{\mu\sigma}\phi_{\mu}(\mathbf{r})\chi_{\sigma}\right) \\
&\qquad\qquad \left[\left(\dots\hat{c}^{\dagger}_{i\uparrow}\dots\hat{c}^{\dagger}_{a\downarrow}\right)|0\rangle - \left(\dots\hat{c}^{\dagger}_{i\downarrow}\dots\hat{c}^{\dagger}_{a\uparrow}\right)|0\rangle\right] \\
&\qquad = \frac{1}{\sqrt{12}}\delta_{a,a'}\delta_{i,j'}\phi_{i'}(\mathbf{r})\chi_{\uparrow} \langle 0| \left[2(\hat{c}_{a\uparrow}\dots\hat{c}_{i\downarrow}\dots\hat{c}_{i'\downarrow}\dots)\hat{c}_{i'\uparrow}\left(\dots\hat{c}^{\dagger}_{i\downarrow}\dots\hat{c}^{\dagger}_{a\uparrow}\right)\right. \\
&\qquad\qquad \left. + (\hat{c}_{a\downarrow}\dots\hat{c}_{i\uparrow}\dots\hat{c}_{i'\downarrow}\dots)\hat{c}_{i'\uparrow}\left(\dots\hat{c}^{\dagger}_{i\uparrow}\dots\hat{c}^{\dagger}_{a\downarrow}\right)\right]|0\rangle \\
&\qquad + \frac{1}{\sqrt{12}}\delta_{a,a'}\delta_{i,i'}\phi_{j'}(\mathbf{r})\chi_{\uparrow} \langle 0| \left[2(\hat{c}_{a\uparrow}\dots\hat{c}_{j'\downarrow}\dots\hat{c}_{i\downarrow}\dots)\hat{c}_{j'\uparrow}\left(\dots\hat{c}^{\dagger}_{i\downarrow}\dots\hat{c}^{\dagger}_{a\uparrow}\right)\right. \\
&\qquad\qquad \left. + (\hat{c}_{a\downarrow}\dots\hat{c}_{j'\downarrow}\dots\hat{c}_{i\uparrow}\dots)\hat{c}_{j'\uparrow}\left(\dots\hat{c}^{\dagger}_{i\uparrow}\dots\hat{c}^{\dagger}_{a\downarrow}\right)\right]|0\rangle \\
&\qquad = +\frac{\sqrt{3}}{2}\delta_{a,a'}\delta_{i,j'}\phi_{i'}(\mathbf{r})\chi_{\uparrow} - \frac{\sqrt{3}}{2}\delta_{a,a'}\delta_{i,i'}\phi_{j'}(\mathbf{r})\chi_{\uparrow}.
\end{aligned}
\tag{3.61}
$$

The Dyson orbital involving the configuration in Eq. (3.49) of the final state is

$$\begin{aligned}\left\langle \Phi^{a'\uparrow}_{i'\uparrow,j'\downarrow}\right|_{csf} \hat{\psi}(\mathbf{r}) \left|\Phi^{a}_{i}\right\rangle_{csf} = \frac{1}{2} \langle 0| \left[(\hat{c}_{a'\uparrow} \dots \hat{c}_{j'\downarrow} \dots \hat{c}_{i'\uparrow} \dots) - (\hat{c}_{a'\uparrow} \dots \hat{c}_{j'\uparrow} \dots \hat{c}_{i'\downarrow} \dots)\right] \\ \left(\sum_{\mu,\sigma} \hat{c}_{\mu\sigma}\phi_{\mu}(\mathbf{r})\chi_{\sigma}\right) \left[\left(\dots \hat{c}^{\dagger}_{i\uparrow} \dots \hat{c}^{\dagger}_{a\downarrow}\right) - \left(\dots \hat{c}^{\dagger}_{i\downarrow} \dots \hat{c}^{\dagger}_{a\uparrow}\right)\right] |0\rangle\end{aligned} \tag{3.62}$$

Similar to the derivation of the previous Dyson orbital, we only get a non-zero contribution if $a = a'$

$$\begin{aligned}&\left\langle \Phi^{a'\uparrow}_{i'\uparrow,j'\downarrow}\right|_{csf} \hat{\psi}(\mathbf{r}) \left|\Phi^{a}_{i}\right\rangle_{csf} = \\ &\quad = -\frac{1}{2}\delta_{a,a'} \langle 0| \left[(\hat{c}_{a\uparrow} \dots \hat{c}_{j'\downarrow} \dots \hat{c}_{i'\uparrow} \dots) - (\hat{c}_{a'\uparrow} \dots \hat{c}_{j'\uparrow} \dots \hat{c}_{i'\downarrow} \dots)\right] \\ &\quad \left(\sum_{\mu,\sigma} \hat{c}_{\mu\sigma}\phi_{\mu}(\mathbf{r})\chi_{\sigma}\right) \left(\dots \hat{c}^{\dagger}_{i\downarrow} \dots \hat{c}^{\dagger}_{a\uparrow}\right) |0\rangle \\ &\quad = -\frac{1}{2}\delta_{a,a'}\delta_{i,j'}\phi_{i'}(\mathbf{r})\chi_{\downarrow} \langle 0| (\hat{c}_{a\uparrow} \dots \hat{c}_{i\downarrow} \dots \hat{c}_{i'\uparrow} \dots)\hat{c}_{i'\downarrow} \left(\dots \hat{c}^{\dagger}_{i\downarrow} \dots \hat{c}^{\dagger}_{a\uparrow}\right) |0\rangle \\ &\qquad + \frac{1}{2}\delta_{a,a'}\delta_{i,i'}\phi_{j'}(\mathbf{r})\chi_{\downarrow} \langle 0| (\hat{c}_{a\uparrow} \dots \hat{c}_{j'\uparrow} \dots \hat{c}_{i\downarrow} \dots)\hat{c}_{j'\downarrow} \left(\dots \hat{c}^{\dagger}_{i\downarrow} \dots \hat{c}^{\dagger}_{a\uparrow}\right) |0\rangle \\ &\quad = \frac{1}{2}\delta_{a,a'}\delta_{i,j'}\phi_{i'}(\mathbf{r})\chi_{\downarrow} + \frac{1}{2}\delta_{a,a'}\delta_{i,i'}\phi_{j'}(\mathbf{r})\chi_{\downarrow}.\end{aligned} \tag{3.63}$$

For the spin-down configuration in Eq. (3.50) of the final state, we obtain the Dyson orbital

$$\begin{aligned}&\left\langle \Phi^{a'\downarrow}_{i'\uparrow,j'\downarrow}\right|_{csf} \hat{\psi}(\mathbf{r}) \left|\Phi^{a}_{i}\right\rangle_{csf} = \\ &\quad = \frac{1}{2} \langle 0| \left[(\hat{c}_{a'\downarrow} \dots \hat{c}_{j'\downarrow} \dots \hat{c}_{i'\uparrow} \dots) - (\hat{c}_{a'\downarrow} \dots \hat{c}_{j'\uparrow} \dots \hat{c}_{i'\downarrow} \dots)\right] \\ &\quad \left(\sum_{\mu,\sigma} \hat{c}_{\mu\sigma}\phi_{\mu}(\mathbf{r})\chi_{\sigma}\right) \left[\left(\dots \hat{c}^{\dagger}_{i\uparrow} \dots \hat{c}^{\dagger}_{a\downarrow}\right) - \left(\dots \hat{c}^{\dagger}_{i\downarrow} \dots \hat{c}^{\dagger}_{a\uparrow}\right)\right] |0\rangle \\ &\quad = \frac{1}{2}\delta_{a,a'}\delta_{i,i'}\phi_{j'}(\mathbf{r})\chi_{\uparrow} \langle 0| (\hat{c}_{a\downarrow} \dots \hat{c}_{j'\downarrow} \dots \hat{c}_{i\uparrow} \dots)\hat{c}_{j'\uparrow} \left(\dots \hat{c}^{\dagger}_{i\uparrow} \dots \hat{c}^{\dagger}_{a\downarrow}\right) |0\rangle \\ &\qquad - \frac{1}{2}\delta_{a,a'}\delta_{i,j'}\phi_{i'}(\mathbf{r})\chi_{\uparrow} \langle 0| (\hat{c}_{a\downarrow} \dots \hat{c}_{i\uparrow} \dots \hat{c}_{i'\downarrow} \dots)\hat{c}_{i'\uparrow} \left(\dots \hat{c}^{\dagger}_{i\uparrow} \dots \hat{c}^{\dagger}_{a\downarrow}\right) |0\rangle \\ &\quad = -\frac{1}{2}\delta_{a,a'}\delta_{i,i'}\phi_{j'}(\mathbf{r})\chi_{\uparrow} - \frac{1}{2}\delta_{a,a'}\delta_{i,j'}\phi_{i'}(\mathbf{r})\chi_{\uparrow}.\end{aligned} \tag{3.64}$$

To summarize the results, the Dyson orbital, which involves an excited initial eigenstate

of the system in Eq. (3.39) and an excited ionized final state in Eq. (3.42) is

$$\langle \Phi_{F\sigma}| \hat{\psi}(\mathbf{r}) |\Phi_I\rangle = \sum_{i'} \sum_{i,a} (c_{i'}(F))^* c_i^a(I) \langle \Phi_{i'\sigma}|_{csf} \hat{\psi}(\mathbf{r}) |\Phi_i^a\rangle_{csf} \tag{3.65}$$

$$+ \sum_{i',a'} \sum_{i,a} (c_{i'}^{a'}(F))^* c_i^a(I) \left\langle \Phi_{i'i'}^{a'\sigma} \right|_{csf} \hat{\psi}(\mathbf{r}) |\Phi_i^a\rangle_{csf} \tag{3.66}$$

$$+ \sum_{i',j',a'} \sum_{i,a} (c_{i'j'}^{a'}(F)))^* c_i^a(I) \left\langle \Phi_{i'\sigma,j'\sigma}^{a'\bar{\sigma}} \right|_{csf} \hat{\psi}(\mathbf{r}) |\Phi_i^a\rangle_{csf} \tag{3.67}$$

$$+ \sum_{i',j',a'} \sum_{i,a} (c_{i'j'}^{a'}(F)))^* c_i^a(I) \left\langle \Phi_{i'\uparrow,j'\downarrow}^{a'\sigma} \right|_{csf} \hat{\psi}(\mathbf{r}) |\Phi_i^a\rangle_{csf} , \tag{3.68}$$

where $\sigma$ is the spin projection value of the final state $\uparrow$ or $\downarrow$, and $\bar{\sigma}$ is the opposite spin. To distinguish the two different cases for the value of $\sigma$, we introduce the function $\mathrm{sgn}(\sigma)$, which is $\mathrm{sgn}(\uparrow) = 1$ and $\mathrm{sgn}(\downarrow) = -1$. The matrix elements are

$$\langle \Phi_{i'\sigma}|_{csf} \hat{\psi}(\mathbf{r}) |\Phi_i^a\rangle_{csf} = -\frac{\mathrm{sgn}(\sigma)}{\sqrt{2}} \delta_{i,i'} \phi_a(\mathbf{r}) \chi_{\bar{\sigma}}, \tag{3.69}$$

$$\left\langle \Phi_{i'i'}^{a'\sigma} \right|_{csf} \hat{\psi}(\mathbf{r}) |\Phi_i^a\rangle_{csf} = -\frac{\mathrm{sgn}(\sigma)}{\sqrt{2}} \delta_{a,a'} \delta_{i,i'} \phi_i(\mathbf{r}) \chi_{\bar{\sigma}}, \tag{3.70}$$

$$\left\langle \Phi_{i'\sigma,j'\sigma}^{a'\bar{\sigma}} \right|_{csf} \hat{\psi}(\mathbf{r}) |\Phi_i^a\rangle_{csf} = \frac{\mathrm{sgn}(\sigma)\sqrt{3}}{2} \delta_{a,a'} \left[ -\delta_{i,j'} \phi_{i'}(\mathbf{r}) + \delta_{i,i'} \phi_{j'}(\mathbf{r}) \right] \chi_{\bar{\sigma}}, \tag{3.71}$$

$$\left\langle \Phi_{i'\uparrow,j'\downarrow}^{a'\sigma} \right|_{csf} \hat{\psi}(\mathbf{r}) |\Phi_i^a\rangle_{csf} = \frac{\mathrm{sgn}(\sigma)}{2} \delta_{a,a'} \left[ \delta_{i,j'} \phi_{i'}(\mathbf{r}) + \delta_{i,i'} \phi_{j'}(\mathbf{r}) \right] \chi_{\bar{\sigma}}. \tag{3.72}$$

We obtain an overall sign change in all matrix elements when the value of $\sigma$ changes, which we also obtained for the Dyson orbitals obtained from removing electrons from the ground state in Eq. (3.34) and Eq. (3.35).

With Eqs. (3.65)-(3.72) and the photoelectron probability in Eq. (3.25) we can now calculate the total photoelectron momentum probability. Based on these equations, I wrote a program that numerically calculates the photoelectron momentum probability based on the initial and final states calculated with the software MOLCAS [116]. The Fourier transformation of the MO is achieved by inserting the LCAO described in Sec. 2.1.4 and performing the Fourier transformation on GTO wavefunctions.

## 3.3. Electron-hole density change induced by the pump excitation

In this section, we derive the equations for calculating the change in the electronic density, considering that the pump pulse excites the system into a coherent superposition of excited eigenstates. This pump-induced electron-hole density is given by the difference of the electron density before the excitation $\rho_0(\mathbf{r})$ and after the excitation with the pump pulse $\rho_{ex}(\mathbf{r}, t)$, similar to the definition used in [120, 121]

$$\Delta\rho(\mathbf{r}, t) = \rho_{ex}(\mathbf{r}, t) - \rho_0(\mathbf{r}), \tag{3.73}$$

where $\rho_0(\mathbf{r})$ is the density of the ground state, which is time-independent.

For the electron-hole density, we evaluate the electron density for a molecule in the state $|\Psi(t)\rangle$

$$\rho(\mathbf{r}, t) = \langle\Psi(t)|\, \hat{\psi}^\dagger(\mathbf{r})\hat{\psi}(\mathbf{r})\, |\Psi(t)\rangle\,. \tag{3.74}$$

Similar to the previous derivations, the wavefunction of the excited molecule is a coherent superposition of excited eigenstates $|\Phi_I\rangle$

$$|\Psi(t)\rangle = \sum_I C_I e^{-iE_I(t-t_0)}\, |\Phi_I\rangle\,, \tag{3.75}$$

where the coefficients $C_I$ depend on the characteristics of the pump pulse and the system. Using CI up to single excitations, the spin-singlet eigenstates of the molecule are expanded as

$$|\Phi_I\rangle = \sum_{i,a} c_i^a(I)\, |\Phi_i^a\rangle_{csf}\,, \tag{3.76}$$

where $i$ is the orbital index from which an electron has been excited to the orbital with index $a$ and $S(I)$ denotes the spin. In contrast to the ground state where all orbitals up to HOMO are doubly occupied, the orbital $i$ is now singly occupied.

The density of the excited state in Eq. (3.74) is

$$\begin{aligned}\rho_{ex}(\mathbf{r},t) =& \sum_{IK} C_I^* C_K e^{-i(E_K-E_I)(t-t_0)} \sum_{iai'a'} (c_i^a(I))^* c_{i'}^{a'}(K) \\ & \sum_{\mu\mu',\sigma\sigma'} \phi_\mu^*(\mathbf{r})\phi_{\mu'}(\mathbf{r})\chi_\sigma^\dagger\chi_{\sigma'} \left\langle \Phi_i^a \right|_{csf} \hat{c}_{\mu\sigma}^\dagger \hat{c}_{\mu'\sigma'} \left| \Phi_{i'}^{a'} \right\rangle_{csf} \\ =& \sum_{IK} C_I^* C_K e^{-i(E_K-E_I)(t-t_0)} \sum_{iai'a'} (c_i^a(I))^* c_{i'}^{a'}(K) \\ & \sum_{\mu\mu'} \phi_\mu^*(\mathbf{r})\phi_{\mu'}(\mathbf{r}) \sum_\sigma \left\langle \Phi_i^a \right|_{csf} \hat{c}_{\mu\sigma}^\dagger \hat{c}_{\mu'\sigma} \left| \Phi_{i'}^{a'} \right\rangle_{csf},\end{aligned} \tag{3.77}$$

where we used that the spin function is orthogonal $\sigma = \sigma'$. The CSF is a superposition of SDs

$$|\Phi_i^a\rangle_{csf} = \frac{1}{\sqrt{2}} \left( \left| \Phi_{i\uparrow}^{a\downarrow} \right\rangle_{SD} + \left| \Phi_{i\downarrow}^{a\uparrow} \right\rangle_{SD} \right). \tag{3.78}$$

For the matrix element between two spin-singlet states, we obtain

$$\begin{aligned}\sum_\sigma \left\langle \Phi_i^a \right|_{csf} \hat{c}_{\mu\sigma}^\dagger \hat{c}_{\mu'\sigma} \left| \Phi_{i'}^{a'} \right\rangle_{csf} =& \sum_\sigma \frac{1}{2} \left( \left\langle \Phi_{i\uparrow}^{a\downarrow} \right|_{SD} - \left\langle \Phi_{i\downarrow}^{a\uparrow} \right|_{SD} \right) \hat{c}_{\mu\sigma}^\dagger \hat{c}_{\mu'\sigma} \\ & \left( \left| \Phi_{i'\uparrow}^{a'\downarrow} \right\rangle_{SD} - \left| \Phi_{i'\downarrow}^{a'\uparrow} \right\rangle_{SD} \right) \\ =& \sum_\sigma \frac{1}{2} \left( \left\langle \Phi_{i\uparrow}^{a\downarrow} \right|_{SD} \hat{c}_{\mu\sigma}^\dagger \hat{c}_{\mu'\sigma} \left| \Phi_{i'\uparrow}^{a'\downarrow} \right\rangle_{SD} \right. \\ & \left. + \left\langle \Phi_{i\downarrow}^{a\uparrow} \right|_{SD} \hat{c}_{\mu\sigma}^\dagger \hat{c}_{\mu'\sigma} \left| \Phi_{i'\downarrow}^{a'\uparrow} \right\rangle_{SD} \right).\end{aligned} \tag{3.79}$$

Similar to evaluating the photoelectron probability in Sec. 3.2, we rewrite the SD with creation and annihilation operators. We consider four different cases for the indices $i, i', a, a'$

$$\sum_\sigma \left\langle \Phi_i^a \right|_{csf} \hat{c}_{\mu\sigma}^\dagger \hat{c}_{\mu'\sigma} \left| \Phi_{i'}^{a'} \right\rangle_{csf} = \sum_\sigma \langle \Phi_i^a |_{csf} \hat{c}_{\mu\sigma}^\dagger \hat{c}_{\mu'\sigma} |\Phi_i^a\rangle_{csf} \delta_{i,i'}\delta_{a,a'} \tag{3.80}$$

$$+ \sum_\sigma \langle \Phi_i^a |_{csf} \hat{c}_{\mu\sigma}^\dagger \hat{c}_{\mu'\sigma} |\Phi_{i'}^a\rangle_{csf} (1-\delta_{i,i'})\delta_{a,a'} \tag{3.81}$$

$$+ \sum_\sigma \langle \Phi_i^a |_{csf} \hat{c}_{\mu\sigma}^\dagger \hat{c}_{\mu'\sigma} \left| \Phi_i^{a'} \right\rangle_{csf} \delta_{i,i'}(1-\delta_{a,a'}) \tag{3.82}$$

$$+ \sum_\sigma \langle \Phi_i^a |_{csf} \hat{c}_{\mu\sigma}^\dagger \hat{c}_{\mu'\sigma} \left| \Phi_{i'}^{a'} \right\rangle_{csf} (1-\delta_{i,i'})(1-\delta_{a,a'}) \tag{3.83}$$

where $(1-\delta_{i,i'})$ is non-zero only if $i \neq i'$. In the first case, we evaluate the matrix element

between the same configurations in Eq. (3.80), meaning $i = i'$ and $a = a'$

$$\sum_\sigma \langle \Phi_i^a|_{csf}\, \hat{c}^\dagger_{\mu\sigma}\hat{c}_{\mu'\sigma}\, |\Phi_i^a\rangle_{csf} = \sum_\sigma \frac{1}{2}\Big(\Big\langle \Phi_{i\uparrow}^{a\downarrow}\Big|_{SD}\, \hat{c}^\dagger_{\mu\sigma}\hat{c}_{\mu'\sigma}\, \Big|\Phi_{i\uparrow}^{a\downarrow}\Big\rangle_{SD} + \Big\langle \Phi_{i\downarrow}^{a\uparrow}\Big|_{SD}\, \hat{c}^\dagger_{\mu\sigma}\hat{c}_{\mu'\sigma}\, \Big|\Phi_{i\downarrow}^{a\uparrow}\Big\rangle_{SD}\Big) \tag{3.84}$$

$$= \sum_\sigma \frac{1}{2}\Big[\langle 0|\dots \hat{c}_{i\uparrow}\dots \hat{c}_{a\downarrow}\left(\hat{c}^\dagger_{\mu\sigma}\hat{c}_{\mu'\sigma}\right)\hat{c}^\dagger_{a\downarrow}\dots\hat{c}^\dagger_{i\uparrow}\dots|0\rangle + \langle 0|\dots \hat{c}_{i\downarrow}\dots \hat{c}_{a\uparrow}\left(\hat{c}^\dagger_{\mu\sigma}\hat{c}_{\mu'\sigma}\right)\hat{c}^\dagger_{a\uparrow}\dots\hat{c}^\dagger_{i\downarrow}\dots|0\rangle\Big] \tag{3.85}$$

$$= \delta_{\mu,a}\delta_{\mu',a} + \delta_{\mu,i}\delta_{\mu',i} + 2\delta_{\mu,\mu'}(1-\delta_{\mu,(i,a)}), \tag{3.86}$$

where the function $(1-\delta_{\mu,(i,a)})$ is non-zero if the index $\mu$ is equal to the index of the doubly occupied orbitals in the configuration $|\Phi_i^a\rangle_{csf}$. We see that doubly occupied orbitals contribute with a factor of two, representing their occupation.

For the second matrix element in Eq. (3.81), the singly occupied electron in the orbitals energetically above the HOMO is equal $a = a'$. The matrix element is

$$\sum_\sigma \langle \Phi_i^a|_{csf}\, \hat{c}^\dagger_{\mu\sigma}\hat{c}_{\mu'\sigma}\, |\Phi_{i'}^a\rangle_{csf} \underset{i\neq i'}{=} \sum_\sigma \frac{1}{2}\Big[\langle 0|\dots \hat{c}_{i\uparrow}\dots \hat{c}_{a\downarrow}\left(\hat{c}^\dagger_{\mu\sigma}\hat{c}_{\mu'\sigma}\right)\hat{c}^\dagger_{a\downarrow}\dots\hat{c}^\dagger_{i'\uparrow}\dots|0\rangle + \langle 0|\dots \hat{c}_{i\downarrow}\dots \hat{c}_{a\uparrow}\left(\hat{c}^\dagger_{\mu\sigma}\hat{c}_{\mu'\sigma}\right)\hat{c}^\dagger_{a\uparrow}\dots\hat{c}^\dagger_{i'\downarrow}\dots|0\rangle\Big] \tag{3.87}$$

$$= \frac{1}{2}\delta_{\mu,i'}\delta_{\mu',i}\Big[\langle 0|\dots \hat{c}_{i\uparrow}\dots \hat{c}_{a\downarrow}\left(\hat{c}^\dagger_{i'\downarrow}\hat{c}_{i\downarrow}\right)\hat{c}^\dagger_{a\downarrow}\dots\hat{c}^\dagger_{i'\uparrow}\dots|0\rangle + \langle 0|\dots \hat{c}_{i\downarrow}\dots \hat{c}_{a\uparrow}\left(\hat{c}^\dagger_{i'\uparrow}\hat{c}_{i\uparrow}\right)\hat{c}^\dagger_{a\uparrow}\dots\hat{c}^\dagger_{i'\downarrow}\dots|0\rangle\Big] \tag{3.88}$$

$$= -\frac{1}{2}\delta_{\mu,i'}\delta_{\mu',i}\Big[\langle 0|\dots \hat{c}_{i\downarrow}\hat{c}_{i\uparrow}\dots \hat{c}_{a\downarrow}\hat{c}^\dagger_{a\downarrow}\dots\hat{c}^\dagger_{i'\uparrow}\hat{c}^\dagger_{i'\downarrow}\dots|0\rangle + \langle 0|\dots \hat{c}_{i\downarrow}\hat{c}_{i\uparrow}\dots \hat{c}_{a\uparrow}\hat{c}^\dagger_{a\uparrow}\dots\hat{c}^\dagger_{i'\uparrow}\hat{c}^\dagger_{i'\downarrow}\dots|0\rangle\Big] \tag{3.89}$$

$$= -\delta_{\mu,i'}\delta_{\mu',i}, \tag{3.90}$$

where minus arises due to the reordering of the operators.

In the matrix element in Eq. (3.82) the configurations have the same singly occupied orbital

energetically below the LUMO $i = i'$. The matrix element is

$$\begin{aligned}\sum_\sigma \langle \Phi_i^a|_{csf}\, \hat{c}^\dagger_{\mu\sigma}\hat{c}_{\mu'\sigma} \left|\Phi_i^{a'}\right\rangle_{csf} &\underset{a\neq a'}{=} \sum_\sigma \frac{1}{2}\Big[\langle 0|\dots \hat{c}_{i\uparrow}\dots \hat{c}_{a\downarrow}\left(\hat{c}^\dagger_{\mu\sigma}\hat{c}_{\mu'\sigma}\right)\hat{c}^\dagger_{a'\downarrow}\dots\hat{c}^\dagger_{i\uparrow}\dots|0\rangle \\ &\qquad + \langle 0|\dots \hat{c}_{i\downarrow}\dots \hat{c}_{a\uparrow}\left(\hat{c}^\dagger_{\mu\sigma}\hat{c}_{\mu'\sigma}\right)\hat{c}^\dagger_{a'\uparrow}\dots\hat{c}^\dagger_{i\downarrow}\dots|0\rangle\Big] \qquad (3.91)\\ &= \frac{1}{2}\delta_{\mu,a}\delta_{\mu',a'}\Big[\langle 0|\dots \hat{c}_{i\uparrow}\dots \hat{c}_{a\downarrow}\left(\hat{c}^\dagger_{a\downarrow}\hat{c}_{a'\downarrow}\right)\hat{c}^\dagger_{a'\downarrow}\dots\hat{c}^\dagger_{i\uparrow}\dots|0\rangle \\ &\qquad + \langle 0|\dots \hat{c}_{i\downarrow}\dots \hat{c}_{a\uparrow}\left(\hat{c}^\dagger_{a\uparrow}\hat{c}_{a'\uparrow}\right)\hat{c}^\dagger_{a'\uparrow}\dots\hat{c}^\dagger_{i\downarrow}\dots|0\rangle\Big] \qquad (3.92)\\ &= \delta_{\mu,a}\delta_{\mu',a'}. \qquad (3.93)\end{aligned}$$

The operators $\hat{c}^\dagger_{\mu\sigma}\hat{c}_{\mu'\sigma}$ in the matrix elements can only change the occupation of one electron from an orbital $\mu'$ to another orbital $\mu$. The two configurations in the matrix element in Eq. (3.83) differ by more than one orbital occupation. Therefore we obtain

$$\sum_\sigma \langle \Phi_i^a|_{csf}\, \hat{c}^\dagger_{\mu\sigma}\hat{c}_{\mu'\sigma} \left|\Phi_{i'}^{a'}\right\rangle_{csf} (1-\delta_{i,i'})(1-\delta_{a,a'}) = 0. \qquad (3.94)$$

Combining these results, the whole matrix element is

$$\begin{aligned}\sum_\sigma \langle \Phi_i^a|_{csf}\, \hat{c}^\dagger_{\mu\sigma}\hat{c}_{\mu'\sigma} \left|\Phi_{i'}^{a'}\right\rangle_{csf} &= \left(\delta_{\mu,a}\delta_{\mu',a} + \delta_{\mu,i}\delta_{\mu',i} + 2\delta_{\mu,\mu'}(1-\delta_{\mu,(i,a)})\right)\delta_{i,i'}\delta_{a,a'} \\ &\quad - \delta_{\mu,i'}\delta_{\mu',i}(1-\delta_{i,i'})\delta_{a,a'} + \delta_{\mu,a}\delta_{\mu',a'}\delta_{i,i'}(1-\delta_{a,a'}) \qquad (3.95)\\ &= 2\delta_{\mu,\mu'}(1-\delta_{\mu,a})\delta_{i,i'}\delta_{a,a'} - \delta_{\mu,i'}\delta_{\mu',i}\delta_{a,a'} + \delta_{\mu,a}\delta_{\mu',a'}\delta_{i,i'}.\end{aligned}$$

With the orbital wavefunctions $\phi^*_\mu(\mathbf{r})$ and $\phi_{\mu'}(\mathbf{r})$ and sum over $\mu$ and $\mu'$ we obtain

$$\begin{aligned}\sum_{\mu\mu'}\sum_\sigma \langle \Phi_i^a|_{csf}\, \hat{c}^\dagger_{\mu\sigma}\hat{c}_{\mu'\sigma} \left|\Phi_{i'}^{a'}\right\rangle_{csf} \phi^*_\mu(\mathbf{r})\phi_{\mu'}(\mathbf{r}) =& 2\delta_{i,i'}\delta_{a,a'}\sum_{\mu\neq a}|\phi_\mu(\mathbf{r})|^2 \\ &- \delta_{a,a'}\phi^*_{i'}(\mathbf{r})\phi_i(\mathbf{r}) \qquad (3.96)\\ &+ \delta_{i,i'}\phi^*_a(\mathbf{r})\phi_{a'}(\mathbf{r}),\end{aligned}$$

where we rewrote the sum $\sum_{\mu\neq a} = \sum_{\mu\leq \mathrm{HOMO}}$, meaning that we sum over all orbitals which are occupied in the HF ground state. Inserting Eq. (3.96) into Eq. (3.77), the electronic

density for the coherent superposition of excited eigenstates becomes

$$\begin{aligned}
\rho_{ex}(\mathbf{r},t) =& \sum_{IK} \underbrace{C_I^* C_K e^{-i(E_K-E_I)(t-t_0)}}_{=\mathcal{I}_{IK}(t)} \sum_{ia,i'a'} (c_i^a(I))^* c_{i'}^{a'}(K) \\
& \sum_{\mu\mu',\sigma\sigma'} \phi_\mu^*(\mathbf{r})\phi_{\mu'}(\mathbf{r})\chi_\sigma^\dagger\chi_{\sigma'} \left\langle \Phi_i^a \right|_{csf} \hat{c}_{\mu\sigma}^\dagger \hat{c}_{\mu'\sigma'} \left| \Phi_{i'}^{a'} \right\rangle_{csf} \\
=& \sum_{IK} \mathcal{I}_{IK}(t) \sum_{iai'a'} (c_i^a(I))^* c_{i'}^{a'}(K) \\
& \left[ 2\delta_{i,i'}\delta_{a,a'} \sum_{\mu\neq a} |\phi_\mu(\mathbf{r})|^2 - \delta_{a,a'}\phi_{i'}^*(\mathbf{r})\phi_i(\mathbf{r}) + \delta_{i,i'}\phi_a^*(\mathbf{r})\phi_{a'}(\mathbf{r}) \right] \\
=& 2 \sum_{\mu\leq HOMO} |\phi_\mu(\mathbf{r})|^2 + \sum_{IK} \mathcal{I}_{IK}(t) \sum_{iai'a'} (c_i^a(I))^* c_{i'}^{a'}(K) \\
& \left[ -\delta_{a,a'}\phi_{i'}^*(\mathbf{r})\phi_i(\mathbf{r}) + \delta_{i,i'}\phi_a^*(\mathbf{r})\phi_{a'}(\mathbf{r}) \right].
\end{aligned} \tag{3.97}$$

In the last step of Eq. (3.97), we used the normalization of the initial wavepacket

$$\langle \Psi(t)|\Psi(t)\rangle = \sum_{I,K} C_I^* C_K e^{-i(E_K-E_I)} \sum_{ia} \tilde{c}_i^a(I)^* \tilde{c}_i^a(K) = 1. \tag{3.98}$$

Eq. (3.97) is the complete expression for the electronic density. The interesting part is the pump pulse-induced change in the electronic density in Eq. (3.73). For the evaluation, we need to calculate the density in the HF ground state, which is the sum of the absolute square of all doubly occupied orbitals

$$\rho_{GS}(\mathbf{r},t) = 2 \sum_{\mu\leq \mathrm{HOMO}} |\phi_\mu(\mathbf{r})|^2 . \tag{3.99}$$

The summation over the doubly occupied orbital in Eq. (3.97) is equal to the density in the HF ground state. The electron-hole density created by the pump pulse excitation thus is

$$\Delta\rho(\mathbf{r},t) = \sum_{IK} \mathcal{I}_{IK}(t) \sum_{iai'a'} (c_i^a(I))^* c_{i'}^{a'}(K) \left[ -\delta_{a,a'}\phi_{i'}^*(\mathbf{r})\phi_i(\mathbf{r}) + \delta_{i,i'}\phi_a^*(\mathbf{r})\phi_{a'}(\mathbf{r}) \right]. \tag{3.100}$$

The positive part in the electron-hole density results from the orbitals of the excited electron ($a$ and $a'$) and the negative from the orbitals where the electrons have been excited from ($i$ and $i'$). The term in the electron-hole density is time-independent if $I = K$, while the contribution for $I \neq K$ is time-dependent.

Based on this derivation, we developed a program that calculates the electron-hole density.

The program takes the excited states calculated with CIS from MOLCAS and calculates the electron-hole density according to Eq. (3.100). The MOs in the calculation is replaced by the GTO based on the LCAO shown in Sec. 2.1.4.

# 4. Time-resolved momentum microscopy of a pentacene film

The results of the following chapter have been published in [62]. In this combined theoretical and experimental work, our experimental collaborators performed a tr-ARPES experiment at a FEL beamline. They investigated the properties of a bilayer pentacene film adsorbed on a silver substrate with surface orientation Ag(110). I performed theoretical calculations which interpreted and explained the obtained results under the supervision of Daria Gorelova. I mainly exchanged information with Kiana Baumgärtner, Christian Metzger, and Markus Scholz in this collaboration.

In the following, I start with an introduction and give an overview of molecular thin films adsorbed on a substrate in Sec. 4.1. Then I explain the experimental setup used in this study in Sec. 4.2. I continue in Sec. 4.3 with a description of the calculations performed on isolated pentacene and a model for a single pentacene on the substrate. The results and a discussion is presented in Sec. 4.4. I finish the chapter with a summary.

## 4.1. Introduction

Molecular thin films adsorbed on a substrate combine properties of both worlds, localized molecular states, and delocalized charge carrier states in the substrate. Organic ($\pi$-conjugated) molecules coupled to inorganic interfaces are important for developing organic electronic devices [122, 123].

The charge transfer at the interface between the molecular layer and the substrate defines the function of such devices. The properties of the molecular layer are linked to the energy levels of the MO and especially the HOMO and LUMO energies and the corresponding

energy gaps. The band structure describes the properties of the substrate, while the Fermi energy $E_F$ and the work function $\phi$ are important values. If these two materials are in contact, their wavefunctions can overlap at the interface which defines the bonding strength, and in addition, charge transfer can occur. The exact behavior depends on the properties of the molecules and the substrate. More details can be found in [124, 125, 126].

If the interaction between the molecules and the substrate is weak (physisorption), the geometry and the electronic structure of the adsorbed molecules are only slightly perturbed. Weak electrostatic forces like van der Waals forces mediate the bonding. For stronger interactions, chemical bonds can be formed between the molecule and the substrate (chemisorption). In this case, the geometry and electronic structure of the adsorbed molecules can vary significantly from the properties of the isolated molecule. The adsorption geometry of the molecules also determines important properties of the system [127].

The interaction of molecules with substrates and their geometry has been investigated theoretically with different models. For simulating such systems, periodic slab and cluster models have successfully been used to reproduce and understand the experimental results from molecules adsorbed on substrates [128, 129, 130, 131, 132, 133]. Periodic slab models explicitly treat the system's periodicity, including long-range interactions. In cluster models, the substrate is constructed from a finite number of atoms. Dangling bonds in the cluster approach can be compensated with hydrogen atoms or point charge arrays. More details and comparisons of the methods can be found in [124, 134]. For example, perylenetetracarboxylic dianhydride (PTCDA) adsorbed on different substrates has been studied in detail using slab and cluster models. Calculated adsorption energies of the molecules, charge transfer properties, and the adsorption geometry of PTCDA are in agreement with experimental data [130, 133, 135].

Our experimental collaborators investigated a sample consisting of a bilayer of pentacene adsorbed on Ag(110). Pentacene is a linear acene and consists of five benzene rings linearly merged. It also has been used in several functional devices, such as OLEDs [136], organic thin film transistors [137, 138] and others [139, 140]. Pentacene is a promising material for OSCs since it can overcome the Shockley–Queisser limit by the conversion of one singlet excited state into two triplet ones (singlet fission) [141, 142, 143]. In the experimental

sample pentacene adsorbed on the substrate in a nearly flat geometry. The pentacene molecules which are in direct contact with the substrate show chemisorption, leading to a charge transfer into the LUMO of pentacene [144]. In a bilayer structure, the molecules are slightly tilted on the surface, and the molecules farther from the substrate do not show charge transfer.

In this study, we want to investigate orbital tomography in the time-resolved domain involving an experiment performed at a FEL. Therefore the theoretical part of the following study is motivated by calculating properties of isolated pentacene in the ground and excited state and relating this to the experimentally obtained time-resolved results. With this, we explain time-resolved microscopic processes in the system up to hundreds of femtoseconds after excitation. Additionally, we perform calculations on a model, which includes a single molecule and a cluster of silver atoms, to describe the molecule-substrate interaction and explain the experimental data.

## 4.2. Experimental details

This section briefly summarizes the sample properties and the experimental setup. More details can be found in [62]. In the experiment, our collaborators studied a bilayer pentacene film adsorbed on Ag(110). The sample was prepared with organic molecular beam epitaxy (OMBE). In OMBE, the molecules are evaporated in a so-called Knudsen cell and are deposited onto the substrate. The OMBE takes place in ultra-high vacuum (pressure $10^{-9}$ mbar).

The pentacene molecules in the two layers are well-ordered and lie almost flat on the surface. The sample structure is the same as in [144]. The molecules in the layer closer to the substrate (first layer) are tilted 6° and in the second layer 8.5° along the long axis of the molecule. The long axis of the molecule is parallel to the [001] direction of the substrate (illustrated in Fig. 4.1). The size of the unit cell of the molecules in the second layer is $\approx 72\%$ larger than that of the first layer.

The experiment was performed at the FEL FLASH in Hamburg (PG2 beamline) [145]. The pump pulse has an energy of 3.1 eV and a probe pulse 35 eV. The incident pump and probe pulses hit the sample from a polar angle $\theta = 68°$ and an azimuthal angle $\varphi = 64°$, as

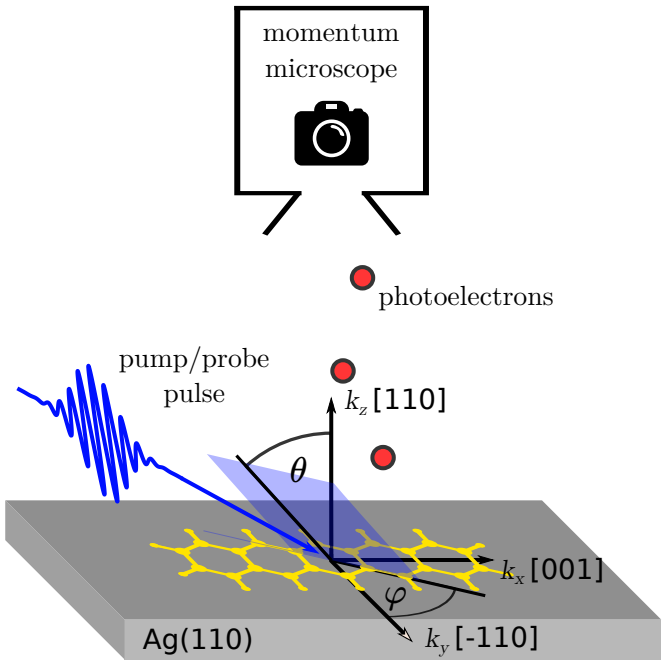


Figure 4.1.: Schematic illustration of the geometry in the experimental setup. The pentacene molecules in the first and second layers (here, represented with one example molecule in yellow) are aligned parallel to the [001] direction of the substrate (shown in grey). The pump and probe beam hit the sample from a direction defined by the polar angle $\theta = 68°$ and azimuthal angle $\varphi = 64°$. The photoelectrons emitted from the interaction with the probe pulse (red circles) are measured with the momentum microscope. Adapted from Ref. [62].

shown in Fig. 4.1. The pulses are $p$-polarized. The photoelectrons, which are emitted to the hemisphere above the sample, are detected with a time-of-flight momentum microscope.

## 4.3. Computational details

In the calculations, we theoretically investigate the properties of isolated pentacene as well as a model for pentacene on the substrate. The ground and excited state properties are simulated with an isolated pentacene molecule. The effect of the substrate interaction is modeled by a single pentacene placed on top of a cluster of silver atoms. We perform the electronic and atomic structure calculations using the RASSCF module implemented in the *ab initio* software MOLCAS [116]. By turning off the orbital optimization in the RASSCF module, we effectively perform a RASCI calculation.

### 4.3.1. Photoelectron spectra

We compute the photoelectron momentum distribution based on the description in Sec. 3.1 and Sec. 3.2. The probe pulse duration involved in this experiment is long enough to calculate the photoelectron momentum distribution according to Eq. (3.29)

$$P(\mathbf{q}, t_p) \propto |\boldsymbol{\epsilon}_{in} \cdot \mathbf{q}|^2 \sum_{\sigma,F} \delta_{\epsilon_e, E_j^{N_e} - E_F^{N_e-1} + \omega_{in}} \left| \chi_\sigma^\dagger \int d^3r \; e^{-i\mathbf{qr}} \phi_F^D(\mathbf{r}) \right|^2 , \tag{4.1}$$

where $\boldsymbol{\epsilon}_{in}$ describes the polarization of the probe pulse and $\omega_{in}$ the energy of the probe pulse. The terms $E_F^{N_e-1}$ describe the energies of the final state $\left|\Phi_F^{N_e-1}\right\rangle$, $E_j^{N_e}$ the energy of the initial state $\left|\Phi_j^{N_e}\right\rangle$ and $\epsilon_e$ the energy of the outgoing photoelectron with wave-vector $\mathbf{q}$ which is treated in the PWA. The spin wavefunction of the photoelectron is $\chi_\sigma^\dagger$. The evaluation of the Dyson orbital $\phi_F^D(\mathbf{r})$ within the method of CI is shown in detail in Sec. 3.2.

### 4.3.2. Photoelectron momentum distribution from isolated pentacene

The ground state of the neutral isolated pentacene is obtained from a HF calculation. For the AO of the H and C atoms, we use a cc-pVDZ basis set [146, 147]. We describe the electronically excited states of neutral pentacene based on the CI method truncated to single excitations. The calculation is converged with a restricted active space with eleven

occupied $\pi$-orbitals in the RAS1 space and eleven unoccupied $\pi^*$-orbitals in the RAS3 space. The RAS1 space contains a maximum of one hole and the RAS3 space a maximum of one electron. The RAS2 space is empty.

The excited and the ground state of neutral pentacene describe the initial states of the system before it is photoionized with the probe pulse. The final states after the ionization of the system with the probe pulse are obtained from a RASCI calculation with an additional hole in the RAS1 space. According to Koopmans' theorem, the Dyson orbitals from the ground state are equal to a single MO, while their orbital energy is the electron's binding energy. In the case of the excited state, the Dyson orbitals are sums over MO, as shown in Sec. 3.2.

In the calculation of the ground state, the geometry of the atoms is optimized with MOLCAS. For the calculation of the excited states of neutral pentacene, we consider two different scenarios. First, on timescales faster than the geometric changes of the atoms, the pump pulse excitation leads to an excitation of the electronic structure without geometry rearrangements of the atoms. We call this the vertical excited state. Second, at later times after the pump pulse excitation, the atoms rearrange to the changed electronic structure, and their geometry changes. We call this the geometry-relaxed excited state.

### 4.3.3. Modelling pentacene on the substrate

We explain the substrate and molecule interaction using our program initially planned for calculations on isolated molecules. Therefore we model the system with MOLCAS with a straightforward cluster approach. It has been shown that electronic correlation effects in such systems are important and can be included with higher excitation determinants in CI or by using perturbation theory [130, 148]. Due to computational limitations, we are restricted to calculations based on HF. In this approach, we are only interested in the changes induced in the molecules and not in specific substrate properties. We will verify this approach by comparison to the experimental data.

To model the interaction of the substrate with the pentacene molecule, we take a single pentacene in the isolated ground state geometry, which is assumed to be flat on top of the silver substrate. We use this simplified approach because, due to computational challenges, we could not compute this structure's equilibrium geometry. The substrate below the

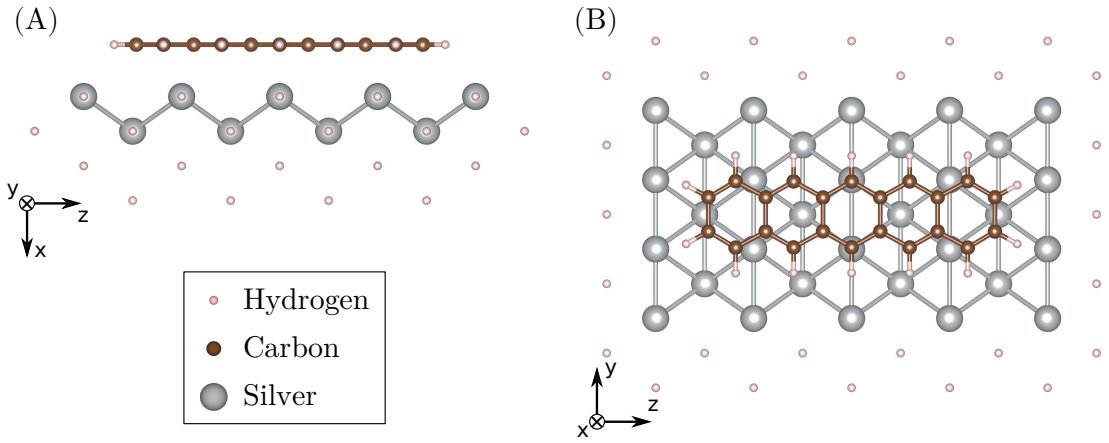


Figure 4.2.: Geometry of the structure used for modeling a single pentacene on the Ag(110) cluster. (A) shows the structure from the side view and (B) from the top view. For visualization of the structure, we used the software VESTA [150]. Adapted from Ref. [62].

pentacene is simulated with a cluster of silver atoms. The geometry of the silver atoms is based on the bulk crystal structure involving a neighboring distance of $d = 2.942$ Å [149].

The cluster includes 20 atoms in the first and 12 in the second layer. Due to the finite size of the substrate cluster, the atoms at the border have fewer bonds than in the real crystal. We compensate for these missing bonds by placing hydrogen atoms at the border so that each silver has the same number of nearest neighbors as the complete structure. The complete structure is shown in Fig. 4.2. In the y and z direction, the cluster represents the unit cell size in the sample [144]. To check the convergence of the model, we increased the number of atoms in the substrate in the x,y, and z directions. We verified that the shape and relative energies of the orbitals, which are mainly localized in the pentacene molecule, do not change significantly.

From the experimental data, the adsorption site and adsorption height of the pentacene molecules on the substrate are unknown. We choose the relative position of the pentacene to the silver atoms based on theoretical work in [151]. We perform the calculations for different distances between the pentacene and the substrate.

The ground state of the system is obtained with a HF calculation. We use a cc-pVDZ basis set for the H and C atoms [146, 147] and a cc-pVDZ basis including a pseudopotential for

the silver atoms [147, 152, 153]. The pseudopotential describes the 28 core electrons in silver, and the remaining 19 electrons are treated explicitly.

We use Koopmans' theorem to describe the final states after the ionization. The Dyson orbital for evaluating the photoelectron probability equals the MO from which the photoelectron has been removed. The negative value of the corresponding orbital energy gives the corresponding binding energy.

## 4.4. Results and Discussion

The experiment was performed in 2018 and initially planned to prove whether molecular thin films could withstand the high intensities of FEL sources. The measured energy distribution curves (EDCs) for the pumped and unpumped samples are shown in Fig. 4.3. Each of the four curves is time integrated for 15 minutes of the measurement. The pronounced peaks in the EDCs at different binding energies can be assigned to MOs, which is in agreement with [144]. This assignment is done by comparing the measured PMMs, which are two-dimensional momentum distributions of the photoelectrons at constant kinetic/binding energies, to the calculated PMMs stemming from orbitals of isolated pentacene (Fig. 4.4). The peaks in the EDCs stemming from MO features are approximately 500 meV wide in energy. We also see that the LUMO of the pentacene molecules in the first layer is occupied in the system [144]. The EDCs at different times for the pumped and unpumped data look similar. Therefore, the sample damage during the measurement can be considered small during the time of measurement. A more detailed discussion is in [62].

### 4.4.1. Time integrated analysis

The experimental PMMs are constructed from the photoelectron distribution at constant binding energies and are integrated 500 meV around the center of the peaks in the EDCs (Fig. 4.3). The PMMs at the binding energies corresponding to the features from the $\mathrm{LUMO}_{1^{st}}$, $\mathrm{HOMO}_{1^{st}}$, $\mathrm{HOMO}_{2^{nd}}$ and $\mathrm{HOMO\text{-}1}_{1^{st}}$ are shown in Fig. 4.4(A)-(D). The data is integrated over all measured time delays between the pump and the probe pulse.

The calculated PMMs are shown in Fig. 4.4(F)-(I). The PMM in Fig. 4.4(F) results from the first vertical excited state of neutral isolated pentacene, while the Dyson orbital is

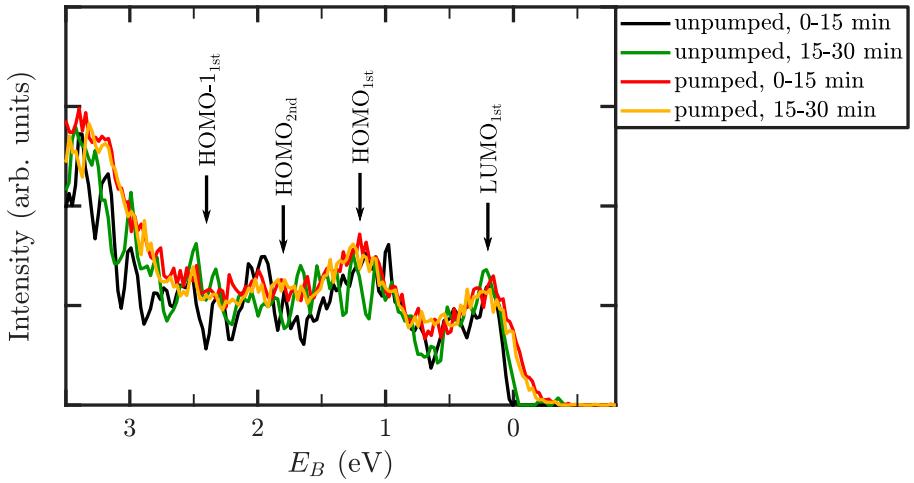


Figure 4.3.: Experimentally measured EDCs, where the intensity of the photoelectron probability is plotted depending on the binding energy $E_B$. The black/green curves show the unpumped data measured from minutes 0-15 and 15-30, while the red/orange data shows the pumped sample in the same duration. The peaks in the curves are assigned to different orbitals of the first and second pentacene layer, labeled by $1^{st}$ and $2^{nd}$. The corresponding $E_B$ is marked with black arrows. For comparison, the curves are normalized at the binding energy of $E_B = 2.15$ eV. Adapted from Ref. [62].

approximately equal to the LUMO. The PMMs in Fig. 4.4(G), (H), and (I) are obtained from the ground state of an isolated pentacene, where the Dyson orbital is equal to MOs. In Fig. 4.4(F),(G) and (I), the PMM is obtained from a molecule that is tilted by 6.0° along the long axis corresponding to the geometry of the pentacene in the first layer. The PMM in Fig. 4.4(H) is calculated from an isolated pentacene tilted by 8.5° along the long axis.

The experimental PMMs labeled by $\mathrm{LUMO}_{1^{st}}$, $\mathrm{HOMO}_{1^{st}}$, $\mathrm{HOMO}_{2^{nd}}$, and the $\mathrm{HOMO\text{-}1}_{1^{st}}$ can be clearly distinguished from one another and can be assigned to the corresponding MO of pentacene by comparison to the simulations. In Fig. 4.4(D), the position of the black peak in the lower left indicates a contribution from HOMO-1 of the first pentacene layer (Fig. 4.4(I)). However, in the calculations, the binding energy of electrons in the HOMO-1 is close to the one for the HOMO-2 and would overlap in the integration range of 500 meV (Fig. 4.4(J)). The experimental data show no contribution from the HOMO-2 orbital of isolated pentacene but it is expected at higher binding energies. It is also unclear if this gap might increase due to the interaction with the substrate and is therefore not visible. Due to overlap with photoelectrons emitted from the substrate, photoelectron distributions for higher binding energies could not be assigned to MO of isolated pentacene.

All PMMs with contribution from MOs show a maximum intensity around $k_x \approx 1.1$ Å$^{-1}$. The $D_{2h}$ symmetry group of the pentacene molecule is not recovered in the PMMs because the polarization of the probe pulse and the tilt of the molecules results in a symmetry breaking in the PMMs. This causes an increased photoelectron probability in the lower left corner.

The calculated and experimentally measured spectra in Fig. 4.4 agree. A previous static study on this system already evaluated this system in detail, revealing structural properties of the molecules [144]. However, we see that mapping the experimentally obtained PMMs to orbital features of the isolated molecule is still possible and that the system is not damaged by the higher light intensities at the FEL.

The calculation on isolated pentacene cannot resolve the features appearing at the Γ-point of the experimental PMMs and cannot explain the charge transfer into the LUMO. The experimental PMM from the clean Ag(110) substrate at the binding energy of $\mathrm{HOMO}_{1^{st}}$ is shown in Fig. 4.4(E). It indicates that the intensity at the Γ-point results from the

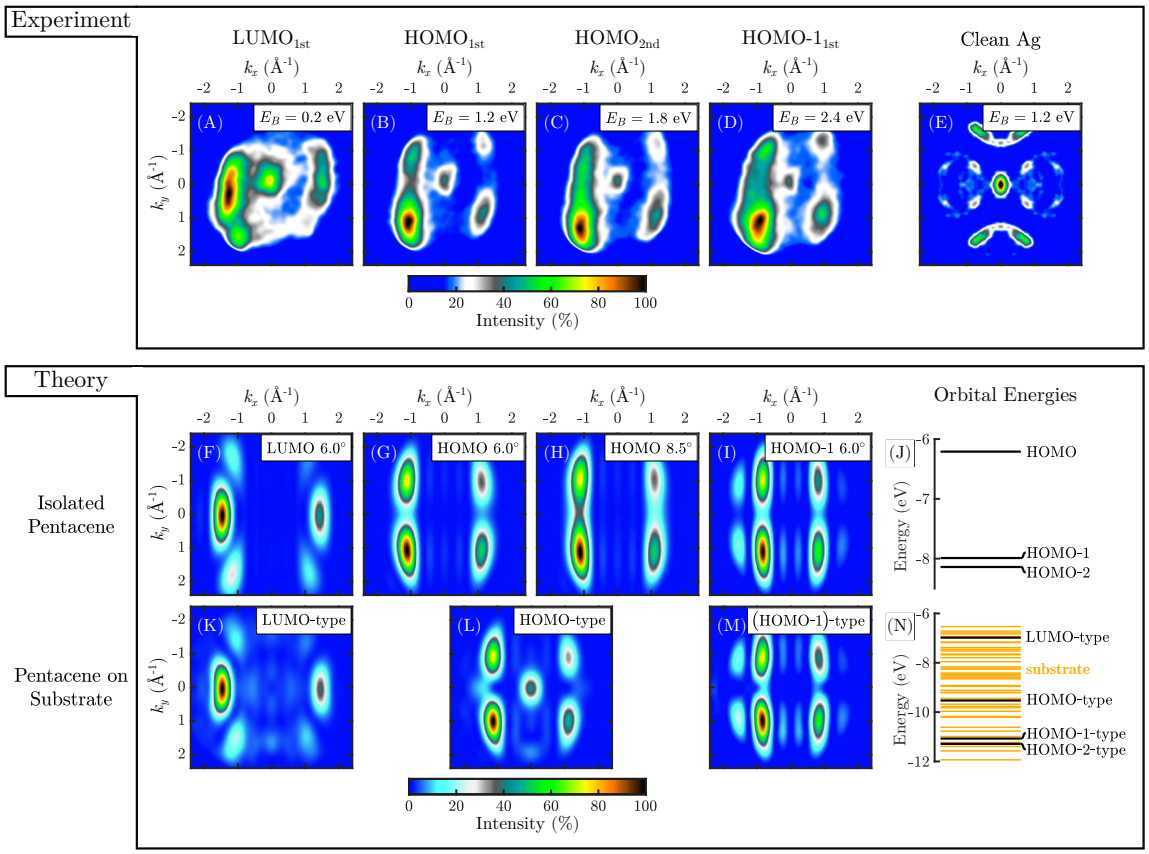


Figure 4.4.: Experimentally measured (A)–(D) and theoretically calculated (F)-(I) and (K)-(M) PMMs for the pentacene valence orbitals involving a probe pulse with the energy of $\omega_{in} = 35$ eV. The experimental data (A)–(D) is time-integrated over all measured time delays between the pump and probe pulse. (E) shows an unexcited, symmetrized PMM of clean Ag(110) at $E_B = 1.2$ eV for comparison. The color scale in (A)-(E) has been adjusted to suppress the background signal. The simulations (F)-(I) show the PMMs obtained from a calculation on isolated pentacene, where the contribution from the LUMO (F) is obtained from the first excited state and the others from the ground state of the molecule. (J) shows the MO energies obtained in the calculation of the ground state. (K)-(M) show the PMMs obtained from the theoretical model of pentacene on the substrate. (N) shows the corresponding MO energies for orbitals with the main contribution in the pentacene (black) and in the substrate (orange). Adapted from Ref. [62].

substrate. The question arises if our model for a single pentacene on the substrate can explain these additional features and how the substrate influences the MOs.

The vertical distance between pentacene and the substrate is experimentally and theoretically unknown for this system. However, we can estimate it with previous studied of the molecule PTCDA adsorbed on silver. The experimental data for the adsorption distance of PTCDA on Ag(111) and pentacene on Ag(111) is similar [154, 155]. This indicates that we can approximately take the distance of PTCDA on Ag(110) as a reference for our system. Experimentally the distance ranges from 2.3 Å to 2.6 Å depending on the specific atom [156].

To evaluate the adsorption distance and to reproduce the experimental data, we calculated PMMs of the model for different adsorption heights. At a vertical distance between pentacene and the substrate of 2.2 Å and lower, we obtain, in agreement with the experiment, an occupied orbital that looks similar to the LUMO of pentacene. Our model for pentacene on the substrate does not include any long-range interaction due to the periodicity of the system. Electronic correlations and in particular, van der Waals interactions are not described within HF [148]. Also, the distance between the molecule and the substrate was not determined by a minimization of the energy (we obtained an increase for lower distances similar to [130]) but rather by the occupation of the LUMO. Therefore, the method used here could slightly underestimate the distance between the molecule and the substrate. However, compared to the distance of PTCDA on Ag(110), it is in a reasonable range. Therefore we set the vertical distance between the pentacene molecules and the substrate atoms in our model to 2.2 Å.

The charge transfer from the substrate into the LUMO indicates a strong interaction between the substrate and the molecule. This interaction is stronger than van der Waals interactions and shows the chemisorption of the pentacene in the first layer. Also, the distance of 2.2 Å in the model is in the range of the covalent radius of C and Ag [157], which indicates a strong interaction and chemisorption [158]. Two different kinds of orbitals appeared in the model of pentacene on the substrate. The first type of orbitals is mainly localized on the silver atoms, while the second type mainly contributes to the pentacene molecule. Three orbitals of the second type with the lowest binding energies are shown in Fig. 4.5 (A)-(C). The changes in the MO due to the substrate are comparable

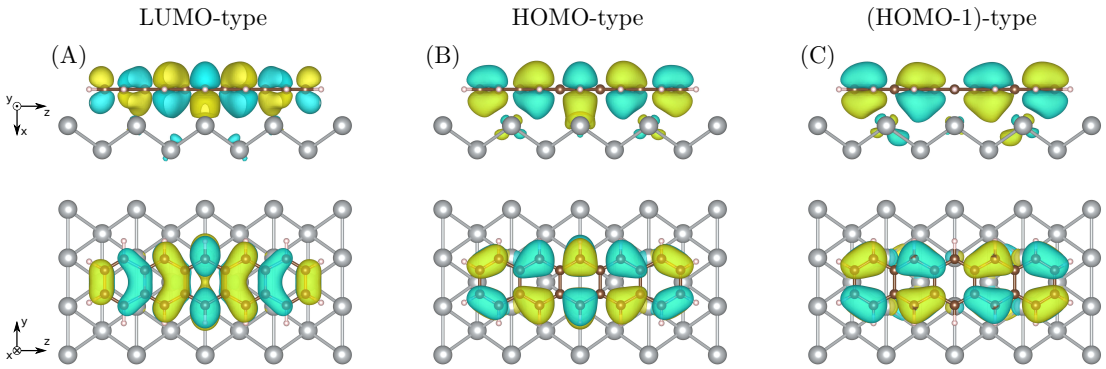


Figure 4.5.: Visualization of the (A) LUMO-, (B) HOMO- and (C) (HOMO-1)-type orbitals for the calculation of pentacene on the substrate. The hydrogen atoms added to the substrate have been removed. The upper row shows the structure from the side view and the lower from the top view. For visualization, we used the software VESTA [150]. Adapted from Ref. [62].

to those obtained for PTCDA on Ag(110) calculated with a more advanced method, second order Møller–Plesset perturbation theory. Even though the orbitals show hybridized bonds between the substrate and the molecule, they are similar to the LUMO, HOMO, and HOMO-1 of the isolated molecule. Therefore we name those orbitals LUMO-type, HOMO-type, and (HOMO-1)-type.

The calculated PMMs resulting from the model of pentacene on the substrate are shown in Fig. 4.4(K)-(M). We integrate the photoelectron distribution 500 meV around the binding energy of the LUMO- HOMO- and (HOMO-1)-type orbital to obtain the PMMs. We removed the contribution from the hydrogen atoms in the substrate. For the PMM in Fig. 4.4(M), we shifted the center of the binding energy slightly to suppress the contribution from the (HOMO-2)-type orbital. The features obtained from isolated pentacene are nearly unchanged in all these PMMs. The major change results from the missing tilt of the molecule. The orbital energies in the model are shifted compared to the calculation of isolated pentacene due to the occupation of the LUMO-type orbital and the influence of the substrate (see Fig. 4.4(N)). However, the relative energies are approximately equal. The orbitals in the model with the major contribution from the substrate are shown in orange in Fig. 4.4(N) and are distributed around the others.

Although our model for pentacene on the substrate is simple, it can reproduce the ad-

ditional feature at the Γ-point in the PMM from the HOMO-type orbital in Fig. 4.4(L). Also, the intensity ratio agrees with the experimental data in Fig. 4.4(B). The feature at the Γ-point does not arise from the HOMO-type orbital. It appears due to the energy integration and is a feature from the orbitals with a major contribution in the substrate. However, the number of silver atoms in this model cannot reproduce the full band structure of the substrate. This mismatch could explain why the feature at the Γ-point is missing for the PMM at the binding energy of the LUMO-type orbital and HOMO-1-type orbital in Fig. 4.4(K) and (M).

### 4.4.2. Time-resolved analysis

Despite the time-integrated data, we want to investigate if time-resolved properties of the system can be obtained from a measurement at a FEL. For the calculation of the time-resolved study, we do not explicitly calculate time-resolved PMMs. We take the calculations on isolated pentacene and the model for pentacene on the substrate and focus on the changes in the PMMs for different geometries of the system.

No photoelectrons stemming from photoexcited states above the Fermi level have been measured in the experiment. Therefore we focus on the changes in the time-resolved photoelectron momentum maps (tr-PMMs) of the initially occupied orbitals. The measured tr-PMMs which could be assigned to the $\mathrm{LUMO}_{1^{\mathrm{st}}}$ and $\mathrm{HOMO}_{1^{\mathrm{st}}}$ are shown in Fig. 4.6(A)-(C) and (D)-(F). The pump-probe delay $\tau_{pp} = -500$ fs is chosen to show the data of the unpumped system.

For a better visualization of the changes, we show the momentum distribution curves, along the white dashed lines in the PMMs of Fig. 4.6, in Fig. 4.7(A) and (B). We see that the pump-pulse induced excitation leads to a decrease of intensity in the signal from the $\mathrm{HOMO}_{1^{\mathrm{st}}}$. For the signal from the $\mathrm{LUMO}_{1^{\mathrm{st}}}$ we first see an increase in the intensity followed by a decrease. We used our model for pentacene on the substrate to understand these dynamics. We calculated the momentum distribution curves from the HOMO-type and LUMO-type orbital (again integrated 500 meV in energy) for different adsorption distances. The results are shown in Fig. 4.7 (C) and (D). We see that the intensity changes with the adsorption distance. The intensity slightly changes for the signal from the LUMO-type orbital, but the signal at the Γ-point in all cases is not pronounced. We

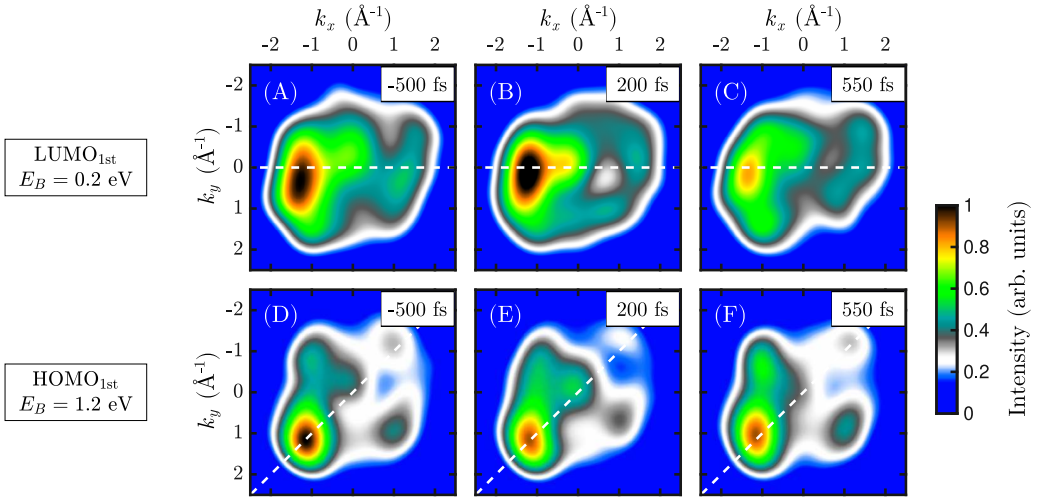


Figure 4.6.: Experimentally measured tr-PMMs for different delays between the pump and probe pulse $\tau_{pp}$ at the binding energies corresponding to the $\mathrm{LUMO}_{1^{\mathrm{st}}}$ with (A) $\tau_{pp} = -500$ fs, (B) $\tau_{pp} = 200$ fs, (C) $\tau_{pp} = 550$ fs, and the $\mathrm{HOMO}_{1^{\mathrm{st}}}$ with (D) $\tau_{pp} = -500$ fs, (E) $\tau_{pp} = 200$ fs, (F) $\tau_{pp} = 550$ fs. The PMMs are integrated in time 350 fs around the delay $\tau_{pp}$ and integrated 500 meV in energy around $E_B$. The white dashed lines show the cut in the PMMs which are used to obtain the momentum distribution curves in Fig. 4.7(A) and (B). Adapted from Ref. [62].

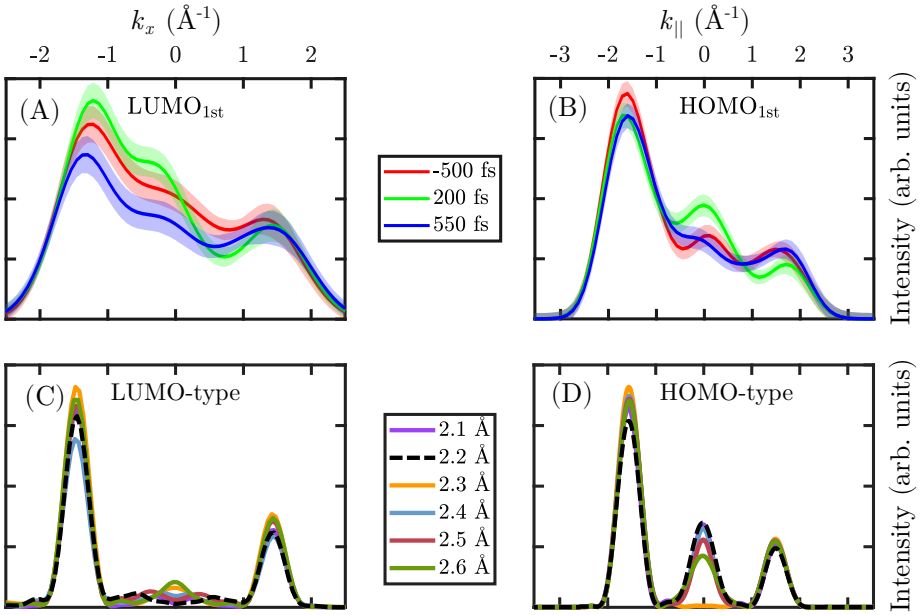


Figure 4.7.: Experimentally measured momentum distribution curves of the photoelectron distributions of the (A) LUMO$_{1^{st}}$ and (B) HOMO$_{1^{st}}$. The blur areas around the lines represent the determined error of the experimental data. The calculated momentum distribution curves (C) from the LUMO-type and (D) HOMO-type orbital are obtained from the model of pentacene on the substrate at different adsorption distances. The curves in (A) and (C) are obtained along a cut in the momentum as indicated by the white dashed line in Fig. 4.6(A)-(C) and for (B) and (D) along a cut indicated by the white dashed line in Fig. 4.6(D)-(F). Adapted from Ref. [62].

see that the changes in the signal at the Γ-point at the binding energy of the HOMO are related to changes in the adsorption distance. The dependence on the adsorption distance indicates that changes in the experimental PMMs at the Γ-point are related to structural changes of the molecule relative to the substrate. The structural changes result from a change in the molecule-substrate interaction upon excitation. The results are also supported by the obtained timescale of the dynamics, which agrees with the ones of atomic motions in molecules [16]. Electronic excitation dynamics on the clean Ag substrate are two orders of magnitude faster [62, 159]. Despite dynamics observed at the Γ-point, charge redistribution between the $\mathrm{LUMO}_{1^{\mathrm{st}}}/\mathrm{HOMO}_{1^{\mathrm{st}}}$ and the substrate can explain the signal changes and overlap with the changes due to geometrical rearrangement. However, the time resolution and quality of the experimental data and the limitations in theoretical calculations did not allow a more detailed investigation of the exact mechanism.

The molecules in the second layer are more electronically decoupled from the substrate, and the experimental data for the $\mathrm{HOMO}_{2^{\mathrm{nd}}}$ (Fig. 4.8(H)) shows a nearly constant intensity at the Γ-point over time. Both indicate a much weaker interaction with the substrate after light excitation and suggest that the dynamics of the molecules in the second layer could resemble the excited state dynamics of the isolated molecule. Therefore we calculate the properties of isolated pentacene at different geometries of the molecule. We assume that the pump pulse excitation brought the pentacene molecule into an excited state. The atoms start to rearrange from the equilibrium geometry of the ground state to the corresponding one for the excited state over time. The first excited state of isolated pentacene $S_1$ has an excitation energy of 2.3 eV, and the second excited state $S_2$ 3.7 eV [160]. Therefore an excitation into the first excited state is much more likely with the pump pulse of 3.1 eV.

We compare the PMM for the vertical first excited state $S_1^*$, where the atoms are still in the position of the ground state, with the geometry-relaxed first excited state $S_1$. These two points in the PES are shown schematically in Fig. 4.8(A) with points B and C. In Fig. 4.8(A), the pink arrow indicates the relaxation down the PES. Interestingly, the geometry relaxation in the first excited state of isolated pentacene results in an intensity increase in the PMM as shown in Fig. 4.8(B),(C), and (D). This intensity increase has two reasons. First, the change in atomic positions results in a small change in the electronic density in the first excited state; second, the final state changes with the rearrangement of the atoms. Therefore the probability for a transition from the initial to the final (in other

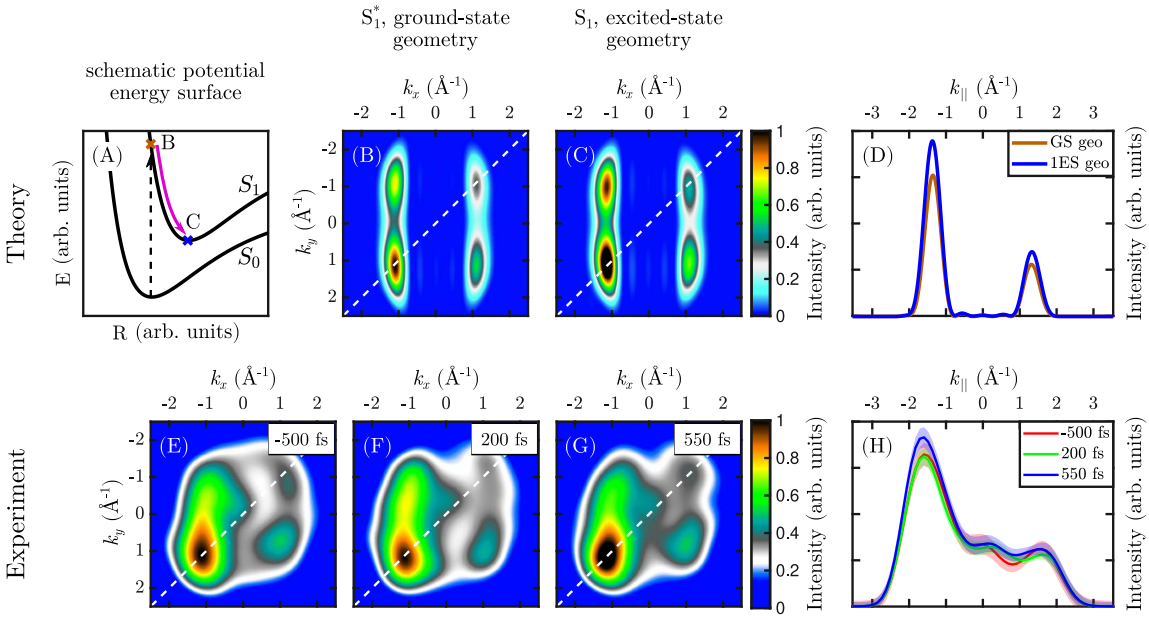


Figure 4.8.: Calculated PMMs (B) and (C) for different points in the PES of the first excited state. The points in the PES are schematically depicted in (A). For comparison, the experimentally measured tr-PMMs at $E_B = 1.8$ eV are shown in (E), (F), and (G) for the shown pump-probe delays. The momentum distribution curves of the theoretical data are shown in (D) and the experimental ones in (H), while the white line in the PMMs shows the direction of the cut in the momentum. Adapted from Ref. [62].

words, the coefficient in the Dyson orbital) increases, causing an increase in the resulting PMM. Despite the increase in intensity, the changes in the PMMs themselves (position of maxima) are small and far less than the experimental resolution in the experiment.

The results agree very well with the experimentally measured features. We also checked the change of the PMM for geometry relaxation of the second excited state of pentacene, but no significant change in the intensity could be obtained. Since the experiment measures an overlap of signals from unexcited and excited molecules, the intensity increase in the experiment is less than in the calculated PMMs. Note that the experimental data for all times overlap with their error and do not allow a strong conclusion here. However, all the results indicate that geometric rearrangements similar to the ones in isolated pentacene are obtained in the experiment. Also, the timescale of the dynamics relates to the timescale of nuclear motion. Due to the obtained lifetimes of the singlet excited states in pentacene dimers of $\approx 500$ fs [161], we can assume that the singlet excited state has not yet decayed. These results indicate the possibility of studying properties of aligned isolated molecules and making it possible to obtain molecular movies without the need to align those in gas phase experiments [162, 163, 164, 62].

## 4.5. Summary

In summary, our combined experimental and theoretical study demonstrates that orbital tomography in the time domain with a time resolution of hundreds of femtoseconds is possible at FEL. We showed that properties obtained from MO of the isolated molecule could be mapped within orbital tomography to the experimental data, even with high-intensity pulses at the FEL. We gained insights into the molecule-substrate interaction and their geometry within our model for pentacene on the substrate. In agreement with the experimental data, we obtained charge transfer into the LUMO and showed that hybridization between the molecular orbitals and substrate states occurs. Moreover, the model reproduces features in the photoelectron distribution resulting from the interplay with the substrate and still captures the properties stemming from the isolated molecule. By investigating the time-dependent changes in the PMMs, we observed that the dynamics of the pentacene molecules in the two different layers significantly differ upon excitation. The molecules in the layer closer to the substrate show a strong dynamical interplay with

the substrate appearing as charge redistribution and geometric changes in the adsorption height. Out-of-plane bending of the molecule could not be investigated due to the limitations of the theoretical model. The pentacene molecules in the topmost layer are electronically decoupled from the substrate. We could reveal that the experimentally obtained changes in the PMMs from the molecules in the topmost layer can be related to geometrical changes similar to the ones expected for an isolated pentacene molecule in the first singlet excited state.

The ongoing development of FEL light sources on the experimental side and further investigation with more sophisticated theoretical approaches make our presented approach an ideal tool for the future. With such an approach, one could resolve dynamic properties between the molecule and the substrate and isolated molecular properties without the need to perform the experiment in the gas phase.

# 5. Ultrafast electronic and structural dynamics of CuPc adsorbed on $TiSe_2$

In this chapter, I present the results of a combined theoretical and experimental study performed on the molecule CuPc, which is adsorbed in the experimental sample on titanium diselenide ($TiSe_2$). With my calculations, I supported the explanation and understanding of the experimental data under the supervision of Daria Gorelova. The whole work is a result of a collaboration with a huge team, while I mainly exchanged information with Kiana Baumgärtner, Christian Metzger, and Markus Scholz. The paper is submitted; the current version is available at [165].

I start with an introduction to the study in Sec. 5.1. I continue with a description of the experimental setup and show information on the sample obtained by our collaborators that are relevant for my calculations in Sec. 5.2. The computational details for excited electronic states and the photoelectron distribution are described in Sec. 5.3. Different scenarios for the excited states of CuPc are discussed in Sec. 5.4. The resulting photoelectron distribution from these excited states of the isolated CuPc allows for gaining insights into the experimentally observed valance band dynamics. In Sec. 5.5, I present my calculations for the angle-integrated photoelectron distributions stemming from core level electrons of neutral and ionized CuPc and compare them to XPS measured in the experiment. I continue in Sec. 5.6 with my theoretical study on structural dynamics due to the charging of the molecules on the surface and compare them with the experimental data. Finally, I summarize the work.

## 5.1. Introduction

The molecule used in this study, CuPc (chemical formula $C_{32}H_{16}CuN_8$), belongs to the class of metal-phthalocyanines (MPc). This class of molecules is interesting for use in organic semiconductors due to their possible growth on thin films, chemical stability, and good charge transport properties. CuPc has been used in different electronic devices such as OSCs [166, 167, 168]. Commercial products use CuPc as a blue pigment [169].

CuPc is a planar molecule with high symmetry ($D_{4h}$ symmetry group). The copper atom in the middle is surrounded by four nitrogen atoms, each belonging to a pyrrole ring. These pyrrole rings are connected via nitrogen atoms. The structure of the molecule is shown in Fig. 5.7. In the outer wings of the molecule are benzene rings, consisting of carbon atoms not bound to the nitrogen atoms. The copper atom in the middle causes an odd number of electrons in the molecule leading to a singly occupied orbital with the 3d character of the Cu and 2p of the connected N atoms [170]. XPS studies revealed different binding energies for the core electrons of the carbon atoms in the molecule due to their non-identical chemical environment [170]. Throughout the work, we discuss further details on the electronic structure of CuPc. In the case of physisorption, the CuPc molecules are distributed with a gas-like behavior on top of the substrate [171, 172, 173]. Gas-like means that by increasing the coverage to a complete monolayer (ML), the molecules on the surface are getting closer together. This growth is a different behavior compared to other systems, e.g., PTCDA which usually first form islands on the substrate due to their attractive van der Waals forces and leave other areas on the substrate uncovered [172]. The adsorption geometry, layer growth, and geometric rearrangement in the system are important for the function of a possible device. Following such dynamics is one goal of this study.

Here CuPc is adsorbed onto $TiSe_2$, a transition-metal dichalcogenide (TMDC). In these layered materials, a transition-metal atom is sandwiched between two layers consisting of chalcogen atoms. Van der Waals interactions bind the layers together. Therefore the substrate can be prepared with a clean surface using exfoliation [174, 175]. $TiSe_2$ has a hexagonal lattice structure and belongs to the $D_{3d}$ point group [176]. Therefore it has a three-fold symmetry, meaning that it is symmetric under rotations of 120°. $TiSe_2$ shows interesting electronic properties like charge density waves (CDWs) [177], where a standing

wave describes the charges in the material. CDWs are interesting because of the proximity to the superconducting phase [178, 179]. The low density of states near the Fermi energy $E_F$ combined with weak bonding between the different layers in $TiSe_2$ makes it sensitive to dynamics at the interface. Also, the behavior of pure $TiSe_2$ after optical excitation has already been studied [54, 180], allowing for disentangling dynamics in the substrate and dynamics happening at the interface. Therefore this material is ideal for obtaining charge transfer processes at the interface and the choice in this study.

In the study, we want to reveal photoinduced dynamics in the molecular layer and at the interface between the molecules and the substrate. My contribution to this work is mostly related to photoemission from isolated CuPc. With properties of the valence states and core level states, we try to explain the experimental data from tr-ARPES, tr-XPS, and tr-XPD experiments. Combining all these methods in the same experiment allows the measurement of valence and core electrons in the same system. The latter is sensitive to the chemical environment of the atoms and structural properties.

## 5.2. Experimental details

We summarize the properties of the experimental setup and the sample, which are important for theoretical calculations. The setup is similar to pentacene on Ag(110) in Ch. 4. The incident angle of the pump and probe beam is the same as shown in Fig. 4.1.

The experiment was performed in 2020 involving HHG sources and the FEL FLASH. The three-dimensional momentum of the emitted photoelectrons is measured with a time-of-flight momentum microscope. For tr-ARPES, a pump pulse with an energy of $\omega = 1.6$ eV and a probe pulse with an energy of $\omega_{in} = 36.3$ eV were used. The results for the valence band dynamics in this work (from tr-ARPES) were all obtained with the HHG source due to higher sampling frequency and better time-resolution in the experiment of $(95 \pm 5)$ fs. The tr-XPD and tr-XPS were performed at FLASH with a probe pulse energy of 370 eV. The time resolution in this experiment is $(180 \pm 10)$ fs. The pump pulse is the same as used in tr-ARPES.

Our collaborators obtained the following sample properties by evaluating the experimental data and comparing those to calculations. We summarize the relevant information for the

calculations in Sec. 5.4-5.6.

The two unit cell vectors of the flat CuPc structure on top of $TiSe_2$ are nearly orthogonal (the angle between them is 93.7°), each with a length of 13.8 Å. These vectors were obtained with low-energy electron diffraction (LEED) performed on the sample with a complete ML coverage. Comparing the size of one CuPc to the size of the unit cell reveals that all molecules must have the same orientation on the substrate in the ground state. The molecules have a point-on-line arrangement on the substrate [173], where one vector of the unit cell in the molecular layer and the substrate are parallel to each other. The structure of the sample used during the time-resolved measurement was not checked with LEED, but the intensity of the PMM assigned to the HOMO allows us to determine a coverage of (0.8-1.0) ML.

Our collaborators found no pronounced hybridization between the MOs and the substrate bands and no charge redistribution in the ground state. In the ground state, the electronic structure of CuPc is occupied up to the HOMO, as expected from the isolated molecule. The tr-PMMs 310 meV below the $E_F$ are assigned to the HOMO of CuPc and is a superposition of signals stemming from the HOMO of the isolated CuPc and $TiSe_2$. Calculations based on DFT showed an adsorption distance between the CuPc and the substrate of 3.16 Å, which corresponds to physisorption [158]. Comparing the experimental data to calculations revealed that CuPc adsorbs in three domains. The adsorption geometry of the molecules in the domains differs by a rotation of the molecules of 120° according to the three-fold symmetry of the substrate. From the symmetry of the system, domains obtained by mirroring the CuPc structure along the symmetry axis of the substrate must be present. However, those are not found from the data of the time-resolved measurement, indicating that either the CuPc molecules are adsorbed such that these mirror domains are equal or the symmetry is broken in some way. We will discuss this in Sec. 5.6.

In the time-resolved measurement, different dynamics could be obtained. The results obtained at the time of excitation, where the pump and probe pulse overlap $t_0 = \tau_{pp} = (0 \pm 100)$ fs, show different signals in the photoelectron distribution above $E_F$. These results reveal that electrons are removed from the Se 4p bands and the HOMO upon excitation, while electrons are excited into Ti 3d bands and a small fraction also into CuPc. The excited electrons in the CuPc decay quickly after excitation with a time constant of

$\tau^{-}_{\mathrm{LUMO}} = (92 \pm 50)$ fs. The signal from the Ti 3d bands increases with a time constant of $\tau^{+}_{\mathrm{Ti3d}} = (243 \pm 50)$ fs and decreases afterwards with $\tau^{+}_{\mathrm{Ti3d}} = (503 \pm 250)$ fs. The signal stemming from photoelectrons removed from the HOMO shows a first decrease with a time constant of $\tau^{-}_{\mathrm{HOMO}} = (220 \pm 50)$ fs and afterward a recovery of the signal within $\tau^{-}_{\mathrm{HOMO}} = (769 \pm 250)$ fs. The comparison of the timescales reveals that the electron is excited from the HOMO into the Ti3d bands.

In the following sections, we will look into the experimental data at specific time points and use the presented calculations to explain the data and gain insights into the processes happening in the system.

## 5.3. Photoelectron distribution and electronic structure of isolated CuPc

The *ab initio* calculations are performed for neutral CuPc and cationic $CuPc^{+}$ in the ground and excited state. For all calculations, we use the RASSCF module implemented in the software program MOLCAS [116], with a truncated ANO-S basis [181] for all atoms, including (4s3p2d1f) contracted atomic basis functions for Cu, (4s3p2d) for N and C and (3s2p) for H. While turning off the orbital optimization in the RASSCF module, we effectively perform a RASCI calculation.

The size of the different orbital spaces (inactive, RAS1, RAS2, RAS3) used in the calculation are shown in Tab. 5.1. The orbital space is chosen such that a further increase in the number of active orbitals does not significantly change the calculated results. For all calculations, the number of orbitals in the RAS2 space is the same, while in this space, all possible occupations in the orbitals are allowed as long as the number of electrons in the whole system is correct. The orbitals in the inactive space are always doubly occupied. In the RAS1/RAS3 space, we allow a maximum number of one hole/electron. All the other orbitals remain unoccupied (secondary).

Three active orbitals in the RAS2 space are particularly interesting for discussing our results. The spatial part of these three RASCI orbital wavefunctions obtained from the ground state of neutral CuPc are shown in Fig. 5.1. We name these HOMO, LUMO, and LUMO′. These are similar to previously obtained orbitals in calculations of isolated CuPc

| Orbital space | Ground state of CuPc | $CuPc^+$ | Excited states of CuPc |
|---|---|---|---|
| Inactive | 145 | 137 | 129 |
| RAS1 | 0 | 8 | 16 |
| max. No. of holes | - | 1 | 1 |
| RAS2 | 4 | 4 | 4 |
| RAS3 | 0 | 6 | 16 |
| max. No. of electrons | - | 1 | 1 |

Table 5.1.: Numbers of orbitals (in different orbital subspaces) used in the RASCI calculations for the ground and excited states of neutral CuPc and $CuPc^+$. Inactive orbitals are always doubly occupied. Orbitals in the RAS1/RAS3 subspace are doubly occupied except for a maximum number of holes/electrons. In the RAS2 subspace, all possible orbital occupations are allowed.

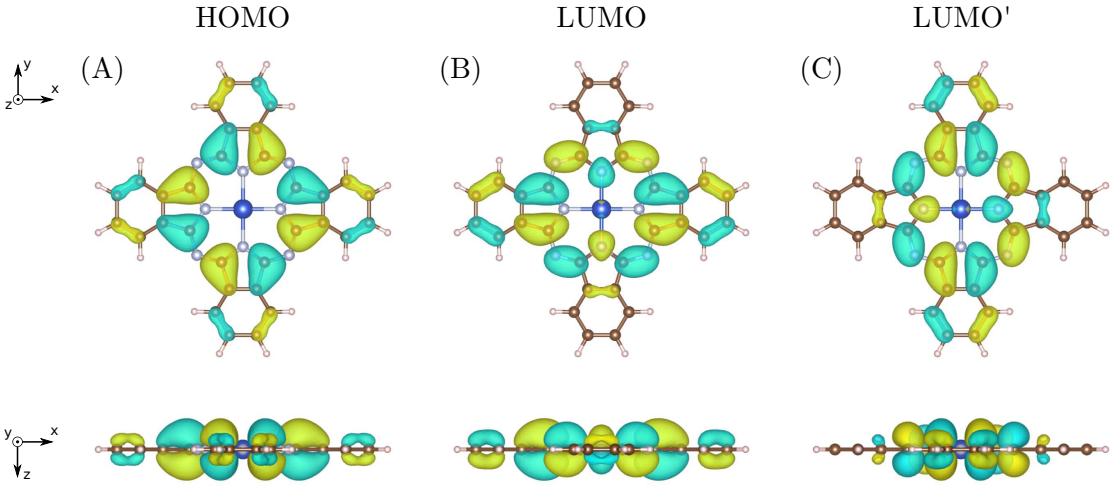


Figure 5.1.: Spatial part of three orbital wavefunctions obtained from the RASCI calculation of neutral CuPc in the ground state. The orbitals correspond to (A) the HOMO and (B), (C) the two degenerate lowest unoccupied molecular orbitals (LUMO and LUMO′). For visualization, we used the software VESTA [150]. Adapted from Ref. [165].

based on DFT [170, 182, 183].

For the ground state of neutral CuPc, we take the geometry from a calculation based on DFT [184]. This geometry is in good agreement with the experimental data of CuPc in the gas phase [185]. We will discuss the different states of CuPc after the interaction with the pump pulse. For the vertical excited/ionized state of CuPc, the atoms did not have time to move according to the fast change in the electronic density. Therefore we use the ground state geometry of neutral CuPc for these states. We refer to the state after the atoms have changed position as the relaxed excited/ionized state. We obtained these states with MOLCAS by optimizing the geometry at the RASCI level [186]. We recover the $D_{4h}$ symmetry after the optimization because MOLCAS cannot handle symmetry groups more complex than $D_{2h}$ and the molecules get slightly disordered in the numerical calculation.

For photoionization from the different states of CuPc, we calculate the corresponding photoelectron momentum distribution with Eq. (3.29). We describe the outgoing photoelectron

within the PWA leading to the photoelectron probability

$$P(\mathbf{q}) \propto |\boldsymbol{\epsilon}_{in} \cdot \mathbf{q}|^2 \sum_{F,\sigma} \delta_{\omega_{in} - E_F^{N_e-1} + E_j^{N_e}, \epsilon_e} \left| \int d^3r \; e^{-i\mathbf{qr}} \phi_F^D(\mathbf{r}) \right|^2, \tag{5.1}$$

where $\mathbf{q}$ is the photoelectron momentum with the corresponding photoelectron energy $\epsilon_e$, $\boldsymbol{\epsilon}_{in}$ is the polarization and $\omega_{in}$ the energy of the photoionizing probe pulse, $E_j^{N_e}$ is the energy of the initial molecular state $\left|\Phi_j^{N_e}\right\rangle$ before removing the photoelectron and $E_F^{N_e-1}$ is the energy of the final molecular state $\left|\Phi_F^{N_e-1}\right\rangle$ after removing the photoelectron. The summation in Eq. (5.1) runs over all possible final states $F$, the function $\delta_{\omega_{in} - E_F^{N_e-1} + E_j^{N_e}, \epsilon_e}$ is for the conservation of energy. The Dyson orbital $\phi_F^D(\mathbf{r})$ is defined in Eq. (3.30).

According to the results in Sec. 5.2 obtained by our collaborators, the molecules are adsorbed in three different domains. Thus the photoelectron distribution is a sum of photoelectrons emitted from the molecules in these domains. Starting from a reference molecular geometry $R_0$, the geometry in the other domains is the same but rotated by an angle of 120° and 240° leading to the geometries $R_{120}$ and $R_{240}$. The photoelectron probability becomes

$$P_D(\mathbf{q}) = P_0(\mathbf{q}) + P_{120^\circ}(\mathbf{q}) + P_{240^\circ}(\mathbf{q}), \tag{5.2}$$

where $P_0(\mathbf{q})$, $P_{120^\circ}(\mathbf{q})$, $P_{240^\circ}(\mathbf{q})$ are the photoelectron probabilities emitted by the molecule with the corresponding geometry $R_0$, $R_{120}$ and $R_{240}$. To improve the signal-to-noise ratio of the data, our experimental collaborators rotated the measured PMMs by an angle of 0°, 120°, and 240° and then averaged these data. Therefore, the resulting PMMs also obey three-fold rotational symmetry in agreement with the symmetry of the substrate. We evaluate the calculated PMMs that they also obey the same rotational symmetry by using the operator for a rotation along the azimuth $\varphi$, $\hat{R}_\varphi$. The total photoelectron distribution becomes

$$P_{total}(\mathbf{q}) = P_D(\mathbf{q}) + P_D(\hat{R}_{120^\circ}\mathbf{q}) + P_D(\hat{R}_{240^\circ}\mathbf{q}). \tag{5.3}$$

## 5.4. Photoelectron imaging of valence states in isolated CuPc

As discussed in Sec. 5.2, our experimental collaborators obtained photoelectrons above $E_F$ when the pump and probe pulse overlap. The time constant indicates a relation between the Ti3d bands and the HOMO. However, an unsolved problem is the occupation of the

excited state in the CuPc. How does it get occupied, and which state is exactly occupied? We want to answer these questions with the following calculations on isolated CuPc.

### 5.4.1. Photoelectron imaging of photo-excited electrons

First, we will discuss the excited states of isolated neutral pentacene. With our calculations on the excited state of isolated neutral CuPc (described in Sec. 5.3), we explain the measured PMM stemming from the CuPc at $t_0$ above $E_F$ by considering three different cases. In case 1, we calculate the distribution of photoelectrons emitted from a CuPc, which has been excited via intramolecular photoexcitation. In case 2, we consider an equal population of two degenerate excited states in the CuPc and calculate the resulting PMM. In case 3, we consider photoelectrons emitted from an emerged orbital.

#### Excited states of neutral CuPc

The two lowest-lying excited states of isolated neutral CuPc are degenerate. Depending on the applied symmetry restrictions in the calculation, the two states are separated in energy by 0.07 meV ($D_{2h}$-symmetry) and 13 meV ($C_{2h}$-symmetry). These two degenerate excited states are described by a CSF with a singly occupied HOMO and LUMO in the first excited state and a singly occupied HOMO and LUMO' in the second excited state. In contrast, contributions from other CSF in both states are negligible. The orbitals in these states correspond to the ones shown in Fig. 5.1. Comparing the orbital occupations in the excited states to the ground state of neutral CuPc, the two degenerate excited states are approximately reached by excitation from one electron in the HOMO to the LUMO/LUMO′. Therefore we label these two states $|\Phi_{1,L}\rangle$ and $|\Phi_{1,L'}\rangle$. The calculated excited states have an excitation energy of approximately 1.1 eV, in agreement with other calculations on CuPc [187] and in the range of the experimental value $(1.4 \pm 0.3)$ eV for CuPc in a thin film (1 nm thick) [188].

For calculating the PMMs, we need to calculate all possible final states after the probe pulse removes photoelectrons. Those states are given by ionized CuPc and ionized $CuPc^+$. The measured photoelectrons above the Fermi level originate from the electrons excited by the pump pulse. In the calculations, we focus on photoelectrons with lower binding energy than in the ground state of neutral CuPc. We find one final state for which a

transition from the two excited states of neutral CuPc is possible by ionization. This final state $F_1$ includes a CSF with a singly occupied HOMO and unoccupied LUMO and LUMO'. The contributions from other CSFs are small. With these considerations, the Dyson orbital in Eq. (5.1) for the first excited state $|\Phi_{1,L}\rangle$ is approximately equal to the orbital wavefunction of the LUMO $\phi_L(\mathbf{r})$, while for the second excited state, it is equal to the orbital wavefunction of the LUMO' $\phi_{L'}(\mathbf{r})$

$$\phi_L^D(\mathbf{r}) = \left\langle \Phi_{F_1}^{N_e-1} \middle| \hat{\psi}(\mathbf{r}) \middle| \Phi_{1,L} \right\rangle \propto \phi_L(\mathbf{r}), \tag{5.4}$$

$$\phi_{L'}^D(\mathbf{r}) = \left\langle \Phi_{F_1}^{N_e-1} \middle| \hat{\psi}(\mathbf{r}) \middle| \Phi_{1,L'} \right\rangle \propto \phi_{L'}(\mathbf{r}). \tag{5.5}$$

**Case 1: Signal resulting from an intramolecular photoexcitation**

In the isolated molecule, the population of the two degenerate excited states can differ because of the polarization of the pump pulse. If the excitation mechanism in the experiment is similar to an excitation of an isolated molecule, the calculation results would agree with the experimental data.

With the interaction Hamiltonian $\hat{H}_{int}$ in Eq. (2.30) and first-order time-dependent perturbation theory, the excited state after the interaction of the pump pulse is considered as

$$|\Phi\rangle_{impe} \propto |\Phi_{1,L}\rangle \langle \Phi_{1,L}| \, \boldsymbol{\epsilon}_p \cdot \hat{\mathbf{p}} \, |\Phi_0\rangle + |\Phi_{1,L'}\rangle \langle \Phi_{1,L'}| \, \boldsymbol{\epsilon}_p \cdot \hat{\mathbf{p}} \, |\Phi_0\rangle \tag{5.6}$$

$$= \boldsymbol{\epsilon}_p \cdot \left( \langle \Phi_{1,L}| \, \hat{\mathbf{p}} \, |\Phi_0\rangle \right) |\Phi_{1,L}\rangle + \boldsymbol{\epsilon}_p \cdot \left( \langle \Phi_{1,L'}| \, \hat{\mathbf{p}} \, |\Phi_0\rangle \right) |\Phi_{1,L'}\rangle , \tag{5.7}$$

where $\boldsymbol{\epsilon}_p$ is the polarization of the pump pulse, $\hat{\mathbf{p}}$ is the momentum operator and $|\Phi_0\rangle$ the ground state of neutral CuPc. The probability for the transition from the ground state to one of the excited states is related to the product of the pump pulse polarization and the transition dipole matrix elements ($\langle \Phi_{1,L}| \, \hat{\mathbf{p}} \, |\Phi_0\rangle$ and $\langle \Phi_{1,L'}| \, \hat{\mathbf{p}} \, |\Phi_0\rangle$) for a transition from the ground state to one of the two excited states. For our calculation, we obtain

$$\begin{aligned} \langle \Phi_{1,L}| \, \hat{\mathbf{p}} \, |\Phi_0\rangle &= \boldsymbol{\mu} = -(\mu_0, 0, 0), \\ \langle \Phi_{1,L'}| \, \hat{\mathbf{p}} \, |\Phi_0\rangle &= \boldsymbol{\mu'} = (0, \mu_0, 0). \end{aligned} \tag{5.8}$$

The two degenerate excited states are orthogonal with different transition dipole matrix elements. Thus the excitation by the pump pulse will create a superposition of both of the

excited states described as

$$|\Phi_{impe}\rangle \propto \boldsymbol{\epsilon}_p \cdot \boldsymbol{\mu} \, |\Phi_{1,L}\rangle + \boldsymbol{\epsilon}_p \cdot \boldsymbol{\mu}' \, |\Phi_{1,L'}\rangle \, . \tag{5.9}$$

The corresponding Dyson orbital is

$$\phi^D_{impe}(\mathbf{r}) \propto (\boldsymbol{\epsilon}_p \cdot \boldsymbol{\mu})\phi_{1,L}(\mathbf{r}) + (\boldsymbol{\epsilon}_p \cdot \boldsymbol{\mu}')\phi_{1,L'}(\mathbf{r}). \tag{5.10}$$

Note that the Dyson orbital in Eq. (5.10) changes for a molecule rotation because the transition dipole moment in the laboratory frame changes. The photoelectron probability for the photoelectron emitted from the excited state by assuming an intramolecular photoexcitation is

$$P(\mathbf{q}) \propto |\boldsymbol{\epsilon}_{\text{in}} \cdot \mathbf{q}|^2 \left| \int d^3r \; e^{-i\mathbf{q}\cdot\mathbf{r}} \phi^D_{impe}(\mathbf{r}) \right|^2 , \tag{5.11}$$

where $\boldsymbol{\epsilon}_{\text{in}}$ is the polarization of the probe pulse. With the three different adsorption directions of the CuPc, the photoelectron probability becomes

$$\begin{aligned} P_{impe}(\mathbf{q}) \propto |\boldsymbol{\epsilon}_{\text{in}} \cdot \mathbf{q}|^2 \Big\{ & \Big| \int d^3r \; e^{-i\mathbf{q}\cdot\mathbf{r}} \left[ (\boldsymbol{\mu} \cdot \boldsymbol{\epsilon}_p)\phi_L(\mathbf{r}) + (\boldsymbol{\mu}' \cdot \boldsymbol{\epsilon}_p)\phi_{L'}(\mathbf{r}) \right] \Big|^2 \\ & + \Big| \int d^3r \; e^{-i\mathbf{q}\cdot\mathbf{r}} \left[ (\hat{R}_{120^\circ}\boldsymbol{\mu} \cdot \boldsymbol{\epsilon}_p)\phi_L(\hat{R}_{120^\circ}\mathbf{r}) + (\hat{R}_{120^\circ}\boldsymbol{\mu}' \cdot \boldsymbol{\epsilon}_p)\phi_{L'}(\hat{R}_{120^\circ}\mathbf{r}) \right] \Big|^2 \\ & + \Big| \int \; d^3r \; e^{-i\mathbf{q}\cdot\mathbf{r}} \left[ (\hat{R}_{240^\circ}\boldsymbol{\mu} \cdot \boldsymbol{\epsilon}_p)\phi_L(\hat{R}_{240^\circ}\mathbf{r}) + (\hat{R}_{240^\circ}\boldsymbol{\mu}' \cdot \boldsymbol{\epsilon}_p)\phi_{L'}(\hat{R}_{240^\circ}\mathbf{r}) \right] \Big|^2 \Big\} . \end{aligned} \tag{5.12}$$

where $\hat{R}_\varphi$ is the rotation matrix along the azimuth $\varphi$. Additionally, we apply the three-fold rotational symmetry (Eq. (5.3)). The resulting PMM is shown in Fig. 5.2(A), which has three-fold rotational symmetry and three maxima. The measured PMM resulting from the excited state has approximately six-fold rotational symmetry and six maxima (excluding the maxima at the Γ-point) as shown in Fig. 5.4(C). The mismatch between the experimental and theoretical results excludes an intramolecular excitation.

#### Case 2: Signal assuming an equal population of both excited states

Now we have a structure with molecules where both degenerate excited states are equally populated. In this case, we sum up the PMMs from both states

$$P(\mathbf{q}) \propto |\boldsymbol{\epsilon}_{\text{in}} \cdot \mathbf{q}|^2 \left( \left| \int d^3r \; e^{-i\mathbf{q}\cdot\mathbf{r}} \phi_L(\mathbf{r}) \right|^2 + \left| \int d^3r \; e^{-i\mathbf{q}\cdot\mathbf{r}} \phi_{L'}(\mathbf{r}) \right|^2 \right) . \tag{5.13}$$

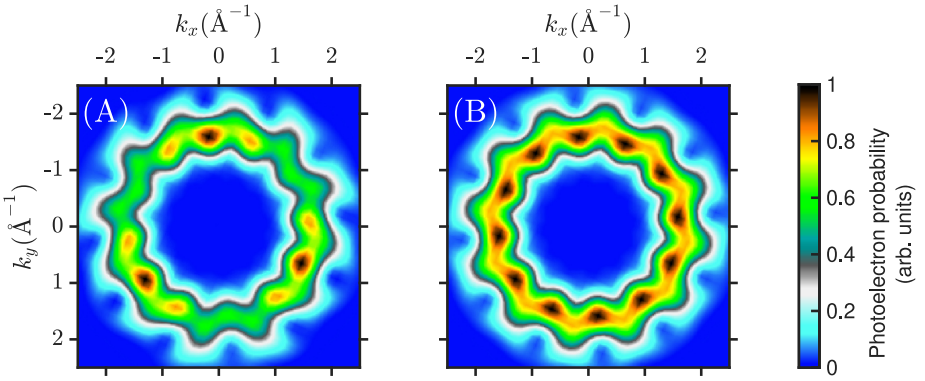


Figure 5.2.: PMM of excited isolated neutral CuPc resulting from photoionizing the least bound electron under the assumption (A) of an intramolecular excitation, (B) that the two degenerate excited states are equally populated. Adapted from Ref. [165].

The resulting PMM is shown in Fig. 5.2(B). This PMM has twelve-fold symmetry with 12 maxima, which does not match the experimentally measured PMM in Fig. 5.4(C). Therefore we can also exclude this type of excitation.

### Case 3: Symmetry breaking in the excited state of CuPc

The previous results exclude an intramolecular excitation from HOMO to LUMO in the experiment. In this section, we assume that the four-fold rotational symmetry of the excited state in isolated CuPc breaks on the three-fold rotational symmetric substrate. Such a symmetry breaking of the excited state in CuPc onto a substrate has already been observed [189, 190]. In this case, new states could emerge, which are superpositions of $|\Phi_{1,L}\rangle$ and $|\Phi_{1,L'}\rangle$

$$|\Phi_1\rangle = \sin\alpha\,|\Phi_{1,L}\rangle + \cos\alpha\,|\Phi_{1,L'}\rangle \tag{5.14}$$

$$|\Phi_2\rangle = -\cos\alpha\,|\Phi_{1,L}\rangle + \sin\alpha\,|\Phi_{1,L'}\rangle\,, \tag{5.15}$$

where $\alpha$ is a parameter that determines the linear combination. The two states $|\Phi_1\rangle$ and $|\Phi_2\rangle$ are orthogonal. The Dyson orbitals for photoionizing the least bound electron from

these states are

$$\phi_1^D(\mathbf{r}) = \left\langle \Phi_{F_1}^{N_e-1} \middle| \hat{\psi}(\mathbf{r}) \, |\Phi_1\rangle \propto \sin\alpha\phi_L(\mathbf{r}) + \cos\alpha\phi_{L'}(\mathbf{r}) \right. \tag{5.16}$$

$$\phi_2^D(\mathbf{r}) = \left\langle \Phi_{F_1}^{N_e-1} \middle| \hat{\psi}(\mathbf{r}) \, |\Phi_2\rangle \propto -\cos\alpha\phi_L(\mathbf{r}) + \sin\alpha\phi_{L'}(\mathbf{r}). \right. \tag{5.17}$$

If we assume an occupation similar to the one considered in Case 2, but with an equal occupation of $|\Phi_1\rangle$ and $|\Phi_2\rangle$ the resulting PMM is given by

$$\begin{aligned} P(\mathbf{q}) &\propto |\boldsymbol{\epsilon}_{\text{in}} \cdot \mathbf{q}|^2 \left( \left| \int d^3r \; e^{-i\mathbf{q}\cdot\mathbf{r}} \phi_1^D(\mathbf{r}) \right|^2 + \left| \int d^3r \; e^{-i\mathbf{q}\cdot\mathbf{r}} \phi_2^D(\mathbf{r}) \right|^2 \right) \\ &= |\boldsymbol{\epsilon}_{\text{in}} \cdot \mathbf{q}|^2 \left( \left| \int d^3r \; e^{-i\mathbf{q}\cdot\mathbf{r}} [\sin\alpha\phi_L(\mathbf{r}) + \cos\alpha\phi_{L'}(\mathbf{r})] \right|^2 \right. \\ &\qquad \left. + \left| \int d^3r \; e^{-i\mathbf{q}\cdot\mathbf{r}} [-\cos\alpha\phi_L(\mathbf{r}) + \sin\alpha\phi_{L'}(\mathbf{r})] \right|^2 \right) \\ &= |\boldsymbol{\epsilon}_{\text{in}} \cdot \mathbf{q}|^2 \left( \left| \int d^3r \; e^{-i\mathbf{q}\cdot\mathbf{r}} \phi_L(\mathbf{r}) \right|^2 + \left| \int d^3r \; e^{-i\mathbf{q}\cdot\mathbf{r}} \phi_{L'}(\mathbf{r}) \right|^2 \right). \end{aligned} \tag{5.18}$$

The expression for the photoelectron distribution in Eq. (5.18) is independent of the value of $\alpha$ and is equal to Eq. (5.13). The resulting PMM is the same as shown in Fig. 5.2(B), which we already excluded.

Instead, we consider that only one of the two states gets occupied, $|\Phi_1\rangle$. The resulting PMMs obtained from photoionizing the state $|\Phi_1\rangle$ for different values of $\alpha$ are shown in Fig. 5.3. Due to the value of $\alpha$, Fig. 5.3(A) and (S) shows the PMM resulting from removing the photoelectron from the LUMO' and Fig. 5.3(J) from the LUMO. All other PMMs in Fig. 5.3 are obtained from linear combinations of $|\Phi_1\rangle$ and $|\Phi_2\rangle$. The PMMs have six maxima and six-fold rotation symmetry in agreement with the measured spectra. The PMM in Fig. 5.3D, for which $\alpha = \frac{\pi}{6}$, has the best agreement with the experimental data and results from the state

$$|\Phi_{1ES}\rangle_D = 0.5 \, |\Phi_{1,L}\rangle + \frac{\sqrt{3}}{2} \, |\Phi_{1,L'}\rangle \, . \tag{5.19}$$

The spatial part of this orbital is shown in Fig. 5.4(A). For comparison the calculated PMM is shown in Fig. 5.4(B) and the experimentally measured PMM in Fig. 5.4(C). We see that the maxima and the fine structure in the PMM agree. In the experimental data, we removed the signal at the Γ-Point stemming from the substrate for comparison.

With this result, we conclude that the substrate influences the excited state of the CuPc in the system. Since the results exclude an intramolecular photoexcitation, the excited

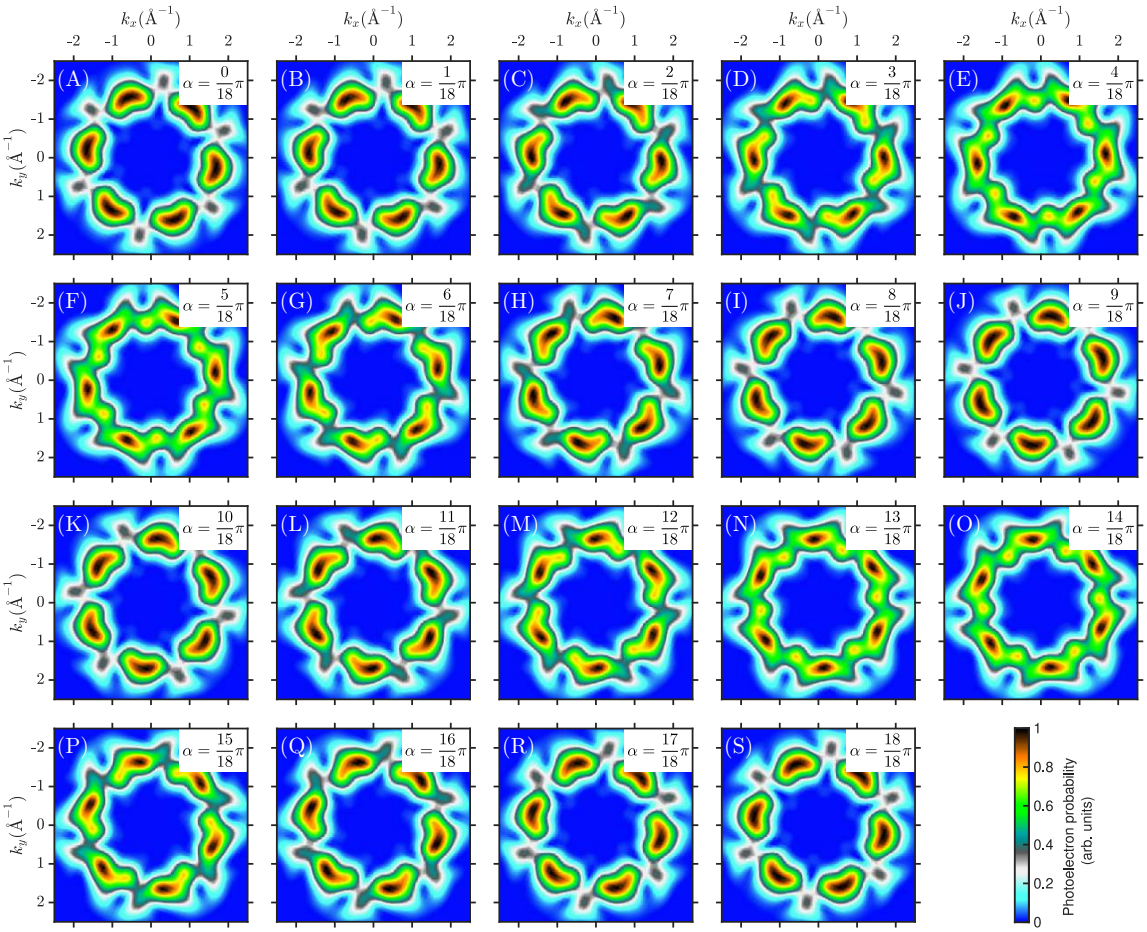


Figure 5.3.: PMMs resulting from different excited states where the photoelectron is emitted from an emerged orbital $\phi_1^D(\mathbf{r}) = \sin\alpha\phi_L(\mathbf{r}) + \cos\alpha\phi_{L'}(\mathbf{r})$, where the parameter $\alpha$ determines the superposition of the two orbitals $\phi_L(\mathbf{r})$ and $\phi_{L'}(\mathbf{r})$. The values of $\alpha$ are given in the PMMs. Adapted from Ref. [165].

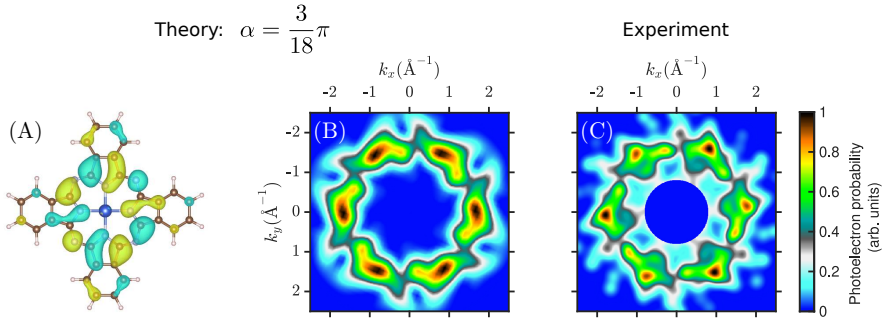


Figure 5.4.: (A) Spatial distribution of the orbital $\phi_D = 0.5\phi_L(\mathbf{r}) + \frac{\sqrt{3}}{2}\phi_{L'}(\mathbf{r})$ with (B) the corresponding PMM obtained from emitting photoelectrons from this orbital. (C) Experimental PMM resulting from photoelectrons measured above $E_F$ that originates from CuPc. The experimental data is smoothed with a Gaussian filter, and for better comparison, the intensity at the Γ-point has been removed. For visualization of (A), we used the software VESTA [150]. Adapted from Ref. [165].

state in CuPc is most likely populated due to so-called hot electron transfer from the substrate, which results in a symmetry breaking of the excited state. "Hot electrons", or more generally, "hot charge carriers", refers to the effective temperature of the charge carriers upon excitation, meaning that they can reach high kinetic energies. The mechanism of hot electron transfer into the molecule requires a hybridization of the orbitals in the CuPc with the substrate, which is weak in the case of physisorption and induced by van der Waals forces [191, 192, 193]. Such a symmetry breaking of the excited state in CuPc has also been observed in systems where CuPc is stronger bound to the surface (e.g., CuPc on Cu(111)) [189, 173, 190, 194]. A charge transfer from the substrate to CuPc in the ground state provides information about the orbitals occupied above the HOMO without performing a time-resolved experiment. In our case, the molecule is much less bound to the substrate, and we could obtain a population of CuPc time-resolved. Even though the occupied LUMO has two-fold symmetry, the calculations of our collaborators show that the geometry and electronic structure of CuPc have a four-fold symmetry before the pump pulse excites the system.

## 5.5. Core level photoelectron spectroscopy in isolated CuPc

In the previous section, we focused on imaging excited states in CuPc using angular distributions of photoelectrons. We now want to focus on photoelectrons emitted from the core levels of CuPc, which resolves site-specific information about the atoms. As already mentioned in Sec. 5.2, the excited state in CuPc decayed after the excitation with a time constant of $\tau_{\mathrm{LUMO}} = (92 \pm 50)$ (exponential fit in the experimental data). The data reveals an ongoing depopulation of the HOMO after the excitation, which is slower. Simultaneously to the depopulation of the HOMO, the signal from the tr-XPS measurement at the binding energy of the C1s core-level decrease. New signals from the C1s core levels appeared at shifted binding energy. The intensity from the HOMO of CuPc reaches its minimum around $t_1 = \tau_{pp} = 375$ fs after the excitation. At the same time the population of the Ti 3d states reaches its maximum, leading to the conclusion that charge is transferred from the molecule into the substrate. This charge transfer leaves a fraction of the molecules ionized. With a calculation on isolated neutral $CuPc^0$ and ionized $CuPc^+$, we want to explain experimental features and relate them to properties of isolated CuPc. The parameters used for the RASCI calculation are described in Sec. 5.3.

### 5.5.1. Extended Koopmans' theorem

Koopmans' theorem lets us obtain the ionized state from a closed-shell HF reference state. It is not applicable for open-shell states and states described within CI. The extended Koopmans' theorem (EKT) [195, 196, 197], states that the wavefunction of the ground state containing $N_e$-electrons $\left|\Psi^{N_e}\right\rangle$ can describe the state of the ionized $N_e - 1$ electronic system

$$\left|\Psi^{N_e-1}\right\rangle = \hat{q}_k \left|\Psi^{N_e}\right\rangle, \tag{5.20}$$

where $\hat{q}_k = \sum_j c_{jk}\hat{c}_j$ is a linear combination of annihilation operator $\hat{c}_j$ of orbital $j$ in the system. The ionization energy is given by

$$I^{EKT} = E^{N_e-1} - E^{N_e} = \frac{\left\langle \Psi^{N_e}\right| \hat{q}^\dagger \left[\hat{H}, \hat{q}\right] \left|\Psi^{N_e}\right\rangle}{\left\langle \Psi^{N_e}\right| \hat{q}^\dagger \hat{q} \left|\Psi^{N_e}\right\rangle}, \tag{5.21}$$

where $E^{N_e}/E^{N_e-1}$ is the energy of the $N_e/(N_e-1)$ electron system and $\hat{H}$ the Hamilton operator. In the case where the $N_e$-electronic wavefunction $\left|\Psi^{N_e}\right\rangle$ is exact, $I^{EKT}$ gives

the correct ionization potential of state $k$. In [198], it has been shown that the EKT also provides ionization energies from wavefunctions computed in the complete active space self-consistent field (CASSCF) approach.

### 5.5.2. Computational details

For the ionization of electrons from core orbitals, we approximate the wavefunction $\left|\Psi^{N_e-1}\right\rangle_j = \hat{c}_j \left|\Psi^{N_e}\right\rangle$, where $j$ is the index of the core orbital. In this approach, we neglect relaxation of the final state $\left|\Psi^{N_e-1}\right\rangle_j$. The core orbitals in our RASCI calculation are in the inactive space, providing us with orbital energies. We assume that the state $\left|\Psi^{N_e}\right\rangle$ is an eigenstate of the Hamiltonian $\hat{H}$. Using EKT, we assume that the orbital energy $\epsilon_j$ is the binding energies of the electrons, corrected by a value caused by electron-electron interactions [199]. The correct ionization potential might be shifted [199, 198] by a value $E_{coor}$

$$I_j^{N_e} = -\epsilon_j - E_{coor}, \tag{5.22}$$

where $\epsilon_j$ is the energy of an inactive orbital obtained from the RASCI calculation.

We use Eq. (5.22) to describe the ionization of the core orbitals from neutral CuPc. We describe the binding energies of the electrons in the core orbitals of $CuPc^+$ similarly but add an additional energy shift caused by the correlation of the electrons in $CuPc^+$, $E_{coor}^{CuPc^+}$. The ionization potential from the core levels of $CuPc^+$ is

$$I^{N_e-1} = -\epsilon_j - (E_{coor} + E_{coor}^{CuPc^+}). \tag{5.23}$$

In both cases, we assume that the electronic correlations $E_{coor}$ are equal for all atoms in the calculation of $CuPc^+$ and ionized $CuPc^+$. Note that this approach is an approximation. Ideally, one obtains the ionization potential by the energy difference between the neutral and ionized state (with a hole in the core orbitals). Electronic correlations can be included with higher excitations in the CI approach and perturbation theory. In our case, this is computationally too demanding and not possible for the large molecule CuPc. Furthermore, calculating the electronic structure of the molecules with a hole at a single atom breaks the symmetry, leading to an even higher computational afford. Therefore we fit the energy shift parameters ($E_{coor}$, $E_{coor}^{CuPc^+}$) to the experimental data. Even if the calculations on the isolated molecule could be performed exactly, it does not capture the

interaction of the substrate and a fitting to be experimental data needs to be applied.

For the simulation of the C1s core spectra, we numerically integrate the photoelectron distribution in Eq. (5.1) over the momentum for fixed photoelectron energies $\epsilon_e = |\mathbf{q}^2|/2$. We replace the Dyson orbital $\phi_F^D(\mathbf{r})$ with the calculated molecular core orbitals.

### 5.5.3. Results and comparison

The calculated and measured angle-integrated photoelectron distributions from C1s core levels are shown in Fig. 5.5. The spectra from $CuPc^0$ in Fig. 5.5(A) are shifted by $E_{coor} = +21.6$ eV to agree with the experimental data in Fig. 5.5(E). The additional shift in the spectra for $CuPc^+$ is $E_{coor}^{CuPc^+} = 1.74$ eV. The surface of the substrate is charged at $t_1$. Our collaborators observed that this causes an additional shift of $E_{surf} = 260$ meV in the spectra. For Fig. 5.5(C) and (D), the total shift of the spectra from $CuPc^0$ is $E_{coor} + E_{surf} = 21.86$ eV and from $CuPc^+$ is $E_{coor} + E_{coor}^{CuPc^+} + E_{surf} = 23.6$ eV to agree with the experimental data in Fig. 5.5(F).

The spectra in Fig. 5.5(A) show two main peaks. The left (smaller) one stems from the carbon atoms in CuPc connected to the nitrogen atoms, and we call those $C_N$ (marked in Fig. 5.6(A)). The right peak (higher intensity) results from the carbon atoms in the benzene rings, which we name $C_B$. The intensity between these two peaks has approximately the same ratio of 1:3 as the number of atoms contributing to each peak. The calculated spectra (Fig. 5.5(A)) show good agreement with a previous study on CuPc [170] and the experimental data obtained by our collaborators shown in Fig. 5.5(F). However, the position and ratio of the intensities between the left and right peaks slightly differ in the calculation and the experiment. It has already been shown that satellite peaks from the $C_B$ are responsible for the higher intensity in the left peak [170], which we do not model here. The mismatch in the distance between the left and right peaks results from approximating the binding energy as MO energies.

The calculated C1s core spectra from $CuPc^+$ in Fig. 5.5(B) do not significantly change before and after optimizing the geometry of the atoms. Compared to the core spectra from $CuPc^0$, (Fig. 5.5(A)) the peaks stemming from the $C_B$ (right peak) are shifted by 0.6 eV towards higher binding energies, while the core spectra from the $C_N$ atoms (left peak) are shifted stronger by 1.6 eV towards higher binding energies. Therefore the separation

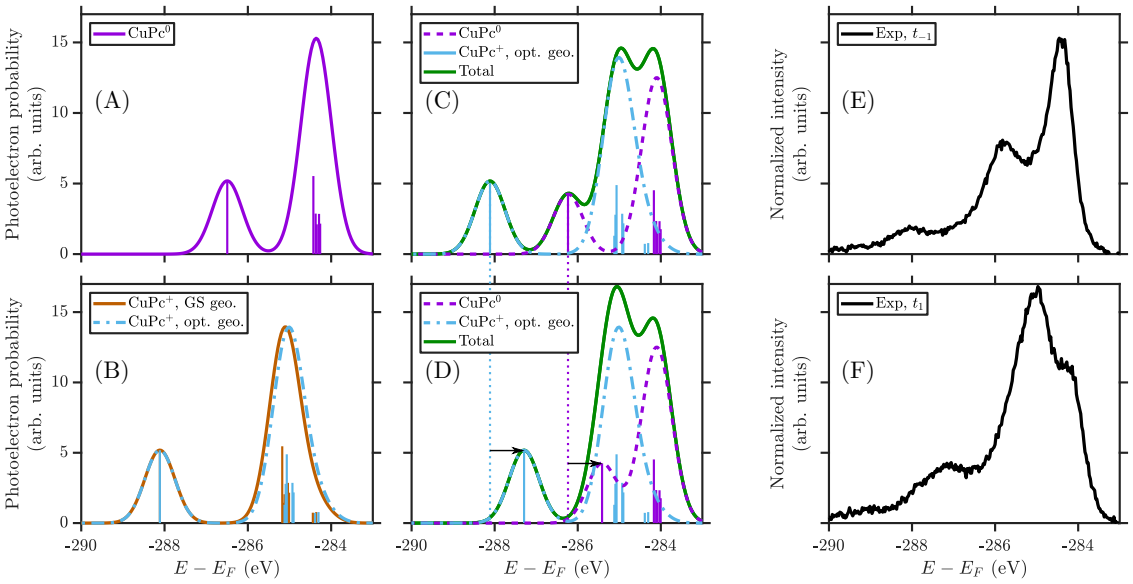


Figure 5.5.: Simulated C1s core photoelectron spectra of (A) the neutral molecule $CuPc^0$, (B) the ionized molecule $CuPc^+$ in the ground-state geometry of $CuPc^0$ and the geometry in which the atoms relaxed to the electronic state of $CuPc^+$. The spectra are shifted by (A) 21.6 eV and (B) 23.6 eV so that the most intense peak agrees with the experimental data. (C) sum of the photoelectron spectra resulting from 45% $CuPc^0$ and 55% $CuPc^+$ in the relaxed geometry. (D) is the same as in (C), but the position of the left peaks of $CuPc^0$ and $CuPc^+$ are shifted by the same value of 820 meV indicated by the black arrows. In (C) and (D), an additional shift of 260 meV was applied to the spectra from $CuPc^0$ due to the negative surface charge obtained in the experiment. The lines in (A)-(D) show the contribution of individual core orbitals according to their binding energy and intensity. The peak width (standard deviation in the Gaussian distribution) of the C1s core spectra is set to 0.36 eV for agreement with the experimental data. The experimental XPS for the pump probe delay times of (E) $t_{-1} = -700$ fs and (F) $t_1 = 375$ fs. Adapted from Ref. [165].

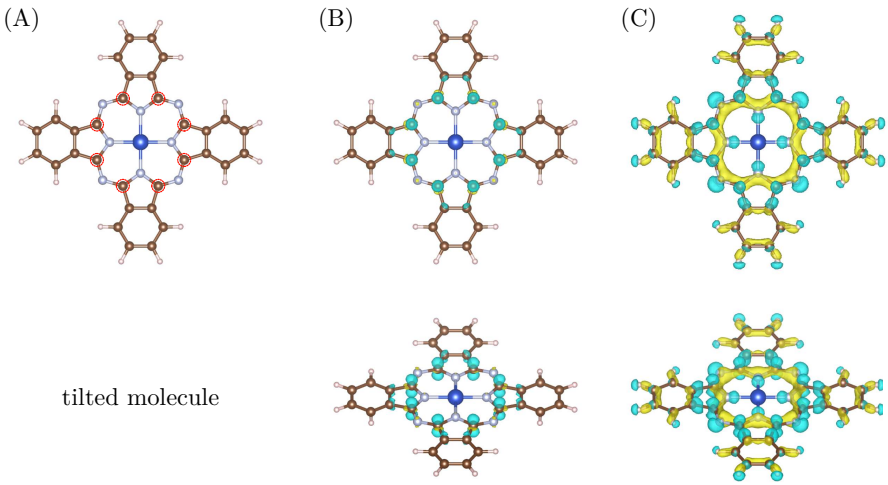


Figure 5.6.: (A) Atomic structure of CuPc where the $C_N$ atoms are marked with red circles. Difference between the charge density of $CuPc^0$ and $CuPc^+$ (B) for both molecules in the ground state geometry of $CuPc^0$, $\rho^+_{GSG} - \rho^0$ and (C) for both molecules each in their optimized geometry, $\rho^+_{ISG} - \rho^0$. The blue isosurface represents a positive and the yellow a negative value. The density difference is shown from the top (upper) and tiled (lower) view of the molecule. For visualization, we used the software VESTA [150]. Adapted from Ref. [165].

between the left and the right peak increases upon ionization by approximately 1 eV, which is related to the changes in the Coulomb potential around the atoms. Further, we obtain a broadening of the right peak by $\approx 4\%$ together with a slight intensity decrease.

To elaborate why the binding energies of the $C_B$ and $C_N$ atoms change differently, we plot the difference between the electronic density of $CuPc^0$ ($\rho^0$) with the one of $CuPc^+$ in the ground state geometry of $CuPc^0$ ($\rho^+_{GSG}$) in Fig. 5.6(B). The positive charge (blue isosurface) is mainly localized on the $C_N$ atoms. Therefore the $C_N$ atoms experience a larger change of the Coulomb potential than the $C_B$ atoms in $CuPc^+$, causing a larger shift of the left peak in the core spectra. Additionally, we see a tiny change in the electronic density around the atoms of the benzene ring (Fig. 5.6(B)). Upon ionization of CuPc, the carbon atoms in the benzene ring that are closer to the copper atom experience a different change in the Coulomb potential than the other carbon atoms in the benzene ring that are further away from the copper atom. This small change causes a slightly larger shift in the binding energies of the benzene atoms closer to the copper than the others, leading to a small broadening in the right peak of the core spectra.

The difference between $\rho^0$ and the electron density of $CuPc^+$ after geometry relaxation, $\rho^+_{ISG}$, is shown in Fig. 5.6(C). The changes in the electronic density by ionization now overlap with the much higher change in the electron density caused by the geometry rearrangement of the atoms. The ionization of $CuPc^0$ causes a maximum change of 1/8 electrons at each $C_N$, while atomic rearrangement of e.g., carbon atoms causes approximately six electrons to move. Therefore Fig. 5.6(C) is not suited to show charge changes upon ionization. However, it illustrates the movements of the atoms due to the rearrangements from the positive (blue) areas to negative (yellow) ones.

In the experiment at time $t_1$, a superposition of photoelectrons stemming from $CuPc^0$ and $CuPc^+$ are obtained. Therefore we add the spectra in Fig. 5.5(C), assuming 45% of $CuPc^0$ and 55% of $CuPc^+$ in the system, to reproduce the experimental data. Due to the surface potential in the system upon charging, the calculated core spectra from $CuPc^0$ need to be shifted by 260 meV compared to Fig. 5.5(A). The structure of the calculated spectrum is similar to the ones obtained in the experiment shown in Fig. 5.5(F). However, the peaks stemming from the electrons in $C_N$ of $CuPc^0$ and $CuPc^+$ (left peaks) in the calculation are obtained at lower energy compared to the experimental data. This difference could also

be seen by comparison of the spectra from $CuPc^0$ in Fig. 5.5(A) to the experimental data in Fig. 5.5(E) and also other experimental results [170]. Therefore we apply an additional shift of 820 meV to the left peak of the spectra from $CuPc^0$ and $CuPc^+$. The calculated core photoelectron spectra with the applied shift are shown in Fig. 5.5(D), while black arrows mark this shift. We see that the left peak from the spectra of $CuPc^0$ now overlaps with the right one of $CuPc^+$, leading to an enhancement in the intensity similar to the one obtained in the experiment Fig. 5.5(F). The spectra are in great agreement, even though we do not calculate satellite peaks in the model.

Our calculated C1s core photoelectron spectra had to be shifted by three values to get an agreement with the experimental data. These shifts are necessary due to missing electronic correlation and the inaccurate description of the resulting binding energies. However, the calculation reveals important information about the system. We obtained that the binding energies of the carbon atoms shift in $CuPc^+$ compared to the ones from $CuPc^0$. Independent of the fitting parameters, we obtained that the gap between the left and right peaks, corresponding to photoelectrons from the $C_N$ and $C_B$ atoms, increases by 1 eV from $CuPc^+$ compared to the one from $CuPc^0$. This increase in the gap results from larger local changes of the charges at the $C_N$ atoms compared to the $C_B$ atoms upon ionization. Structural changes do not significantly influence this change in the molecule. The calculations revealed a ratio between the neutral and ionized CuPc at $t_1$ of 45:55. This ratio is also consistent with a decrease of the signal (approximately 30%) in the PMM related to the HOMO of CuPc at $t_{-1}$.

## 5.6. Structural changes in the photo-excited CuPc layer

The evaluation of the C1s core photoelectron spectra (Sec. 5.5) revealed that nearly half of the CuPc are ionized at $t_1 = 375$ fs after the excitation. Both the measured PMMs corresponding to the HOMO of CuPc and the carbon 1s tr-XPD patterns at the time $t_1 = 375$ fs after the excitation with the pump pulse demonstrate a rotation of the molecules relative to their geometry at $t_0 = 0$ fs [165]. The neutral charged $CuPc^0$ molecules rotate clockwise $(-15 \pm 3)^\circ$, while the ionized $CuPc^+$molecules rotate anti-clockwise $(15 \pm 3)^\circ$ within 375 fs after the excitation. By using a pair potential, we theoretically investigate the influence of the ionization of the molecules on the structure of the adsorbed molecular

layer. Motivated by the experimental results we focus on the rotation of the molecules. The approach of using a pair potential for studying the structural properties of adsorbed molecules is based on the work by Kröger et al. [190]. This pair potential model successfully described the geometry of several organic thin films on a substrate [190, 200, 201, 202, 203].

### 5.6.1. Pair potential

Consider two isolated molecules A and B. The pair potential between molecule A with atoms $i$ and the molecule B with atoms $j$ is

$$\phi_{AB} = \sum_{i,j} \left( \phi_{ij}^{vdW}(r_{ij}) + \phi_{ij}^{El}(r_{ij}) \right), \tag{5.24}$$

where $\phi_{ij}^{vdW}(r_{ij})$ is the van der Waals and $\phi_{ij}^{El}(r_{ij})$ the electrostatic potential, which both depend on the distance $r_{ij}$ between atom $i$ and $j$. The electrostatic potential depends on the partial charges $Z_i$ and $Z_j$ of the atoms $i$ and $j$

$$\phi_{ij}^{El}(r_{ij}) = \frac{Z_i Z_j}{r_{ij}}. \tag{5.25}$$

The RASCI calculations performed to obtain the electronic structure on isolated neutral $CuPc^0$ and ionized CuPc ($CuPc^+$) (Sec. 5.3) are constructed from a basis of atomic orbitals. Therefore we obtain from the results partial charges at each atom. The partial charges for $CuPc^0$ and $CuPc^+$ are in Tab. 5.2, while the corresponding atomic labels are shown in Fig. 5.7.

The van der Waals potential includes an exponential Pauli repulsion and an attractive London force written as

$$\phi_{ij}^{vdW}(r_{ij}) = a_{ij} \exp(-b_{ij} r_{ij}) - c_{ij} r_{ij}^{-6}, \tag{5.26}$$

where the coefficients $a_{ij}$, $b_{ij}$ and $c_{ij}$ depend on the specific element of the atoms $i$ and $j$. We use the parameters from [190].

### 5.6.2. Results and comparison

With the pair potential model, we investigate the structure of the molecules on the sample before and after the excitation. Before the sample is excited, the molecules on the substrate

| atom | $CuPc^0$ | $CuPc^+$ |
|---|---|---|
| C1 | +0.2293 | +0.2730 |
| C2 | +0.1246 | +0.1310 |
| C3 | −0.1906 | −0.1838 |
| C4 | −0.1471 | −0.1297 |
| H1 | +0.1611 | +0.1775 |
| H2 | +0.1437 | +0.1664 |
| N1 | −0.4289 | −0.4119 |
| N2 | −0.4350 | −0.4290 |
| Cu | +0.8873 | +0.8887 |

Table 5.2.: Partial charges (in the unit of the elementary charge $e$) at each atom for different states of CuPc. The atom label in the molecule is shown in Fig. 5.7.

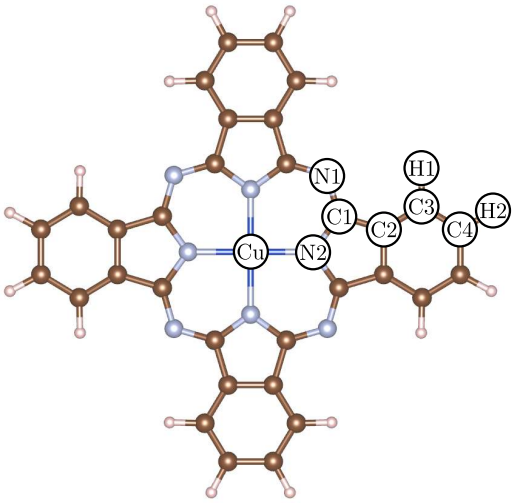


Figure 5.7.: Atomic structure of the CuPc molecule with the atomic labels used for the description of the partial charges in Tab. 5.2. For visualization of the molecule, we used the software VESTA [150]. Adapted from Ref. [165].

are neutral charged. This corresponds to the structure obtained in the experiment at the time $t_{-1} = -700$ fs, which we call the "unexcited structure". We model it with a two-dimensional grid of isolated $CuPc^0$ molecules. The LEED measurement of the sample in the ground state reveals that all molecules have the same orientation on the surface. This orientation means that all $CuPc^0_{t_{-1}}$ molecules (the subscript refers to the unexcited structure) have the same alignment on the substrate. The experimental PMM from the HOMO also indicates this alignment of the molecules. In our model, we fix the geometry of the atoms in each molecule. We obtain the orientation of the molecules by a minimum in the pair potential while sweeping over different angles $\alpha$ between the molecular axis and the vector which connects neighboring molecules. The sample structure used in the experiment for the time-resolved study was not explicitly checked with LEED. The intensity in the PMM from the HOMO suggests a coverage in the range of (0.8-1.0) ML. Since the distance between the molecules increases for lower coverage, we also change the distance between the molecules in the model. The structure used in the model is shown in Fig. 5.8A.

After the excitation of the sample, nearly half of the molecules are ionized. This corresponds to the structure obtained in the experiment at the time point $t_1$, which we call the "excited structure". We model it by a two-dimensional molecular grid in which every

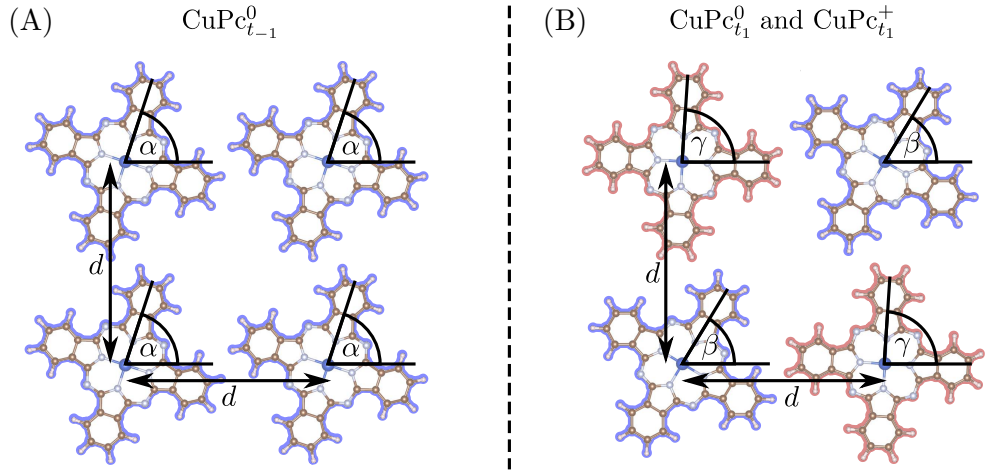


Figure 5.8.: Visualization of the two-dimensional grid of the molecules used in the pair potential calculation. The structure in (A) for the model of the unexcited structure contains only neutral charged molecules (blue). (B) structure for the model of the excited structure with neutral charged molecules (blue) and singly ionized ones (red) ordered in a checkerboard pattern. For visualization of the molecules, we used the software VESTA [150]. Adapted from Ref. [165].

$CuPc^0_{t_1}$ next neighbor is a $CuPc^+_{t_1}$ and vice versa (checkerboard pattern). We consider two different angles $\beta$ for the rotation of $CuPc^0$ and $\gamma$ for $CuPc^+$. The structure is shown in Fig. 5.8(B).

In both structures, we neglect the bending or shifting of the molecules to the surface and place them in one layer, justified by the results based on DFT of our collaborators. They obtained an atomic displacement perpendicular to the molecular plane for the hydrogen atoms closest to the surface of less than 0.2 Å. This displacement leads to a maximal change in the distance between the atoms $r_{ij}$ of 2%. For the carbon atoms closest to the surface, it is below 1%, and for all the other atoms even less.

We calculate the pair potential for different distances between the molecules on the grid and sweep through all possible molecular angles. For each distance between the molecules, we extract the angles which result in a minimum in the pair potential. We considered two different structure sizes. In the first one, we assume one molecule in the middle and calculate the potential by including the nearest neighbors. This structure contains five molecules. In the second structure, we also include the next-nearest and second next-

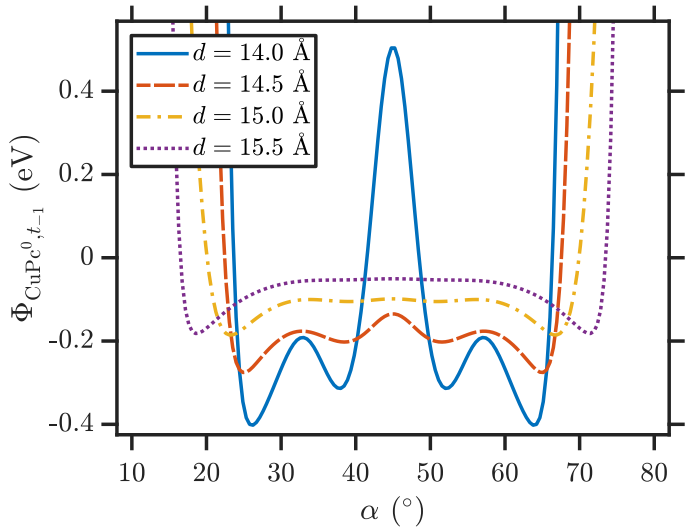


Figure 5.9.: Pair potential $\Phi_{\mathrm{CuPc}^0{}_{t_{-1}}}$ for the unexcited structure depending on the angle $\alpha$ and distance between next-neighbor molecules $d$. Adapted from Ref. [165].

nearest neighbors, resulting in a structure with 13 molecules. If not stated otherwise, the structure with five molecules is used. We also increased the structure beyond 13 molecules for some cases, but the results remained unchanged.

The pair potential for the unexcited structure at different angles $\alpha$ and distances $d$ is shown in Fig. 5.9. The angle $\alpha^*$ that minimizes the pair potential (we refer to it as the "optimal" angle) gives the initial orientation of the molecules on the substrate before the excitation. We see that it changes with the distance between the molecules. The lines in the plot are all symmetric around $\alpha = 45°$. This results from the symmetry of the molecules, the structures with $\alpha < 45°$ are the mirror image of the ones at $\alpha > 45°$.

In the model for the excited structure, the pair potential depends on the two angles $\beta$ and $\gamma$. The result for each distance between the molecules is shown as two-dimensional plots in Fig. 5.10. In this case, we now get a pair of optimal angles $(\beta^*, \gamma^*)$ for a minimum in the pair potential. The calculations show that the molecules change their structure upon excitation and rotate from their initial rotation angle $\alpha^*$ to a new rotation angle $\beta^*$ for the neutral molecules and $\gamma^*$ for the ionized molecules. We identify that this results from the interaction between ionized and neutral molecules. Interestingly, the neutral and charged molecules rotate in opposite directions. Further, the symmetry of the excited structure is

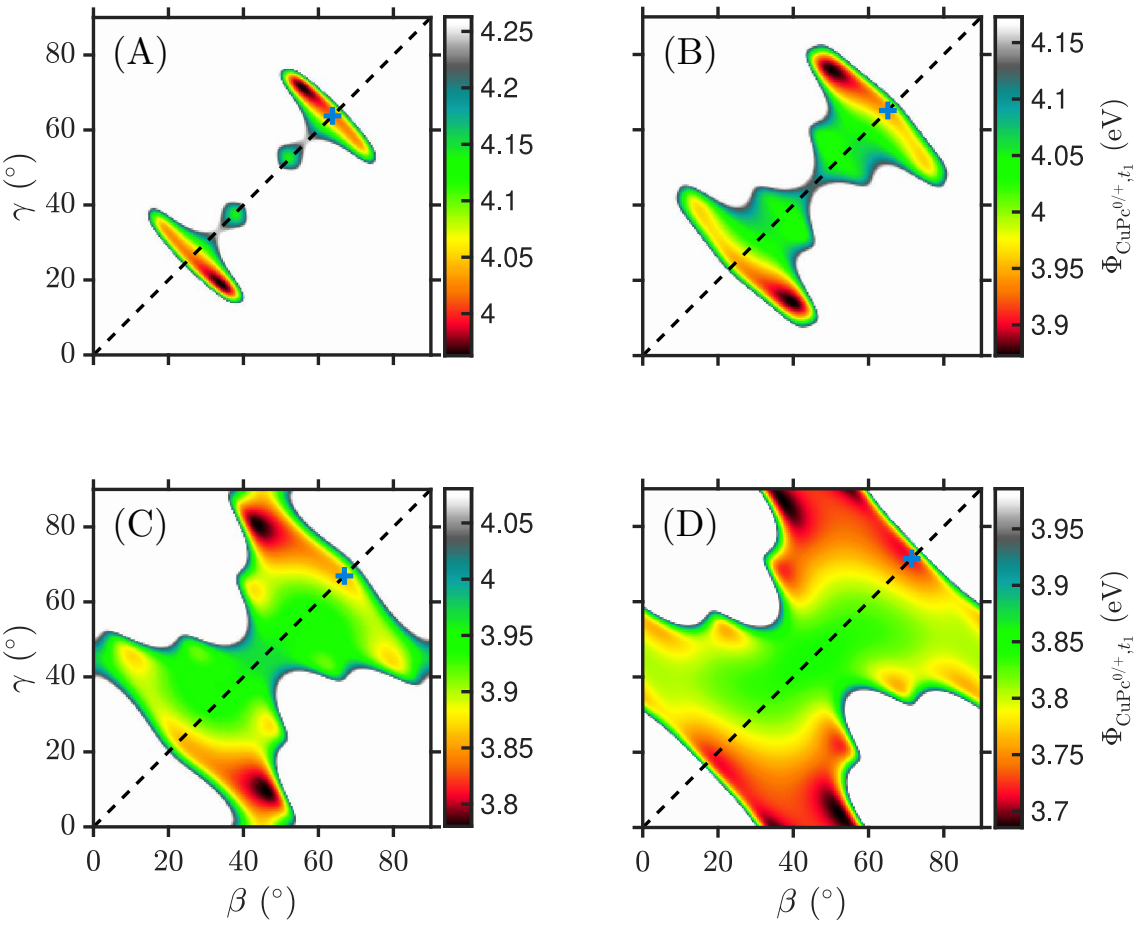


Figure 5.10.: Pair potential $\Phi_{CuPc^{0/+},t_1}$ for the excited structure depending on the angles $\beta$ and $\gamma$ describing the rotation of the neutral and ionized CuPc correspondingly. The pair potential is shown for different distances between the next-neighbor molecules with (A) $d = 14.0$ Å, (B) $d = 14.5$ Å, (C) $d = 15.0$ Å, and (D) $d = 15.5$ Å. The dashed black lines mark the diagonal of the plot, where $\beta = \gamma$. The blue cross in each plot marks the angle $\alpha^*$ for which the pair potential of the unexcited structure is minimized. Adapted from Ref. [165].

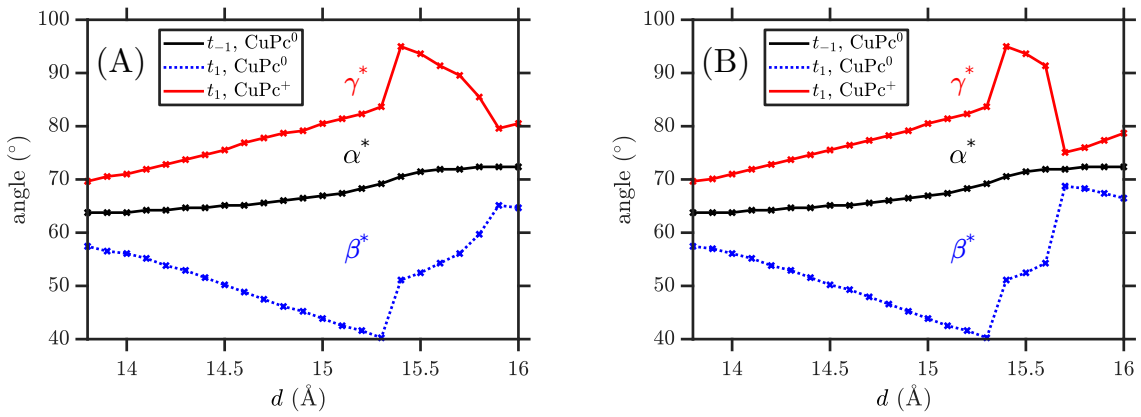


Figure 5.11.: Angles $\alpha^*$, $\beta^*$, $\gamma^*$ which minimize the pair potential in the unexcited and excited structure for different distances between neighboring molecules. The black line corresponds to the angles of the neutral charged molecules in the structure in Fig. 5.8(A). The blue and red lines show the angles for neutral charged and ionized CuPc in the structure in Fig. 5.8(B). (A) is obtained from a molecular grid that includes five molecules (one molecule in the middle and the nearest neighbors around). (B) is obtained from a structure that includes 13 molecules (one molecule in the middle, nearest and next-nearest neighbors around). Adapted from Ref. [165].

recovered in the two-dimensional plots in Fig. 5.10, since they are symmetric to a rotation of the image by 180°.

We look into the optimal angles for the unexcited and excited structures for different distances to further evaluate this structure change. Note that for each structure, two minima in the pair potential exist. For the unexcited structure, we choose the optimal angle $\alpha^* > 45°$. We choose the set of optimal angles for the excited structure, which are closer to angle $\alpha^*$. The results for the calculation involving five molecules are shown in Fig. 5.11(A). In the results for the unexcited system ($\mathrm{CuPc}^0_{t_{-1}}$, black line), we demonstrate that the angle increases with an increasing distance between the molecules from $\alpha = 63°$ to $\alpha = 73°$. The result does not depend on the size of the structure and we do not need to increase the structure beyond nearest-neighbor interactions. The model predicts that the molecules change their orientation after the excitation compared to the unexcited structure. The increasing angle of the ionized molecules corresponds to anti-clockwise

rotation to their new equilibrium geometry. The neutral molecules change their angle to a lower value and rotate clockwise until they reach the new equilibrium geometry. This rotation direction does not depend on the distance between the molecules, but the value of the rotation increases up to a distance of $d = 15.3$ Å. For $d > 15.3$ Å, the pair potential becomes flatter and other local minima appear. Therefore the optimal angles in the excited structure are not a continuous function anymore. The appearing different local minima and the flat pair potential at higher distances indicate that the interaction between the molecules loses its angle dependence.

As already mentioned, the calculation has two optimal angles caused by the symmetry of the system. One set of optimal angles $\alpha^*$,$\beta^*$ and $\gamma^*$ is shown in Fig. 5.11(A) and (B). The other angle in the unexcited structure is $\alpha' = 90 - \alpha^*$ and for the excited structure $\beta' = 90 - \beta^*$ and $\gamma' = 90 - \gamma^*$ (while all angles are in the range of $[0°, 90°]$). We refer to the second set of angles as the mirror domain since the structure is the mirror image of the other one. This means if the molecules in the unexcited structure have an initial angle above 45°, the ionized molecules, after the excitation, start to rotate anti-clockwise, and the neutral ones clockwise to the new equilibrium geometry of the structure. In the mirror domain, the rotations of the molecules from the structure before and after excitation are vice versa. The ionized molecules rotate clockwise, while the neutral molecules rotate anti-clockwise.

For the calculation in Fig. 5.11(B), we extended the structure by including the next-nearest neighbors, including 13 molecules in the grid. The results remain unchanged up to a distance of $d = 15.6$ Å compared to Fig. 5.11(A). For larger distances between the molecules, the absolute value of the rotation slightly changes for the different grid sizes. This results from the pair potential becoming flatter around the minimum at larger distances between the molecules. Therefore, the small changes due to the next-nearest neighbor interactions lead to a slight shift of the minimum. For smaller distances, the next-nearest neighboring molecules do not affect the position of the minimum in the potential since it is stronger pronounced. However, the relevant property is the rotation of the molecules, which remains in the same direction even if we increase the grid size further.

In Appendix A.2, the details for our approach to calculating the pair potential, including the influence of the substrate, are presented. The results show no significant change com-

pared to Fig. 5.10, except for a constant shift in the pair potential. The rotation of the molecules is therefore not influenced by the negative charge of the substrate.

The positive charges in the molecular layer lead to a repulsive force between the molecules (shown by a decreasing potential for increasing distances in Fig. 5.10). This repulsive force can cause changes in the distances between the molecules in the excited structure. As shown in Fig. A.1, the interaction with the substrate counteracts the repulsive force between the molecules (increasing potential for higher distances) and makes the structure stable. Therefore, the influence of the substrate is relevant for describing molecular shifts along the surface after the excitation. Due to the limitations of our model (an accurate description of the complete substrate, bending of the molecules) and since the experimental data is not sensitive to such shifts of the molecules, we have not investigated the changes in the distances between the molecules further. However, the results in Fig. 5.11 demonstrate that only the magnitude of the rotation, but not the direction, depends on the distance between the molecules and our conclusion is still valid.

With the pair potential calculation, we identified that the molecules rotate after the excitation caused by the interaction between the charged and non-charged molecules. The experimental tr-PMMs of the HOMO and tr-XPD data also provides such a rotation. After the excitation, the neutral molecules $CuPc^0_{t_1}$ rotate clockwise by an angle of $(-15 \pm 3)^\circ$ and the ionized $CuPc^+_{t_1}$ anti clockwise by an angle of $(15 \pm 3)^\circ$. The experimental data do not show an opposite rotation of the molecules ($CuPc^0_{t_1}$ anti-clockwise, $CuPc^+_{t_1}$ clockwise), which would be the case in the mirror domain. Therefore we conclude that no mirror domain exists in the sample. The interplay between the four-fold symmetry of the molecules and the three-fold symmetry of the substrate can slightly disturb this symmetry [204, 205]. This leads to a reorganization of the molecules over the time of the measurement. The amount of molecules in the mirror domain is then suppressed and so-called homochiral domains [206, 207, 208] are present in the sample.

## 5.7. Summary

In summary, my calculations on CuPc provide insights into the measured values of tr-ARPES, tr-XPD, and tr-XPS. We revealed that combining all the experimental methods and the-

oretical calculations is a powerful method to image the response of the system (electronic and structural) up to several hundreds of femtoseconds.

The excitation of the sample lead to an occupation of orbitals in CuPc above the HOMO. With my calculations, we could reveal a symmetry breaking of the excited state in the molecule, most probably related to the interaction with the substrate. This symmetry breaking indicates that the occupation of the excited state in CuPc occurs due to charge transfer from the photoexcited Ti 3d states in the substrate.

After the de-occupation of the excited state in CuPc, the charge is redistributed in the system in comparison to the ground state. Comparing my simulations of the C1s core photoelectron spectra to the experimental data revealed that 375 fs after the excitation with the pump pulse, approximately 55% of the molecules in the sample are ionized. Further, we obtain a change in the binding energies of the C1s core electrons in $CuPc^+$, which have different strengths for different carbon atoms in CuPc.

With the pair potential model, we could explain the experimentally observed rotation of the molecules after the excitation of the system. We see that the direction of the rotation in the molecules is linked to the initial orientation of the molecules. Our calculations show that the symmetry between the mirror domains in the structure must be broken, and homochiral domains must be formed.

# 6. Imaging charge migration with time- and momentum-resolved photoelectron spectroscopy

This chapter presents the results published in [209]. Here, I theoretically study the possibilities of time-resolved photoelectron microscopy for imaging excited electronic charge oscillations down to the attosecond timescale. In particular, I consider charge migration in pentacene described by a superposition of excited states. The interaction with the broadband probe pulse removes the bound electrons. I did this work under the supervision of Daria Gorelova.

## 6.1. Charge migration

The interaction of attosecond light pulses with molecules could lead to the population of several excited states, creating a coherent electronic wave packet. This launched electronic wave packet leads to an oscillation of the charges in the molecule on the attosecond timescale. If it is purely electronic, without the influence of the nuclei, this process is called charge migration [120]. Charge migration happens up to a few femtoseconds and can be the first step in charge transfer [210]. The interaction with the nuclei destroys the electronic coherence leading to the redistribution of the charges in the molecule [210]. The relation of electronic coherence to charge transfer makes this topic important for solar cells [211], e.g., in the process of efficient charge transfer [212, 213].

Charge migration is a coherent motion of electron density that is launched, when a wavefunction becomes a coherent superposition of electronic eigenstates. Until now, charge migration has been investigated in ionized molecules [120, 214, 215, 216, 217] and also

in neutral molecules where it results from excited electronic states [121, 218, 219, 220]. For more details on charge migration, we refer to the reviews [210, 221, 222]. Experimentally, charge migration in ionized molecules has been observed, e.g., in phenylalanine [18], iodoacetylene [31], and tryptophan [223]. Coherent electron dynamics can also be created by crossing a conical interaction [224]. Conical interactions appear where two adiabatic PESs get close and cross. Conical interactions are important for charge transfer processes in OSCs [225, 226].

Charge migration describes purely electronic charge oscillation without considering the effects of the nuclei. Pure charge migration will continue forever without considering coupling to the environment/nuclei. Including the nuclei in the model leads to decoherence, causing the amplitude of the charge oscillations to decay [210, 227, 228]. However, studies on norbornadiene cations [229] and benzene [230], molecules similar to the one considered here, have shown coherence of the electronic motions up to 20 fs.

Since imaging ultrafast electronic dynamics is challenging, new experiments have been theoretically proposed [44, 45, 231, 232, 233, 234, 235, 236, 237, 238]. Here we want to show how photoelectron momentum microscopy can observe charge migration in an excited neutral molecule with angstrom spatial resolution. In particular, we consider a coherent superposition of the excited states in pentacene probed with an XUV probe pulse. We analyze how spatial and time properties of coherent electron dynamics are encoded in the photoelectron momentum distribution. Imaging charge migration in ionized molecules has already been theoretically considered [86]. Here we extend this work to charge migration in excited molecules. In Sec. 4.1, the relevance of pentacene for OSCs is described.

## 6.2. Computational details

We consider charge migration initiated by a pump pulse, which creates a coherent superposition of excited states at time $t_0$ in the electronic system. The time evolution of this wave packet is

$$|\Psi(t)\rangle = \sum_j C_j e^{-iE_j(t-t_0)} |\Phi_j\rangle \,, \tag{6.1}$$

where $|\Phi_j\rangle$ is the electronic excited eigenstate $j$ of the system with the corresponding energy $E_j$. The coefficients $C_j$ are the population distribution for each state $j$ and are

determined by the characteristics of the pump pulse.

### 6.2.1. Photoelectron momentum distribution

The system is probed with an ultrashort XUV pulse at time $t_p$, which leads to an emission of photoelectrons. The momentum distribution of the photoelectron encodes information about the electronic state at the time $t_p$. The derivation of the time and momentum-depended photoelectron probability is in Sec. 3.1 and is based on the work in [86]. According to Eq. (3.25), where a probe pulse with center photon energy $\omega_{in}$, polarization $\boldsymbol{\epsilon}_{in}$, pulse duration $\tau_p$ and intensity profile $I(t) = I_0 e^{-4\ln 2[(t-t_p)/\tau_p]^2}$ has been assumed, the photoelectron probability is

$$P(\mathbf{q}, t_p) = \frac{\pi^2 \tau_p^2 I_0 \left|\boldsymbol{\epsilon}_{in} \cdot \mathbf{q}\right|^2}{\ln 2 \omega_{in}^2 c} \sum_{F,\sigma} \left| \sum_j \nu_{j,F}(t_p) \int d^3r \; \phi_e^\dagger(\mathbf{r}, \mathbf{q}) \left\langle \Phi_F \right| \hat{\psi}(\mathbf{r}) \left| \Phi_j \right\rangle \right|^2 , \tag{6.2}$$

$$\nu_{j,F}(t_p) = e^{-\frac{\tau_p^2}{8\ln 2}(E_F - E_j - \omega_{in} + \epsilon_e)^2} C_j e^{-iE_j(t_p - t_0)}, \tag{6.3}$$

where $\mathbf{q}$ is the momentum of the photoelectron with the corresponding energy $\epsilon_e = \frac{|\mathbf{q}|^2}{2}$, $\phi_e^\dagger(\mathbf{r}, \mathbf{q})$ is the wavefunction of the photoelectron, $\hat{\psi}(\mathbf{r})$ is the electron annihilation field operator and $\langle \Phi_F|$ is the final state after the ionization with the probe pulse with the corresponding energy $E_F$.

For the description of the photoelectron wavefunction within the PWA we use Eq. (3.28)

$$\phi_e(\mathbf{r}, \mathbf{q}) = \frac{1}{\sqrt{(2\pi)^3}} e^{i\mathbf{q}\mathbf{r}} \chi_\sigma, \tag{6.4}$$

where $\chi_\sigma$ is the wavefunction of the photoelectron spin state.

The crucial part of the calculation in Eq. (6.2) is the overlap between the final state and the excited state in the wave packet of the initial state $\langle \Phi_F| \hat{\psi}(\mathbf{r}) |\Phi_j\rangle$ (Dyson orbital). We describe each excited state based on CI up to single excitation

$$|\Phi_j\rangle = \sum_{i_1, a_1} \tilde{c}_{i_1}^{a_1}(j) \left| \phi_{i_1}^{a_1, S(j)} \right\rangle , \tag{6.5}$$

where $\left|\phi_{i_1}^{a_1,S(j)}\right\rangle$ denotes a CSF, where an electron of the HF ground-state has been excited from the orbital $i_1$ to the orbital $a_1$. Such a state has a hole in orbital $i_1$ and an electron in orbital $a_1$, and $S(j)$ describes the total spin and the spin projection value. We describe

the final state similarly, with one additional hole in the configuration space

$$\langle \Phi_F | = \sum_{i_2,j_2,a_2} \tilde{c}^{a_2}_{i_2,j_2}(F) \left\langle \phi^{a_2,S(F)}_{i_2,j_2} \right| + \sum_{i_2} \tilde{c}_{i_2}(F) \left\langle \phi^{S(F)}_{i_2} \right| , \tag{6.6}$$

where $\left\langle \phi^{a_2,S(F)}_{i_2,j_2} \right|$ describes a CSF which contains two holes in orbital $i_2$ and $j_2$ and an electron in orbital $a_2$. We denote a CSF with one hole and no excited electron with $\left\langle \phi^{S(F)}_{i_2} \right|$. In both cases, $S(F)$ describes the total spin and the spin projection value of the final state $F$. The coefficients $\tilde{c}^{a_2}_{i_2,j_2}(F)$ and $\tilde{c}_{i_2}(F)$ determine the contribution of a CSF to the final state. The evaluation of the Dyson orbital $\langle \Phi_F | \hat{\psi}(\mathbf{r}) | \Phi_j \rangle$ for such an initial and final state is shown in detail in Sec. 3.2.

### 6.2.2. Excited states of the molecules

To evaluate the wave packet in Eq. (6.1), we need to know the excited states of the molecule. For the selection of the molecules, we calculate the first few excited states and the transition probability from the ground state. We consider the molecules pentacene, anthracene, naphthalene, carbonyl sulfide (OCS), propylene oxide, and Dithieno$[3,2-\mathrm{b}:2',3'-\mathrm{d}]$thiophen.

The excited states are calculated with a RASCI calculation, with a maximum number of one hole in the RAS1 space and a maximum number of one electron in the RAS3 space. The RAS2 space is empty. For the calculation of the excited states, the amount of orbitals in the RAS1 and RAS3 space is chosen that further increase does not change the results (converged). The direct transition with the pump pulse from the ground state to triplet excited states is dipole-forbidden (dark states). Therefore we truncate our considerations to spin-singlet excited states. We calculate the vertical excited spin-singlet states of each molecule with MOLCAS [116] with a cc-pVDZ basis set for the atoms [146, 147].

To consider the lowest amount of excited states in the wave packet, we are looking for a molecule with two low-lying excited states, which are dipole-allowed (bright states) for excitation from the ground state and separated from other dipole-allowed states. In such a case, the pump pulse could be chosen so that it launches a coherent superposition of the lowest two excited states at $t_0$

$$|\Psi(t)\rangle = C_1 e^{-iE_1(t-t_0)} |\Phi_1\rangle + C_2 e^{-iE_2(t-t_0)} |\Phi_2\rangle . \tag{6.7}$$

The oscillation period of this wave packet is determined by the energy difference between the states $T = 2\pi/(E_2 - E_1)$. We want to image a full oscillation period of the charge dynamics. Therefore the oscillation period should be long enough to visualize it with the available temporal resolution and short enough before decoherence destroys them. Therefore the oscillation periods of the wave packet should approximately be in the range of 5 fs $< T <$ 15 fs.

We determined that propylene oxide and Dithieno$[3, 2-b : 2', 3'-d]$thiophen are unsuitable for our requirements because the two lowest-lying bright states are not separated (more than 1 eV) from the others. Anthracene and naphthalene fulfill this, but the oscillation period of the wave packets is above 20 fs. We obtain two low-lying degenerate excited states for OCS, but the oscillation period for a wave packet involving the lowest three states is too fast $T < 2$ fs. The best of the six molecules for our needs is pentacene, which we already studied in Ch. 4. Calculating the first excited states of pentacene involves an active space of 22 orbitals, containing $11\pi$ and $11\pi^*$ orbitals. According to the excited-state spectrum in Fig. 6.1, the first two excited-states are separated from the next bright excited-states, which are in energy above $S_4$. Therefore, one could create a coherent superposition of the excited-state $S_1$ and $S_2$ in a possible experiment. Due to the energy difference between the two states, the wave packet has an oscillation period of $T = 5.73$ fs. We can neglect nuclear motions for simplicity on such timescales.

## 6.3. Imaging charge migration in pentacene

Based on the previous considerations, we present an example of imaging excited-state dynamics in aligned isolated pentacene molecules. Experimentally the alignment of the molecules could be achieve in the gas phase, or as our results of Ch. 4 indicate, isolated molecular dynamics can also be obtained for molecular thin films on a substrate [62]. The important properties for the aim of our study are the relative energies between the first two bright excited states, defining the oscillation period, and the orbital excitations in CI that contribute to the wavefunction. These calculated values, as shown in Fig. 6.1, agree with the experimental and theoretical data in previous studies [239, 240, 241].

Fig. 6.1 shows that the first excited states of pentacene are described by a CSF, where an

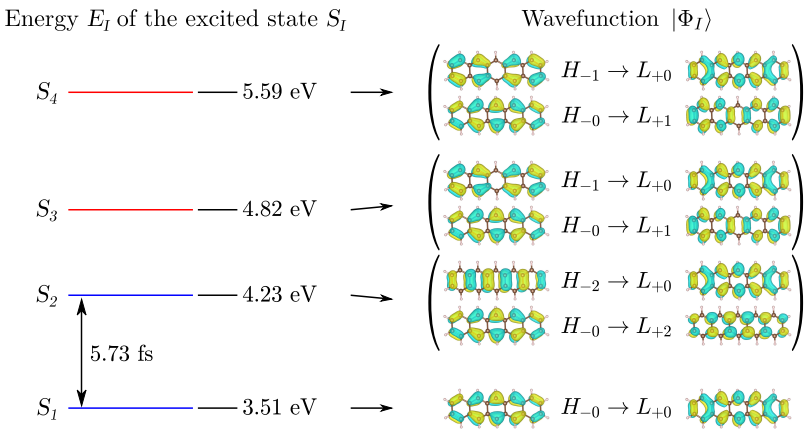


Figure 6.1.: Energy-level diagram of the first four vertical spin-singlet excited states of pentacene (left), with bright states in blue and dark states in red. A wave packet in a coherent superposition of the first two excited states has an oscillation period of 5.73 fs. The corresponding orbital excitations in the wavefunction of the states are shown on the right, while the arrow in the brackets means an excitation from the left (HOMO-i) to the right (LUMO+j) orbital. For the visualization of the orbitals, we used the software VESTA [150]. Adapted from Ref. [209].

electron from the HOMO has been excited into the LUMO

$$|\Phi_1\rangle = \left|\phi_H^{L,0(0)}\right\rangle, \tag{6.8}$$

where the CSF $\left|\phi_{H-i}^{L+j,0(0)}\right\rangle$ is given by an excitation of the orbital $H-i$ (ith orbital below the HOMO) to the orbital $L+j$ (jth orbital above the LUMO). The second excited state is a linear combination of two CSF. In the first CSF, an electron from the HOMO has been excited into the LUMO+2, and in the second CSF, an electron from the HOMO-2 has been excited into the LUMO

$$|\Phi_2\rangle = \frac{1}{\sqrt{2}}\left(\left|\phi_H^{L+2,0(0)}\right\rangle - \left|\phi_{H-2}^{L,0(0)}\right\rangle\right). \tag{6.9}$$

The time evolution of the wave packet after the excitation with the pump pulse is given by Eq. (6.7). We assume an equal population of both states $C_1 = C_2$ (given in Eq. (6.7)).

The excitation with the pump pulse changes the electron density in the molecule (electron-hole density). This electron-hole density is given by the difference between the electron density of pentacene after and before the pump pulse

$$\rho_{ex}(t) = \rho(\Psi(t)) - \rho(\Phi_0), \tag{6.10}$$

where $\rho(\Phi_0) = \langle\Phi_0|\,\hat{\psi}^\dagger(\mathbf{r})\hat{\psi}(\mathbf{r})\,|\Phi_0\rangle$ is the electron density of the HF ground-state of pentacene described by the wavefunction $|\Phi_0\rangle$, and $\rho(\Psi(t)) = \langle(\Psi(t)|\,\hat{\psi}^\dagger(\mathbf{r})\hat{\psi}(\mathbf{r})\,|(\Psi(t)\rangle$ is the electron density for the pentacene after the excitation with the pump pulse. The evaluation of this electron-hole density for a coherent superposition of excited states, described with CIS, is shown in detail in Sec. 3.3. For the considered wave packet in pentacene, the electron-hole density is

$$\begin{aligned}\rho_{ex}(\mathbf{r},t) = &\left|C_1^* e^{iE_1 t}\phi_L(\mathbf{r}) + \frac{C_2^*}{\sqrt{2}}e^{iE_2 t}\phi_{L+2}(\mathbf{r})\right|^2 + \frac{|C_2|^2}{2}|\phi_L(\mathbf{r})|^2 \\ &- \left|C_1^* e^{iE_1 t}\phi_H(\mathbf{r}) - \frac{C_2^*}{\sqrt{2}}e^{iE_2 t}\phi_{H-2}(\mathbf{r})\right|^2 - \frac{|C_2|^2}{2}|\phi_H(\mathbf{r})|^2,,\end{aligned} \tag{6.11}$$

where $\phi_i(\mathbf{r})$ is the wavefunction of the MO $i$. The LUMO and higher orbitals positively contribute to the electron density change, while the HOMO and lower orbitals have a negative contribution. We can separate the electron-hole density into a time-dependent

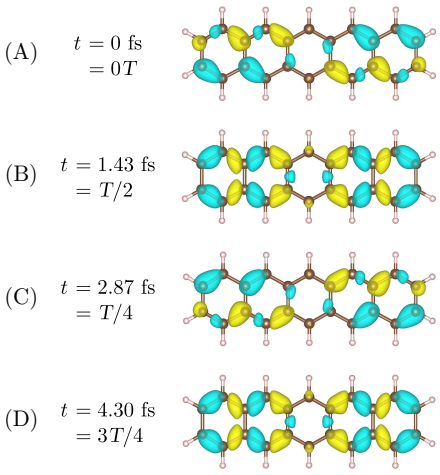


Figure 6.2.: The time evolution of the electron-hole density (A) 0 fs, (B) 1.43 fs, (C) 2.87 fs and (D) 4.30 fs after the excitation of the pentacene molecule to the first two excited states with the pump pulse. The blue isosurface shows the hole density (negative value), and the yellow shows the electron density (positive value). We used the software VESTA [150] for the visualization. Adapted from Ref. [209].

part

$$\rho_{ex,1}(t) = 2\mathrm{Re}\left[\tilde{\phi}(\mathbf{r})\right]\cos\left[(E_1 - E_2)(t - t_0)\right] - 2\mathrm{Im}\left[\tilde{\phi}(\mathbf{r})\right]\sin\left[(E_1 - E_2)(t - t_0)\right], \quad (6.12)$$

$$\text{with } \tilde{\phi}(\mathbf{r}) = \frac{C_1^* C_2}{\sqrt{2}}\left(\phi_L^*(\mathbf{r})\phi_{L+2}(\mathbf{r}) + \phi_H^*(\mathbf{r})\phi_{H-2}(\mathbf{r})\right), \quad (6.13)$$

and a time-independent part

$$\rho_{ex,2} = \left(|C_1|^2 + \frac{|C_2|^2}{2}\right)\left(-|\phi_H(\mathbf{r})|^2 + |\phi_L(\mathbf{r})|^2\right) + \frac{|C_2|^2}{2}\left(-|\phi_{H-2}(\mathbf{r})|^2 + |\phi_{L+2}(\mathbf{r})|^2\right). \quad (6.14)$$

The electron-hole density is shown in Fig. 6.2. The negative (blue) part is the hole density, meaning a reduction of the electron density compared to the ground state. The positive one (yellow) shows an increase in the electron density. We see that the excitation with the pump pulse rearranges the charges in the molecule, which oscillates over time. In our calculation, $\mathrm{Im}\left[\tilde{\phi}(\mathbf{r})\right] = 0$, and according to Eq. (6.12), the time-dependent part in the electron-hole density is proportional to $\cos\left[(E_1 - E_2)(t - t_0)\right]$, which we also see in Fig. 6.2. From $t = 0T$ to $t = \frac{T}{2}$ (Fig. 6.2(A) and (C)), the photoinduced negative charge

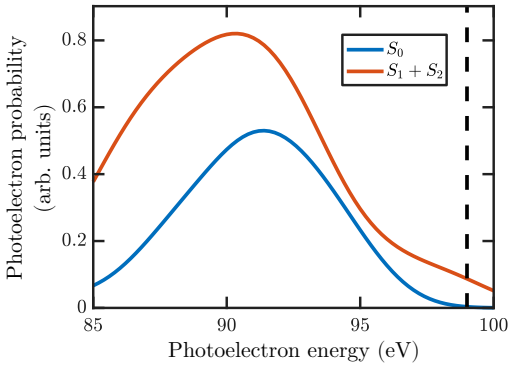


Figure 6.3.: Angle-integrated photoelectron spectra for photoelectrons detached from the ground-state $S_0$ or in the coherent superposition of the excited-states $S_1$ and $S_2$. The black dashed line shows the contribution at the photoelectron energy $\epsilon_e = 99$ eV. The probe pulse duration is $\tau_p = 0.5$ fs and has a center photon energy of $\omega_{in} = 100$ eV. Adapted from Ref. [209].

seems to flow from the top left and bottom right of the molecule to the top right and bottom left, and for the positive charge vice versa. The spatial distribution of the electron density change at $t = \frac{T}{2}$ is connected to the one at $t = 0T$ by a reflection along the plane perpendicular to the short axis of the molecule. At $t = \frac{T}{4}$ and $t = \frac{3T}{4}$ (Fig. 6.2(B) and (D)) the pump-induced change in the electron density is equal.

Tab. 6.1 shows the first six final states of pentacene that can be reached by ionizing the initial state in Eq. (6.7). Due to the exponential factor in Eq. (6.3), the photoelectron probability for a specific transition of an initial to a final state is energetically distributed around a centering value. The center of the Gaussian curve is $\Omega_{F,j} = E_F - E_j - \omega_{in} + \epsilon_e$ and the width is determined by the probe pulse duration. We assume a probe pulse with a center photon energy of $\omega_{in} = 100$ eV and pulse duration $\tau_p = 0.5$ fs, resulting in a full width at half maximum of the Gaussian curve of 5.16 eV. We first consider the angle-integrated spectra. A probe pulse energy of 100 eV corresponds to a de Broglie wavelength of approximately 1 Å, allowing angstrom spatial resolution. In principle, the interaction with the probe pulse creates photoelectrons from the pentacene molecules in the ground and excited state. Consequently, we consider two initial states, the pentacene molecule in the ground-state $S_0$ and in the coherent superposition of the excited-state $S_1$ and $S_2$ ($|\Psi(t)\rangle$

| F | $E_F$ | $\Omega_{F,1ES}$ | $\Omega_{F,2ES}$ | $\langle\Phi_F\vert$ |
|---|---|---|---|---|
| 1 | 5.0 eV | 98.5 eV | 99.2 eV | $-0.95\left\langle\Phi_H^{1/2(1/2)}\right\vert$ |
| 2 | 6.7 eV | - | 97.5 eV | $-0.94\left\langle\Phi_{H-2}^{1/2(1/2)}\right\vert$ |
| 3 | 7.5 eV | 96.0 eV | - | $-0.83\left\langle\Phi_{H,H}^{L,1/2(1/2)}\right\vert + 0.31\left\langle\Phi_{H-4}^{1/2(1/2)}\right\vert$ |
| 4 | 8.7 eV | 94.8 eV | - | $-0.62\left\langle\Phi_{H,H}^{L+1,1/2(1/2)}\right\vert + 0.5\left\langle\Phi_{H-1,H}^{L,1/2(1/2)}\right\vert_{udu}$ $+0.28\left\langle\Phi_{H-1,H}^{L,1/2(1/2)}\right\vert_{uud}$ |
| 5 | 9.6 eV | 93.9 eV | - | $0.70\left\langle\Phi_{H-1,H}^{L,1/2(1/2)}\right\vert_{uud} - 0.45\left\langle\Phi_{H-1,H}^{L,1/2(1/2)}\right\vert_{udu}$ |
| 6 | 9.7 eV | - | 94.5 eV | $-0.59\left\langle\Phi_{H,H}^{L+2,1/2(1/2)}\right\vert + 0.62\left\langle\Phi_{H-2,H}^{L,1/2(1/2)}\right\vert_{udu}$ $-0.28\left\langle\Phi_{H-2,H}^{L,1/2(1/2)}\right\vert_{uud}$ |

Table 6.1.: First six final states $\langle\Phi_F\vert$ of ionized and excited pentacene, which have a nonzero overlap with the initial state $\langle\Phi_F\vert\,\hat{\psi}(\mathbf{r})\,\vert\Phi_j\rangle$. The corresponding energy is $E_F$, and $\Omega_{F,1ES}/\Omega_{F,2ES} = E_F - E_{1ES/2ES} - \omega_{in} + \epsilon_e$ is the center of the photoelectron probability in energy in Eq. (6.2) for the given final state where we distinguish between photoelectrons which have been detached from the first/second excited-state (1ES/2ES) of pentacene. If the value for $\Omega_{F,1ES}/\Omega_{F,2ES}$ is empty, the overlap with the initial state is zero. The right column shows the contributing CSFs of the final state. For the coupling of three electrons, two different CSFs result in the same total and spin-projection value. We denote those here with *uud* and *udu*.

in Eq. (6.7)). Fig. 6.3 shows the angle-integrated spectra. Interestingly the photoelectron distribution for electrons emitted from the initial-state $|\Psi(t)\rangle$ is time-independent. This time-independence results from the high symmetry of the electron-hole density. We see that the signal strongly depends on the chosen photoelectron energy. A ground-state free measurement of photoelectron stemming from the excited state is possible at photoelectron energies of $\epsilon_e = 99$ eV (marked by the dashed line in Fig. 6.3) and higher. The signal for photoelectrons emitted from transitions to different final states overlaps due to the broad distribution in energy. This broadening makes it impossible to distinguish which signal belongs to which final state transitions only from the photoelectron distribution curve.

The angle-integrated spectra do not reveal information about the time-dependent electron-hole density and do not resolve transitions to different final states. We now want to investigate if photoelectron microscopy can overcome these issues. We first look into the PMMs at a particular energy, and afterward, demonstrate the dependence on the photoelectron energy. PMMs are constructed by a two-dimensional projection of the three-dimensional photoelectron momentum distribution for constant energy $\epsilon_e$ (hemispherical cuts). Based on Eq. (6.2), the photoelectron probability resulting from a particular final state is only time-dependent if the final state has a nonzero overlap with both states in the initial state, $\langle\Phi_F|\,\hat{\psi}(\mathbf{r})\,|\Phi_1\rangle \neq 0$ and $\langle\Phi_F|\,\hat{\psi}(\mathbf{r})\,|\Phi_2\rangle \neq 0$. In the case of the first six relevant final states (Tab. 6.1), only the contribution from the first one gives a time-dependent photoelectron distribution, which is centered at an energy of 98.5 eV and 99.2 eV of the emitted photoelectrons. We choose the photoelectron energy $\epsilon_e = 99$ eV to image this time-dependent feature. At $\epsilon_e = 99$ eV the contribution of photoelectrons emitted from the ground-state is almost zero (see black dashed line in Fig. 6.3), and we neglect the ground-state. Because of the broadening in energy, we take all final states into account, where $\Omega_{F,1ES/2ES} = E_F - E_{1ES/2ES} - \omega_{in} + \epsilon_e$ is roughly in the range of $(96 - 102)$ eV covering the range of the first three excited-states. For the first three final states, the Dyson orbital is

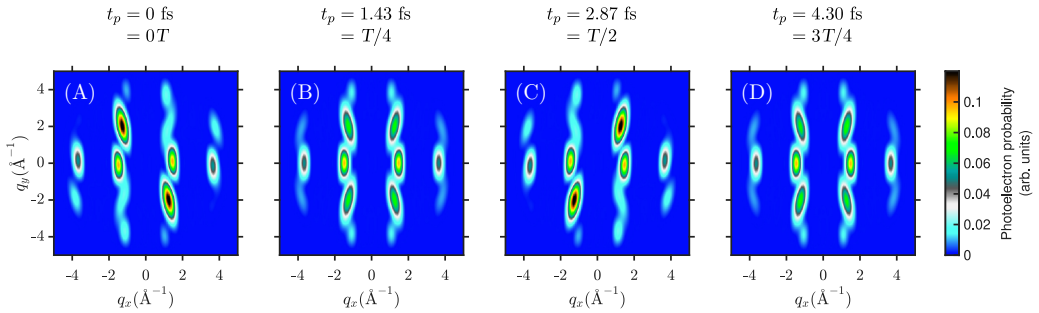


Figure 6.4.: The time evolution of the PMMs where the probe pulse detaches the photoelectron at time (A) $t_p = 0$ fs, (B) $t_p = 1.43$ fs, (C) $t_p = 2.87$ fs and (D) $t_p = 4.30$ fs from the excited pentacene. The probe pulse duration is $\tau_p = 0.5$ fs and has a center photon energy of $\omega_{in} = 100$ eV. The momentum maps are shown for the photoelectron energy of $\epsilon_e = 99$ eV. Adapted from Ref. [209].

$$\langle \Phi_{F_1} | \hat{\psi}(\mathbf{r}) | \Phi_1 \rangle = -\frac{0.95}{\sqrt{2}} \phi_L(\mathbf{r}) \chi_\downarrow, \tag{6.15}$$

$$\langle \Phi_{F_1} | \hat{\psi}(\mathbf{r}) | \Phi_2 \rangle = -\frac{0.95}{2} \phi_{L+2}(\mathbf{r}) \chi_\downarrow, \tag{6.16}$$

$$\langle \Phi_{F_2} | \hat{\psi}(\mathbf{r}) | \Phi_2 \rangle = \frac{0.94}{2} \phi_L(\mathbf{r}) \chi_\downarrow, \tag{6.17}$$

$$\langle \Phi_{F_3} | \hat{\psi}(\mathbf{r}) | \Phi_1 \rangle = -\frac{0.83}{\sqrt{2}} \phi_H(\mathbf{r}) \chi_\downarrow. \tag{6.18}$$

These four Dyson orbitals contain the LUMO+2, LUMO, and HOMO wavefunction. Besides the contribution from the HOMO, the photoelectrons emitted at $\epsilon_e = 99$ eV can be interpreted as the electrons photoexcited by the pump pulse. Therefore these electrons have less binding energy than the ones from the ground state. The resulting time-resolved PMMs are shown in Fig. 6.4. The PMMs at $t_p = 0T$ and $t_p = \frac{T}{2}$ (Fig. 6.4(A) and (C)) are the reflection image (along the axis $q_x = 0$ Å$^{-1}$) of the other one and have the same symmetry as the electron-hole density at these times. The other PMMs at $t_p = \frac{T}{4}$ and $t_p = \frac{3T}{4}$ (Fig. 6.4(B) and (D)) are equal. According to the Dyson orbitals in Eq. (6.15) and Eq. (6.16), the time-dependent feature in the PMMs arises from the Fourier transformed wavefunction of LUMO+2 and LUMO. The other Dyson orbitals in Eq. (6.17) and Eq. (6.18) contribute as time-constant features in the PMMs. The time-resolved signal at the photoelectron energy of $\epsilon_e = 99$ eV thus stems from the absolute square of the Fourier

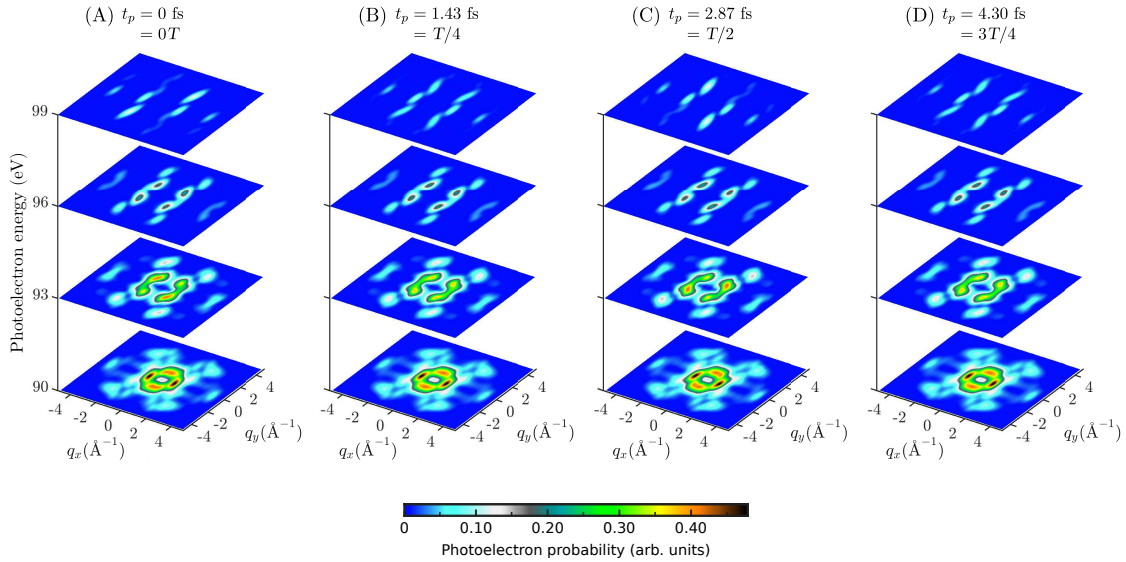


Figure 6.5.: Time evolution of the PMMs for different photoelectron energies $\epsilon_e$. Each set of momentum maps has different probe pulse arrival times (A) $t_p = 0$ fs, (B) $t_p = 1.43$ fs, (C) $t_p = 2.87$ fs and (D) $t_p = 4.30$ fs. The probe pulse duration is $\tau_p = 0.5$ fs and has a center photon energy of $\omega_{in} = 100$ eV. Adapted from Ref. [209].

transformed LUMO+2 and LUMO wavefunction. It is directly related to the negative part of the time-dependent electron density change in Fig. 6.2. We see that the PMMs encode information about the excited-state dynamics. A possible experiment could use the high contrast and small background features to obtain information from the system even for a weak signal.

Now we investigate the dependence of PMMs on the photoelectron energy. The PMMs for different energies are shown in Fig. 6.5. Similar to the angle-integrated spectra, the overall intensity increases for lower photoelectron energies. The time-dependence of the signal in the PMMs at $\epsilon_e = 90$ eV and $\epsilon_e = 96$ eV is weak. At $\epsilon_e = 93$ eV and $\epsilon_e = 99$ eV the PMMs show pronounced time-dependent features. Although the absolute change of the signal during time is approximately the same in both cases, the overall contrast is much better for the PMMs at $\epsilon_e = 99$ eV. Moreover, background features from the ground state would also influence the PMMs at $\epsilon_e = 93$ eV. We see that the signal and the sensitivity for imaging the time-dependent features in the PMMs strongly depend on the

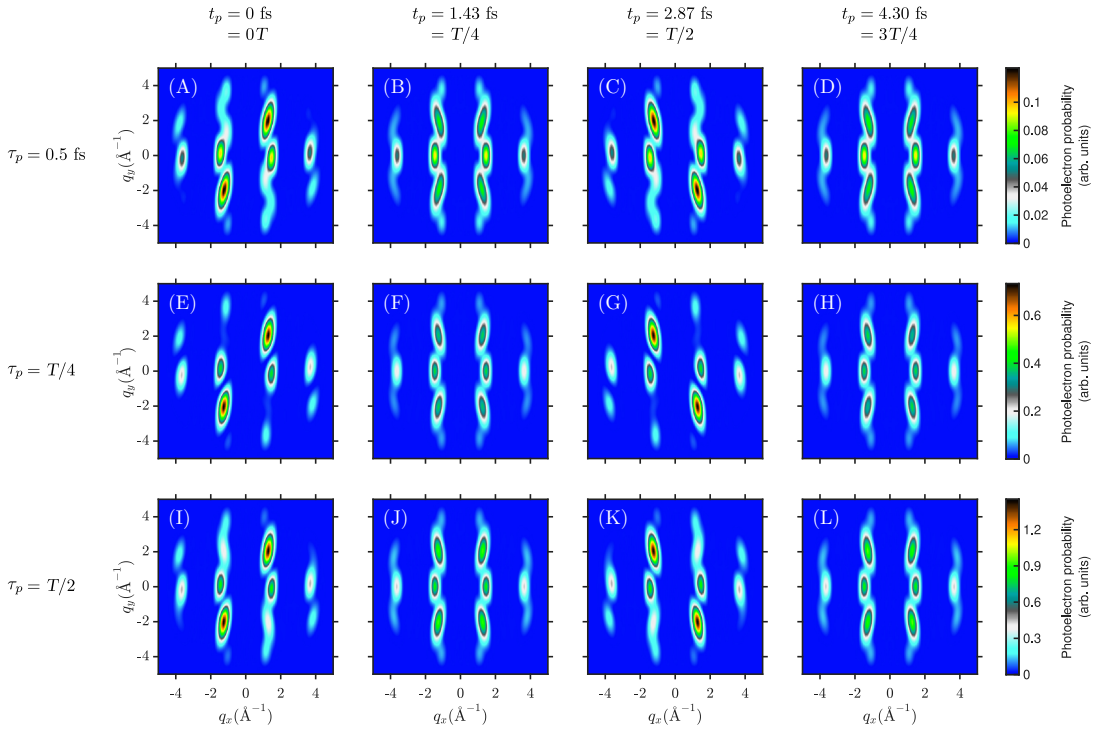


Figure 6.6.: Time evolution of the PMMs where the probe pulse detaches the photoelectron at (A),(E),(F) $t_p = 0T$, (B),(F),(J) $t_p = T/4$, (C),(G),(K) $t_p = T/2$, (D),(H),(L) $t_p = 3/4T$ from the excited pentacene. The probe pulse duration is (A)-(D) $\tau_p = 0.5$ fs, (E)-(H) $\tau_p = T/4$, (I)-(J) $\tau_p = T/2$ and has a center photon energy of $\omega_{in} = 100$ eV. The PMMs are averaged for photoelectron energies of $(98.5 - 99.5)$ eV, simulating an energy resolution of 1 eV. Adapted from Ref. [209].

photoelectron energy. We can understand the photoelectron probability from photoexcited electrons as a direct probe of the photoinduced dynamics. Changes in the photoelectron probability arising from lower bound electrons can be understood as an "indirect probe" of photoinduced dynamics since it measures the hole density. Therefore measuring the pump pulse photoexcited electrons leads to a background-free measurement of the time-dependent features, with a low contribution from the ground state.

We want to address how the results depend on the time and energy resolution, which are limited in a possible experiment. We simulate an energy resolution of 1 eV by averaging the PMMs over an energy interval of 1 eV. The PMMs averaged for photoelectron energies

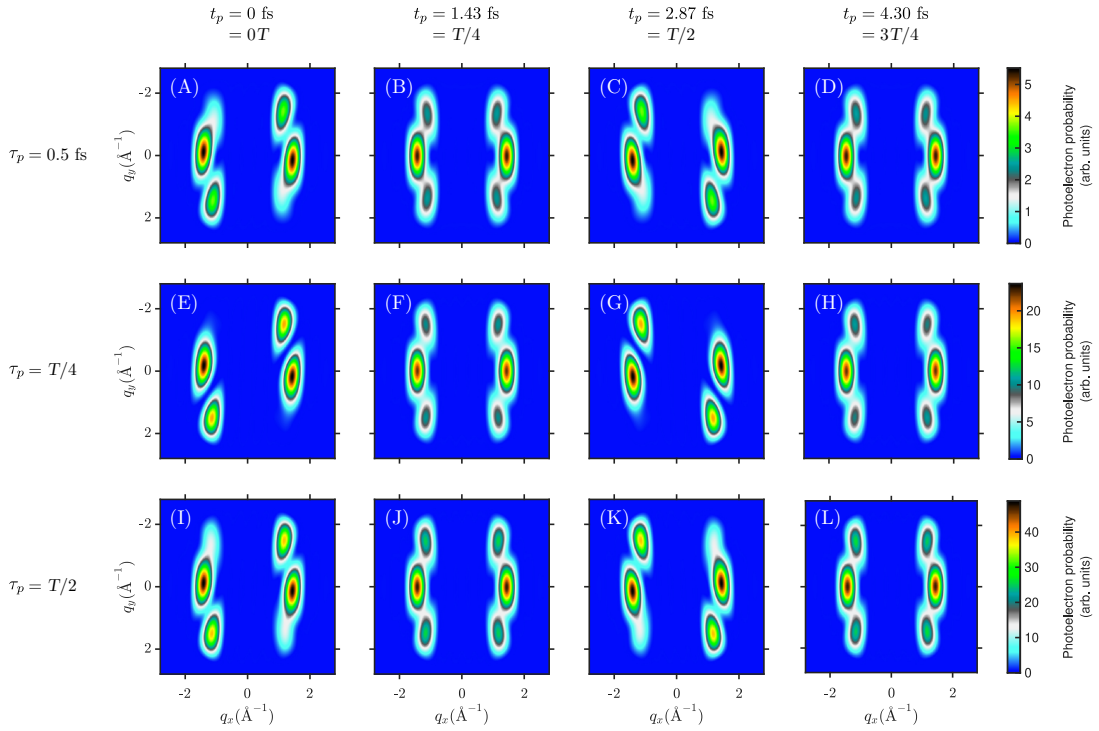


Figure 6.7.: Time evolution of the PMMs where the probe pulse detaches the photoelectron at (A),(E),(F) $t_p = 0T$, (B),(F),(J) $t_p = T/4$, (C),(G),(K) $t_p = T/2$, (D),(H),(L) $t_p = 3/4T$ from the excited pentacene. The probe pulse duration is (A)-(D) $\tau_p = 0.5$ fs, (E)-(H) $\tau_p = T/4$, (I)-(J) $\tau_p = T/2$ and has a center photon energy of $\omega_{in} = 30$ eV. The PMMs are averaged for photoelectron energies of $(28.5 - 29.5)$ eV, simulating an energy resolution of 1 eV.

from (98.5-99.5) eV are shown in Fig. 6.6(A)-(D). The obtained PMMs do not significantly change by the limited energy resolution. Further, we consider the time resolution by increasing the duration of the probe pulse. In an experiment, the time resolution is not only given by the duration of the probe pulse but also by the synchronization between the pump and probe pulse. We consider both of these effects by just increasing the probe pulse duration. Changing the probe pulse duration only causes slight changes in the PMMs (Fig. 6.6(E)-(L)). Therefore, even for large probe pulse durations up to half of the oscillation period, the PMMs still allows imaging of the charge migration in pentacene.

Finally, we want to investigate if a measurement of these dynamics is also possible with a probe pulse with less pulse energy, like the energy of the HHG sources involved in the study in Ch. 4 and Ch. 5. The calculated PMMs (averaged from photoelectron energies of (28.5-29.5) eV) for a probe pulse with photon energy of $\omega_{in} = 30$ eV for different pulse durations is in Fig. 6.7. The oscillations in the PMMs are still visible. However, the time-dependent oscillations of the signal are less pronounced. Moreover, the fine (light blue) structure of the PMMs disappears. Nevertheless, even for probe pulses with less photon energy, the results show that following charge migration is still possible, even up to probe pulse durations of half an oscillation period.

## 6.4. Summary

In summary, we have shown that photoelectron momentum microscopy can image charge migration in neutral photoexcited molecules on the attosecond timescale. The charge migration is considered as a superposition of the two lowest excited states of pentacene. With an XUV probe pulse (photon energy of 100 eV), charge migration could be followed in the PMMs with atomic spatial resolution. Based on previous studies on the decoherence in such systems [230, 229], the electronic coherence should be preserved in the first oscillation period of about 6 fs. The angle-integrated photoelectron distributions cannot resolve the charge oscillation in pentacene. We demonstrated that the distribution of the high-energy photoelectrons, corresponding to the electrons which have been excited in the system by the pump pulse, allows a ground state and background-free measurement of the charge migration with high contrast. The high-energy electrons are connected to the negative part in the photoinduced electron-hole density. Further, the high contrast and the background-free measurement are advantageous for the data quality in a possible experiment. We also showed that following the charge migration is possible for energy resolution up to 1 eV and higher time (probe pulse durations up to half of the oscillation period) resolution.

These results showed that photoelectron momentum microscopy is promising for imaging electronic coherences in molecular systems. Also, the decoherence of such a system could be studied experimentally by deviation from the calculated results. In the future, such an experiment will enable better understanding of charge transfer in organic semiconductors on femtosecond down to the attosecond timescales.

# 7. Conclusion

The extension of orbital tomography into the time domain needs theoretical models for the interpretation of the data. This extension brings us closer to the goal of a complete movie of isolated molecules or molecule substrate interplay. In this thesis, I investigated the possibility of photoelectron momentum microscopy for imaging photoexcited dynamics in molecular systems down to attosecond time and atomic spatial resolution. To achieve these goals, I derived equations for the photoelectron momentum distributions from excited states in molecules.

In Ch. 4, I studied the time-resolved properties of a pentacene film on Ag(110). Together with the experimental data from our collaborators, we showed the possibility of orbital tomography in the time domain with a time resolution of hundreds of femtoseconds at FELs. A comparison of my theoretical results allowed the interpretation of the experimental data. We were able to identify frontier orbitals of pentacene in the measurement. Based on my calculations on isolated pentacene and pentacene on a slab of silver atoms, we could disentangle molecular and substrate features in the photoelectron momentum maps. We revealed that the dynamics differ in the different molecular layers upon excitation. The results indicate that the distance between the substrate and the pentacene molecules in direct contact with the substrate changes after the excitation. The dynamics of the molecules in the outermost layer are decoupled from the substrate. The transient changes in the PMM of the HOMO resemble the geometrical relaxation of excited isolated pentacene. We demonstrated the capabilities of measuring the dynamics of isolated molecules in a sample, where molecules are adsorbed on a substrate. This possibility is promising for studying aligned isolated molecules without needing an alignment in the gas phase.

In a similar study (Ch. 5), I performed calculations on the isolated molecule CuPc and compared it with experimental data from our collaborators obtained for CuPc adsorbed

on $TiSe_2$. Upon excitation, hot electrons transfer from the substrate into orbitals of CuPc above the HOMO. We revealed that the symmetry of this excited state in CuPc must be broken, which is most probably caused by the interaction with the substrate. Simultaneously, the HOMO gets unoccupied by hot hole transfer across the interface and reaches its minimum after the decay of the excited state in CuPc. At the minimum, in the HOMO population, we could identify that about 55% of the CuPc molecules in the system are singly ionized. We revealed this by comparing my calculation of angle-averaged photoelectron distributions from C1s core levels to the experimental tr-XPS data. Such a supercharging of the molecules causes structural arrangements in the molecular film. My calculations involving a pair potential showed that the interaction between neutral and ionized CuPc molecules causes a rotation. In agreement with the experimental data, the neutral and ionized molecules rotate in opposite directions. We showed that combining a measurement of photoelectrons from core and valence states allows us to gain insights into structural and electronic properties.

With my calculations on pentacene and CuPc, we interpreted the dynamics measured in the experiments. Calculating dynamics in such big systems is challenging and currently impossible up to several hundreds of femtoseconds. Therefore I did not calculate excited-state dynamics explicitly (e.g., time propagation of the electron wavefunction). However, our static calculations at particular states, which could occur during the dynamics, allowed us to obtain the electronic and structural properties of the samples in the experiment.

For a theoretical investigation of excited state dynamics, I studied the possibility of photoelectron momentum microscopy for imaging charge oscillations in neutral photoexcited molecules (Ch. 6). I considered charge migration triggered by a pump pulse, described by a superposition of excited states. I showed that for pentacene, the angle-dependent photoelectron distributions could measure the considered charge migration down to the attosecond timescale, while angle-integrated cannot. Imaging the photoelectron distribution emitted from electrons excited by the pump pulse allows a background-free measurement with high contrast, which is advantageous in possible experiments. The charge migration even can be obtained for limited energy resolution (1 eV), and durations of the probe pulse up to half of the oscillation period of the charge migration.

Finally, within this thesis, we showed that our extension of photoelectron momentum

microscopy for excited states in molecules has several important applications. The calculations could already give insights into the time-resolved properties of current experiments. The ongoing development of FEL light sources, e.g., the increase in the repetition rate at LCLS-II, allows data acquisition for such experiments, which is currently impossible. Investigation in the future will reveal time-resolved information about dynamics in molecules and the interplay between molecules and surfaces. Our approach also showed what could be possible in experiments for imaging ultrafast charge migration. More sophisticated theoretical methods will also allow us to compute the dynamics on larger timescales. Future investigations with similar setups will push the understanding and development of organic semiconductors forward.

# A. Appendix

## A.1. Coupling of angular momentum

In a system of multiple interacting electrons, the angular momenta of the electrons can couple to form states which are eigenfunctions of the spin projection operator $\hat{S}_z$ and also total spin operator $\hat{S}^2$. In the case of a wavefunction constructed from a SD, the spin part of each electronic wavefunction are multiplied by each other, and we write this down as $|\sigma_1, \sigma_2 ...\rangle$. Another basis would be to construct CSFs which are given by the total angular momentum $J$ and the projection $m$: $|J, m\rangle$, and are also eigenfunctions of the corresponding operators $\hat{S}_z$ and $\hat{S}^2$. The transformation of SDs to the CSFs is now derived for two and three electrons.

From a quantum treatment of the angular momentum, the ladder operators for increasing and decreasing the spin projection value are

$$\hat{J}_+ |J, m\rangle = \sqrt{J(J+1) - m(m+1)}\, |J, m+1\rangle\,, \tag{A.1}$$

$$\hat{J}_- |J, m\rangle = \sqrt{J(J+1) - m(m-1)}\, |J, m-1\rangle\,, \tag{A.2}$$

where $\hat{J}_+$ raises and $\hat{J}_-$ lowers the projection value of the angular momentum by one. The coupling of two different angular momentum $J_1$ and $J_2$ with their projection values $-J \leq m \leq J$ has certain selection rules, leading to functions with an angular momentum $J_3 = J_1 \oplus J_2$, which follows as a linear combination of the single ones

$$J_3 = |J_1 - J_2|, |J_1 - J_2| + 1, \ldots, J_1 + J_2, \tag{A.3}$$

$$m_3 = m_1 + m_2. \tag{A.4}$$

This coupling results in wavefunctions which are eigenfunctions of the total angular momentum. Note that the basis sets need to be orthonormal.

### A.1.1. Two Spins

First of all, we start with the coupling of the spins from two electrons. From the selection rules, we end up with four different functions, which are a superposition of the single-particle states $|\uparrow\rangle, |\downarrow\rangle$. We can write down two of the final states since the spin projection 1 and -1 is only possible by coupling the states

$$|1,1\rangle = |\uparrow\uparrow\rangle\,, \tag{A.5}$$

$$|1,-1\rangle = |\downarrow\downarrow\rangle\,. \tag{A.6}$$

The other two eigenfunctions $|1,0\rangle$, $|0,0\rangle$ are a superposition of the mixed states $|\uparrow\downarrow\rangle, |\downarrow\uparrow\rangle$. With the ladder operators, we get

$$\begin{aligned} |1,0\rangle &= \frac{1}{\sqrt{2}}\hat{J}_- |1,1\rangle \\ &= \frac{1}{\sqrt{2}}\left(|\uparrow\downarrow\rangle + |\downarrow\uparrow\rangle\right). \end{aligned} \tag{A.7}$$

The last remaining state is also a superposition of $|1,0\rangle$, $|0,0\rangle$ one could make the ansatz

$$|0,0\rangle = \frac{1}{\sqrt{2}}\left(c_1\,|\uparrow\downarrow\rangle + c_2\,|\downarrow\uparrow\rangle\right). \tag{A.8}$$

The coefficients are evaluated with the relations $\langle 1,0|0,0\rangle = 0$ and $\langle 0,0|0,0\rangle = 1$. We end up with

$$|0,0\rangle = \frac{1}{\sqrt{2}}\left(|\uparrow\downarrow\rangle - |\downarrow\uparrow\rangle\right). \tag{A.9}$$

We see that the state in Eq. (A.9) is the spin singlet state, and the one in Eq. (A.7) is the spin-triplet state.

### A.1.2. Three Spins

The coupling of the spin of three electrons follows the same procedure as the latter. The third spin now couples to the wavefunctions derived for the two spin coupling leading to

the following two and one electron coupled functions

$$\left|\frac{3}{2},\frac{3}{2}\right\rangle_1 = |1,1\rangle\,|\uparrow\rangle \tag{A.10}$$

$$\left|\frac{3}{2},\frac{1}{2}\right\rangle_1 = |1,1\rangle\,|\downarrow\rangle \oplus |1,0\rangle\,|\uparrow\rangle \tag{A.11}$$

$$\left|\frac{3}{2},-\frac{1}{2}\right\rangle_1 = |1,0\rangle\,|\downarrow\rangle \oplus |1,-1\rangle\,|\uparrow\rangle \tag{A.12}$$

$$\left|\frac{3}{2},-\frac{3}{2}\right\rangle_1 = |1,-1\rangle\,|\downarrow\rangle \tag{A.13}$$

$$\left|\frac{1}{2},\frac{1}{2}\right\rangle_1 = |1,1\rangle\,|\downarrow\rangle \oplus |1,0\rangle\,|\uparrow\rangle \tag{A.14}$$

$$\left|\frac{1}{2},-\frac{1}{2}\right\rangle_1 = |1,0\rangle\,|\downarrow\rangle \oplus |1,-1\rangle\,|\uparrow\rangle \tag{A.15}$$

$$\left|\frac{1}{2},\frac{1}{2}\right\rangle_0 = |0,0\rangle\,|\uparrow\rangle \tag{A.16}$$

$$\left|\frac{1}{2},\frac{1}{2}\right\rangle_0 = |0,0\rangle\,|\downarrow\rangle\,. \tag{A.17}$$

Note that, e.g., the total function in Eq. (A.14) and Eq. (A.16) have the same total spin $J_3$ and spin projection value $m_3$, they result from a different $J_1$ and $J_2$ and are therefore different CSF. Therefore one ends up with eight different functions for three particles. If the total spin function is given by one product of the two single states, the coupling of the spins leads to

$$\left|\frac{3}{2},\frac{3}{2}\right\rangle_1 = |\uparrow\uparrow\uparrow\rangle \tag{A.18}$$

$$\left|\frac{3}{2},-\frac{3}{2}\right\rangle_1 = |\downarrow\downarrow\downarrow\rangle \tag{A.19}$$

$$\left|\frac{1}{2},\frac{1}{2}\right\rangle_0 = \frac{1}{\sqrt{2}}\left(|\uparrow\downarrow\uparrow\rangle - |\downarrow\uparrow\uparrow\rangle\right) \tag{A.20}$$

$$\left|\frac{1}{2},-\frac{1}{2}\right\rangle_0 = \frac{1}{\sqrt{2}}\left(|\uparrow\downarrow\downarrow\rangle - |\downarrow\uparrow\downarrow\rangle\right). \tag{A.21}$$

The remaining four functions could now be evaluated similarly to the coupling of two spins. With the ladder operator and the basis $\left|\frac{3}{2},\frac{3}{2}\right\rangle_1$ one get the functions for $J = \frac{3}{2}$

$$\left|\frac{3}{2},\frac{1}{2}\right\rangle_1 = \frac{1}{\sqrt{3}}\left(|\uparrow\uparrow\downarrow\rangle + |\uparrow\downarrow\uparrow\rangle + |\downarrow\uparrow\uparrow\rangle\right) \tag{A.22}$$

$$\left|\frac{3}{2},-\frac{1}{2}\right\rangle_1 = \frac{1}{\sqrt{3}}\left(|\downarrow\downarrow\uparrow\rangle + |\downarrow\uparrow\downarrow\rangle + |\uparrow\downarrow\downarrow\rangle\right). \tag{A.23}$$

The remaining states now use the orthogonality and the normalization to evaluate the linear combination coefficients of the states written down in eq. A.14 and A.15. This gives

$$\left|\frac{1}{2},\frac{1}{2}\right\rangle_1 = \frac{1}{\sqrt{6}}\left(2\left|\uparrow\uparrow\downarrow\right\rangle - \left|\uparrow\downarrow\uparrow\right\rangle - \left|\downarrow\uparrow\uparrow\right\rangle\right) \tag{A.24}$$

$$\left|\frac{1}{2},-\frac{1}{2}\right\rangle_1 = -\frac{1}{\sqrt{6}}\left(2\left|\downarrow\downarrow\uparrow\right\rangle - \left|\downarrow\uparrow\downarrow\right\rangle - \left|\uparrow\downarrow\downarrow\right\rangle\right). \tag{A.25}$$

### A.1.3. Clebsch-Gordan Coefficients

For the general evaluation, one could make use of the Clebsch-Gordan coefficients. The Clebsch-Gordan coefficients transform the function in the SD basis and the CSF. Since we do not need the explicit CSF for more than three coupled spins, details can be found in [82].

## A.2. Pair potential calculation including CuPc and the substrate

Here we address the influence of the substrate in the pair potential as an extension of 5.6. In our model, we consider the substrate as a cluster of atoms below the molecular layer. In the case of the unexcited structure, the interaction with the substrate would lead to an additional term in the pair potential

$$\Phi_{total,t_{-1}} = \Phi_{M\leftrightarrow S,t_{-1}} + \Phi_{M\leftrightarrow S,t_{-1}}, \tag{A.26}$$

where $\Phi_{M\leftrightarrow S,t_{-1}}$ is the pair potential between all CuPc molecules and $\Phi_{M\leftrightarrow S,t_{-1}}$ is the pair potential between the molecules and the substrate. The LEED data on the sample showed a point-of-line arrangement of the molecules, resulting in different adsorption sites for the molecules on the substrate. Since all CuPc molecules are orientated equally, the dependency of $\Phi_{\mathrm{CuPc^0},\mathrm{TiSe_2},t_{-1}}$ on the angle $\alpha$ should not be pronounced. Therefore we consider that for each arrangement of CuPc, the contribution from the substrate is constant for changing values of $\alpha$.

In the case of the excited structure, nearly half of the molecules are positively charged, while the substrate is negatively charged. The charging increases the interaction between the substrate and the molecular layer. This is also indicated by the bending of the charged molecule as shown by DFT calculation of our collaborators. The pair potential for the

excited structure including the substrate is

$$\Phi_{total,t_1} = \Phi_{M\leftrightarrow M,t_1} + \Phi_{M\leftrightarrow S,t_1}, \tag{A.27}$$

where $\Phi_{M\leftrightarrow M,t_1}$ is the pair potential between the CuPc molecules and $\Phi_{M\leftrightarrow S,t_1}$ between the CuPc molecules and the substrate. We can rewrite it with the pair potential between the molecule substrate at $t_{-1}$ as

$$\Phi_{total,t_1} = \Phi_{M\leftrightarrow M,t_1} + \Phi_{M\leftrightarrow S,t_1} - \Phi_{M\leftrightarrow S,t_{-1}} + \Phi_{M\leftrightarrow S,t_{-1}}. \tag{A.28}$$

Since the molecule substrate interaction in the unexcited structure is considered as a constant function of $\alpha$, $\Phi_{M\leftrightarrow S,t_{-1}} = Const.$. The difference between the pair potential of the molecule and substrate in the unexcited and excited structure is

$$\Phi_{M\leftrightarrow S,t_1} - \Phi_{M\leftrightarrow S,t_{-1}} = \underbrace{\Phi^{vdW}_{M\leftrightarrow S,t_1} - \Phi^{vdW}_{M\leftrightarrow S,t_{-1}}}_{\Delta\Phi^{vdW}_{M\leftrightarrow S,t_{-1},t_1}} + \underbrace{\Phi^{El}_{M\leftrightarrow S,t_1} - \Phi^{El}_{M\leftrightarrow S,t_{-1}}}_{\Delta\Phi^{El}_{M\leftrightarrow S,t_{-1},t_1}}. \tag{A.29}$$

The experimental data at time $t_1 = 375\ fs$ showed that the charge in the substrate is distributed in the 3d bands of the titanium atoms. Therefore $\Delta\Phi^{eL}_{M\leftrightarrow S,t_{-1},t_1}$ is approximated by the interaction between the molecule and the titanium atoms. To keep the total charge of the system conserved, we add a charge of half an electron to all the involved titanium atoms for every CuPc molecule in the structure. We consider structural changes (e.g., bending) to be negligible as a function of the orientation angles of the molecules. We also consider that the change in the van der Waals potential $\Delta\Phi^{vdW}_{M\leftrightarrow S,t_{-1},t_1}$ does not depend on the adsorption angles, resulting in

$$\Phi_{total,t_1} \approx \Phi_{M\leftrightarrow M,t_1} + \Delta\Phi^{El}_{M\leftrightarrow S,t_{-1},t_1} + const. \tag{A.30}$$

The result of this pair potential is shown in Fig. A.1 for four different distances between neighboring molecules. Despite an overall shift of the pair potential, we do not obtain any change in the pair potential compared to the one in Fig. 5.10, which only includes the potential between the molecules. Therefore we assume the influence of the substrate to be small.

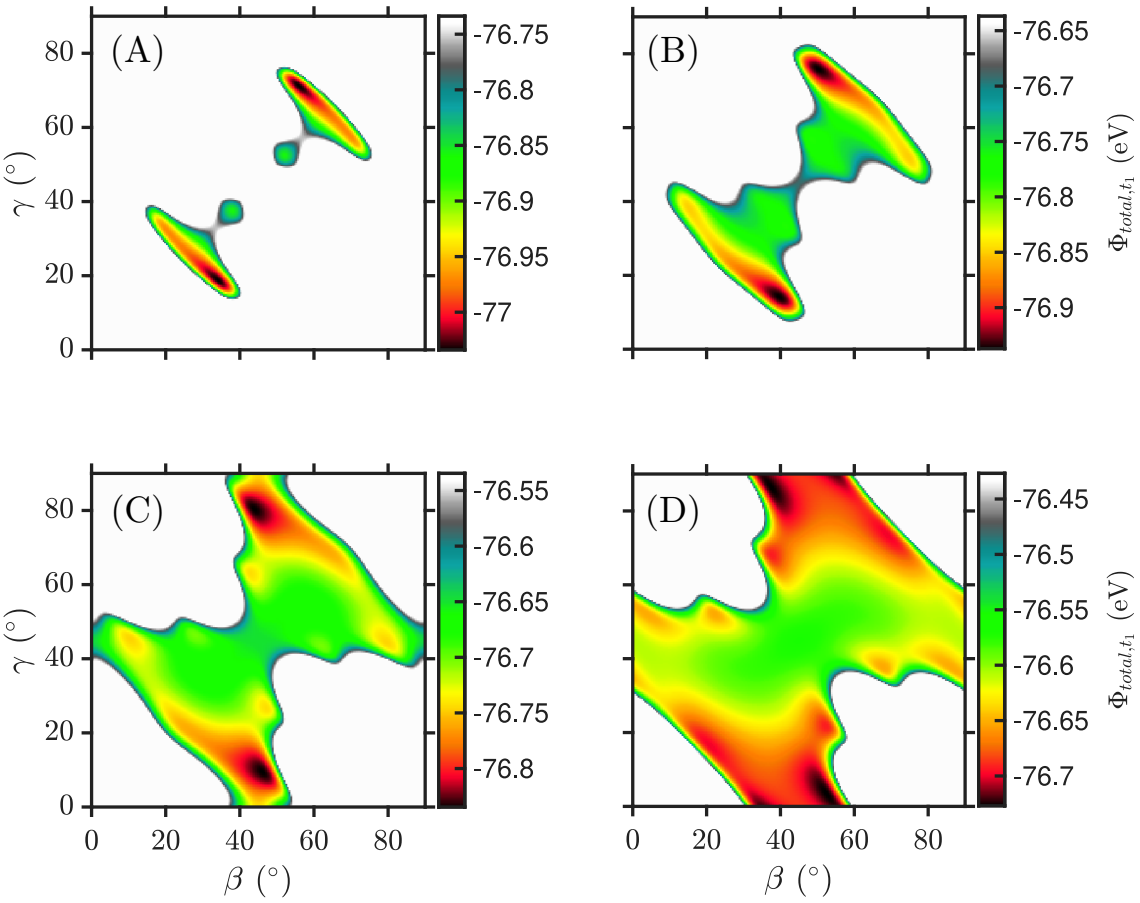


Figure A.1.: Pair potential $\Phi_{total,t_1}$ for the excited structure with considering the interaction of the substrate. The pair potential depends on the angles $\beta$ and $\gamma$ describing the rotation of the neutral and ionized CuPc correspondingly and is shown for different distances between the next-neighbor molecules with (A) $d = 14.0$ Å, (B) $d = 14.5$ Å, (C) $d = 15.0$ Å, and (D) $d = 15.5$ Å. Adapted from Ref. [165].

# Bibliography

[1] Li, Y. *et al.* Recent progress in organic solar cells: A review on materials from acceptor to donor. *Molecules* **27** (2022). URL https://www.mdpi.com/1420-3049/27/6/1800.

[2] Murphy, A. R. & Fréchet, J. M. J. Organic semiconducting oligomers for use in thin film transistors. *Chemical Reviews* **107**, 1066–1096 (2007). URL https://doi.org/10.1021/cr0501386. PMID: 17428023, https://doi.org/10.1021/cr0501386.

[3] Chen, Y. *et al.* Flexible inorganic bioelectronics. *npj Flexible Electronics* **4**, 2 (2020). URL https://doi.org/10.1038/s41528-020-0065-1.

[4] Burroughes, J. H. *et al.* Light-emitting diodes based on conjugated polymers. *Nature* **347**, 539–541 (1990). URL https://doi.org/10.1038/347539a0.

[5] Borchardt, J. K. Developments in organic displays. *Materials Today* **7**, 42–46 (2004). URL https://www.sciencedirect.com/science/article/pii/S1369702104004018.

[6] Logothetidis, S. Flexible organic electronic devices: Materials, process and applications. *Materials Science and Engineering: B* **152**, 96–104 (2008). URL https://www.sciencedirect.com/science/article/pii/S0921510708002316. 4th International Workshop on Nanosciences and Nanotechnologies (NN07).

[7] Hong, G. *et al.* A brief history of oleds—emitter development and industry milestones. *Advanced Materials* **33**, 2005630 (2021). URL https://onlinelibrary.wiley.com/doi/abs/10.1002/adma.202005630. https://onlinelibrary.wiley.com/doi/pdf/10.1002/adma.202005630.

[8] Best Research-Cell Efficiency Chart, National Renewable Energy Laboratory

(NREL), https://www.nrel.gov/pv/cell-efficiency.html (accessed: 2023-04-18).

[9] Meng, L. *et al.* Organic and solution-processed tandem solar cells with 17.3% efficiency. *Science* **361**, 1094–1098 (2018). URL https://www.science.org/doi/abs/10.1126/science.aat2612. https://www.science.org/doi/pdf/10.1126/science.aat2612.

[10] Chen, H. *et al.* A guest-assisted molecular-organization approach for >17% efficiency organic solar cells using environmentally friendly solvents. *Nature Energy* **6**, 1045–1053 (2021). URL https://doi.org/10.1038/s41560-021-00923-5.

[11] Song, J. *et al.* High-efficiency organic solar cells with low voltage loss induced by solvent additive strategy. *Matter* **4**, 2542–2552 (2021). URL https://www.sciencedirect.com/science/article/pii/S2590238521002800.

[12] Coropceanu, V., Chen, X.-K., Wang, T., Zheng, Z. & Brédas, J.-L. Charge-transfer electronic states in organic solar cells. *Nature Reviews Materials* **4**, 689–707 (2019). URL https://doi.org/10.1038/s41578-019-0137-9.

[13] Haneef, H. F., Zeidell, A. M. & Jurchescu, O. D. Charge carrier traps in organic semiconductors: a review on the underlying physics and impact on electronic devices. *J. Mater. Chem. C* **8**, 759–787 (2020). URL http://dx.doi.org/10.1039/C9TC05695E.

[14] Köhler, A. & Bässler, H. *Electronic processes in organic semiconductors: An introduction* (John Wiley & Sons, 2015).

[15] Corkum, P. B. & Krausz, F. Attosecond science. *Nature Physics* **3**, 381–387 (2007). URL https://doi.org/10.1038/nphys620.

[16] Krausz, F. & Ivanov, M. Attosecond physics. *Rev. Mod. Phys.* **81**, 163–234 (2009). URL https://link.aps.org/doi/10.1103/RevModPhys.81.163.

[17] Goulielmakis, E. *et al.* Real-time observation of valence electron motion. *Nature* **466**, 739–743 (2010). URL https://doi.org/10.1038/nature09212.

[18] Calegari, F. *et al.* Ultrafast electron dynamics in phenylalanine initiated by attosecond pulses. *Science* **346**, 336–339 (2014). URL https://www.science.org/doi/

abs/10.1126/science.1254061. https://www.science.org/doi/pdf/10.1126/science.1254061.

[19] Nisoli, M., Decleva, P., Calegari, F., Palacios, A. & Martín, F. Attosecond electron dynamics in molecules. *Chemical Reviews* **117**, 10760–10825 (2017). URL https://doi.org/10.1021/acs.chemrev.6b00453. PMID: 28488433, https://doi.org/10.1021/acs.chemrev.6b00453.

[20] Paul, P. M. *et al.* Observation of a train of attosecond pulses from high harmonic generation. *Science* **292**, 1689–1692 (2001). URL https://www.science.org/doi/abs/10.1126/science.1059413. https://www.science.org/doi/pdf/10.1126/science.1059413.

[21] Hentschel, M. *et al.* Attosecond metrology. *Nature* **414**, 509–513 (2001). URL https://doi.org/10.1038/35107000.

[22] Chini, M., Zhao, K. & Chang, Z. The generation, characterization and applications of broadband isolated attosecond pulses. *Nature Photonics* **8**, 178–186 (2014). URL https://doi.org/10.1038/nphoton.2013.362.

[23] Krausz, F. The birth of attosecond physics and its coming of age. *Physica Scripta* **91**, 063011 (2016). URL https://dx.doi.org/10.1088/0031-8949/91/6/063011.

[24] Gaumnitz, T. *et al.* Streaking of 43-attosecond soft-x-ray pulses generated by a passively cep-stable mid-infrared driver. *Opt. Express* **25**, 27506–27518 (2017). URL https://opg.optica.org/oe/abstract.cfm?URI=oe-25-22-27506.

[25] Chapman, H. N. *et al.* Femtosecond diffractive imaging with a soft-x-ray free-electron laser. *Nature Physics* **2**, 839–843 (2006). URL https://doi.org/10.1038/nphys461.

[26] Emma, P. *et al.* First lasing and operation of an ångstrom-wavelength free-electron laser. *Nature Photonics* **4**, 641–647 (2010). URL https://doi.org/10.1038/nphoton.2010.176.

[27] Ishikawa, T. *et al.* A compact x-ray free-electron laser emitting in the sub-ångström region. *Nature Photonics* **6**, 540–544 (2012). URL https://doi.org/10.1038/nphoton.2012.141.

[28] Duris, J. *et al.* Tunable isolated attosecond x-ray pulses with gigawatt peak power from a free-electron laser. *Nature Photonics* **14**, 30–36 (2020). URL https://doi.org/10.1038/s41566-019-0549-5.

[29] Maroju, P. K. *et al.* Attosecond pulse shaping using a seeded free-electron laser. *Nature* **578**, 386–391 (2020). URL https://doi.org/10.1038/s41586-020-2005-6.

[30] Sansone, G. *et al.* Electron localization following attosecond molecular photoionization. *Nature* **465**, 763–766 (2010). URL https://doi.org/10.1038/nature09084.

[31] Kraus, P. M. *et al.* Measurement and laser control of attosecond charge migration in ionized iodoacetylene. *Science* **350**, 790–795 (2015). URL https://www.science.org/doi/abs/10.1126/science.aab2160. https://www.science.org/doi/pdf/10.1126/science.aab2160.

[32] Wallauer, R. *et al.* Tracing orbital images on ultrafast time scales. *Science* **371**, 1056–1059 (2021). URL https://www.science.org/doi/abs/10.1126/science.abf3286. https://www.science.org/doi/pdf/10.1126/science.abf3286.

[33] Erk, B. *et al.* Ultrafast charge rearrangement and nuclear dynamics upon inner-shell multiple ionization of small polyatomic molecules. *Phys. Rev. Lett.* **110**, 053003 (2013). URL https://link.aps.org/doi/10.1103/PhysRevLett.110.053003.

[34] Liekhus-Schmaltz, C. E. *et al.* Ultrafast isomerization initiated by x-ray core ionization. *Nature Communications* **6**, 8199 (2015). URL https://doi.org/10.1038/ncomms9199.

[35] Berrah, N. *et al.* Femtosecond-resolved observation of the fragmentation of buckminsterfullerene following x-ray multiphoton ionization. *Nature Physics* **15**, 1279–1283 (2019). URL https://doi.org/10.1038/s41567-019-0665-7.

[36] Boll, R. *et al.* Femtosecond photoelectron diffraction on laser-aligned molecules: Towards time-resolved imaging of molecular structure. *Phys. Rev. A* **88**, 061402 (2013). URL https://link.aps.org/doi/10.1103/PhysRevA.88.061402.

[37] Minitti, M. P. *et al.* Imaging molecular motion: Femtosecond x-ray scattering of an electrocyclic chemical reaction. *Phys. Rev. Lett.* **114**, 255501 (2015). URL https://link.aps.org/doi/10.1103/PhysRevLett.114.255501.

[38] Zewail, A. H. Femtochemistry: Atomic-scale dynamics of the chemical bond. *The Journal of Physical Chemistry A* **104**, 5660–5694 (2000). URL https://doi.org/10.1021/jp001460h. https://doi.org/10.1021/jp001460h.

[39] Ott, C. *et al.* Reconstruction and control of a time-dependent two-electron wave packet. *Nature* **516**, 374–378 (2014). URL https://doi.org/10.1038/nature14026.

[40] Pertot, Y. *et al.* Time-resolved x-ray absorption spectroscopy with a water window high-harmonic source. *Science* **355**, 264–267 (2017). URL https://www.science.org/doi/abs/10.1126/science.aah6114. https://www.science.org/doi/pdf/10.1126/science.aah6114.

[41] Öström, H. *et al.* Probing the transition state region in catalytic co oxidation on ru. *Science* **347**, 978–982 (2015). URL https://www.science.org/doi/abs/10.1126/science.1261747. https://www.science.org/doi/pdf/10.1126/science.1261747.

[42] Milne, C., Penfold, T. & Chergui, M. Recent experimental and theoretical developments in time-resolved x-ray spectroscopies. *Coordination Chemistry Reviews* **277-278**, 44–68 (2014). URL https://www.sciencedirect.com/science/article/pii/S0010854514000630. Following Chemical Structures using Synchrotron Radiation.

[43] Attar, A. R. *et al.* Femtosecond x-ray spectroscopy of an electrocyclic ring-opening reaction. *Science* **356**, 54–59 (2017). URL https://www.science.org/doi/abs/10.1126/science.aaj2198. https://www.science.org/doi/pdf/10.1126/science.aaj2198.

[44] Dixit, G., Vendrell, O. & Santra, R. Imaging electronic quantum motion with light. *Proceedings of the National Academy of Sciences* **109**, 11636–11640 (2012). URL https://www.pnas.org/doi/abs/10.1073/pnas.1202226109. https://www.pnas.org/doi/pdf/10.1073/pnas.1202226109.

[45] Popova-Gorelova, D. & Santra, R. Imaging instantaneous electron flow with ultrafast resonant x-ray scattering. *Phys. Rev. B* **91**, 184303 (2015). URL https://link.aps.org/doi/10.1103/PhysRevB.91.184303.

[46] Kraus, P. M., Zürch, M., Cushing, S. K., Neumark, D. M. & Leone, S. R. The ultrafast x-ray spectroscopic revolution in chemical dynamics. *Nature Reviews Chemistry* **2**, 82–94 (2018). URL https://doi.org/10.1038/s41570-018-0008-8.

[47] Popova-Gorelova, D., Reis, D. A. & Santra, R. Theory of x-ray scattering from laser-driven electronic systems. *Phys. Rev. B* **98**, 224302 (2018). URL https://link.aps.org/doi/10.1103/PhysRevB.98.224302.

[48] Mayer, D. *et al.* Following excited-state chemical shifts in molecular ultrafast x-ray photoelectron spectroscopy. *Nature Communications* **13**, 198 (2022). URL https://doi.org/10.1038/s41467-021-27908-y.

[49] Al-Haddad, A. *et al.* Observation of site-selective chemical bond changes via ultrafast chemical shifts. *Nature Communications* **13**, 7170 (2022). URL https://doi.org/10.1038/s41467-022-34670-2.

[50] Fasel, R. *et al.* Orientation of adsorbed $c_{60}$ molecules determined via x-ray photoelectron diffraction. *Phys. Rev. Lett.* **76**, 4733–4736 (1996). URL https://link.aps.org/doi/10.1103/PhysRevLett.76.4733.

[51] Kazama, M. *et al.* Photoelectron diffraction from single oriented molecules: Towards ultrafast structure determination of molecules using x-ray free-electron lasers. *Phys. Rev. A* **87**, 063417 (2013). URL https://link.aps.org/doi/10.1103/PhysRevA.87.063417.

[52] Tsuru, S., Sako, T., Fujikawa, T. & Yagishita, A. Theory of time-resolved x-ray photoelectron diffraction from transient conformational molecules. *Phys. Rev. A* **95**, 043404 (2017). URL https://link.aps.org/doi/10.1103/PhysRevA.95.043404.

[53] Böker, T. *et al.* Band structure of $mos_2$, $mose_2$, and $\alpha - mote_2$ : angle-resolved photoelectron spectroscopy and ab initio calculations. *Phys. Rev. B* **64**, 235305 (2001). URL https://link.aps.org/doi/10.1103/PhysRevB.64.235305.

[54] Rohwer, T. *et al.* Collapse of long-range charge order tracked by time-resolved photoemission at high momenta. *Nature* **471**, 490–493 (2011). URL https://doi.org/10.1038/nature09829.

[55] Smallwood, C. L., Kaindl, R. A. & Lanzara, A. Ultrafast angle-resolved photoe-

mission spectroscopy of quantum materials. *Europhysics Letters* **115**, 27001 (2016). URL https://dx.doi.org/10.1209/0295-5075/115/27001.

[56] Nicholson, C. W. *et al.* Beyond the molecular movie: Dynamics of bands and bonds during a photoinduced phase transition. *Science* **362**, 821–825 (2018). URL https://science.sciencemag.org/content/362/6416/821. https://science.sciencemag.org/content/362/6416/821.full.pdf.

[57] Puschnig, P. *et al.* Reconstruction of molecular orbital densities from photoemission data. *Science (New York, N.Y.)* **326**, 702–706 (2009).

[58] Puschnig, P. & Ramsey, M. Photoemission tomography: Valence band photoemission as a quantitative method for investigating molecular films. In Wandelt, K. (ed.) *Encyclopedia of Interfacial Chemistry*, 380–391 (Elsevier, Oxford, 2018). URL https://www.sciencedirect.com/science/article/pii/B9780124095472137825.

[59] Mugarza, A., Ortega, J. E., Himpsel, F. J. & García de Abajo, F. J. Measurement of electron wave functions and confining potentials via photoemission. *Phys. Rev. B* **67**, 081404 (2003). URL https://link.aps.org/doi/10.1103/PhysRevB.67.081404.

[60] Lüftner, D. *et al.* Imaging the wave functions of adsorbed molecules. *Proceedings of the National Academy of Sciences* **111**, 605–610 (2014). URL https://www.pnas.org/doi/abs/10.1073/pnas.1315716110. https://www.pnas.org/doi/pdf/10.1073/pnas.1315716110.

[61] Kliuiev, P., Latychevskaia, T., Osterwalder, J., Hengsberger, M. & Castiglioni, L. Application of iterative phase-retrieval algorithms to arpes orbital tomography. *New Journal of Physics* **18**, 093041 (2016). URL https://dx.doi.org/10.1088/1367-2630/18/9/093041.

[62] Baumgärtner, K. *et al.* Ultrafast orbital tomography of a pentacene film using time-resolved momentum microscopy at a fel. *Nature Communications* **13**, 2741 (2022). URL https://doi.org/10.1038/s41467-022-30404-6.

[63] Neef, A. *et al.* Orbital-resolved observation of singlet fission. *Nature* **616**, 275–279 (2023). URL https://doi.org/10.1038/s41586-023-05814-1.

[64] Xia, J. *et al.* Singlet fission: Progress and prospects in solar cells. *Advanced Materials* **29**, 1601652 (2017). URL https://onlinelibrary.wiley.com/doi/abs/10.

1002/adma.201601652. https://onlinelibrary.wiley.com/doi/pdf/10.1002/adma.201601652.

[65] Helgaker, T., Jørgensen, P. & Olsen, J. *Molecular Electronic-Structure Theory* (John Wiley & Sons, Ltd, 2000).

[66] Jensen, F. *Introduction to Computational Chemistry* (John Wiley & Sons, Inc., Hoboken, NJ, USA, 2006).

[67] Born, M. & Oppenheimer, R. Zur quantentheorie der molekeln. *Annalen der Physik* **389**, 457–484 (1927). URL https://onlinelibrary.wiley.com/doi/abs/10.1002/andp.19273892002. https://onlinelibrary.wiley.com/doi/pdf/10.1002/andp.19273892002.

[68] Crespo-Otero, R. & Barbatti, M. Recent advances and perspectives on nonadiabatic mixed quantum–classical dynamics. *Chemical Reviews* **118**, 7026–7068 (2018). URL https://doi.org/10.1021/acs.chemrev.7b00577. PMID: 29767966, https://doi.org/10.1021/acs.chemrev.7b00577.

[69] Koopmans, T. Über die Zuordnung von Wellenfunktionen und Eigenwerten zu den Einzelnen Elektronen Eines Atoms. *Physica* **1**, 104–113 (1934).

[70] Boys, S. F. & Egerton, A. C. Electronic wave functions - i. a general method of calculation for the stationary states of any molecular system. *Proceedings of the Royal Society of London. Series A. Mathematical and Physical Sciences* **200**, 542–554 (1950). URL https://royalsocietypublishing.org/doi/abs/10.1098/rspa.1950.0036. https://royalsocietypublishing.org/doi/pdf/10.1098/rspa.1950.0036.

[71] Hill, J. G. Gaussian basis sets for molecular applications. *International Journal of Quantum Chemistry* **113**, 21–34 (2013). URL https://onlinelibrary.wiley.com/doi/abs/10.1002/qua.24355. https://onlinelibrary.wiley.com/doi/pdf/10.1002/qua.24355.

[72] Roothaan, C. C. J. New developments in molecular orbital theory. *Rev. Mod. Phys.* **23**, 69–89 (1951). URL https://link.aps.org/doi/10.1103/RevModPhys.23.69.

[73] Lischka, H. *et al.* Multireference approaches for excited states of molecules. *Chemical*

*Reviews* **118**, 7293–7361 (2018). URL https://doi.org/10.1021/acs.chemrev.8b00244. PMID: 30040389, https://doi.org/10.1021/acs.chemrev.8b00244.

[74] Knowles, P. J. & Handy, N. C. Unlimited full configuration interaction calculations. *The Journal of Chemical Physics* **91**, 2396–2398 (1989). URL https://doi.org/10.1063/1.456997. https://pubs.aip.org/aip/jcp/article-pdf/91/4/2396/15357998/2396_1_online.pdf.

[75] Rossi, E., Bendazzoli, G. L., Evangelisti, S. & Maynau, D. A full-configuration benchmark for the n2 molecule. *Chemical Physics Letters* **310**, 530–536 (1999). URL https://www.sciencedirect.com/science/article/pii/S0009261499007915.

[76] Sugisaki, K. *et al.* Quantum algorithm for full configuration interaction calculations without controlled time evolutions. *The Journal of Physical Chemistry Letters* **12**, 11085–11089 (2021). URL https://doi.org/10.1021/acs.jpclett.1c03214. PMID: 34749498, https://doi.org/10.1021/acs.jpclett.1c03214.

[77] Olsen, J., Roos, B. O., Jo/rgensen, P. & Jensen, H. J. A. Determinant based configuration interaction algorithms for complete and restricted configuration interaction spaces. *The Journal of Chemical Physics* **89**, 2185–2192 (1988). URL https://doi.org/10.1063/1.455063. https://pubs.aip.org/aip/jcp/article-pdf/89/4/2185/11255374/2185_1_online.pdf.

[78] Malmqvist, P. Å., Rendell, A. & Roos, B. O. The restricted active space self-consistent-field method, implemented with a split graph unitary group approach. *Journal of Physical Chemistry* **94**, 5477–5482 (1990).

[79] Casanova, D. Restricted active space configuration interaction methods for strong correlation: Recent developments. *WIREs Computational Molecular Science* **12**, e1561 (2022). URL https://wires.onlinelibrary.wiley.com/doi/abs/10.1002/wcms.1561. https://wires.onlinelibrary.wiley.com/doi/pdf/10.1002/wcms.1561.

[80] Foresman, J. B., Head-Gordon, M., Pople, J. A. & Frisch, M. J. Toward a systematic molecular orbital theory for excited states. *The Journal of Physical Chemistry* **96**, 135–149 (1992). URL https://doi.org/10.1021/j100180a030. https://doi.org/10.1021/j100180a030.

[81] Tran, T., Segarra-Martí, J., Bearpark, M. J. & Robb, M. A. Molecular vertical excitation energies studied with first-order rasscf (ras[1,1]): Balancing covalent and ionic excited states. *The Journal of Physical Chemistry A* **123**, 5223–5230 (2019). URL https://doi.org/10.1021/acs.jpca.9b03715. PMID: 31150228, https://doi.org/10.1021/acs.jpca.9b03715.

[82] Helgaker, T., Jørgensen, P. & Olsen, J. *Spin in Second Quantization*, chap. 2, 34–79 (John Wiley & Sons, Ltd, 2000). URL https://onlinelibrary.wiley.com/doi/abs/10.1002/9781119019572.ch2. https://onlinelibrary.wiley.com/doi/pdf/10.1002/9781119019572.ch2.

[83] Santra, R. Concepts in x-ray physics. *Journal of Physics B: Atomic, Molecular and Optical Physics* **42**, 023001 (2008). URL https://dx.doi.org/10.1088/0953-4075/42/2/023001.

[84] Loudon, R. *The quantum theory of light* (OUP Oxford, 2000).

[85] Gottfried, K. & Yan, T.-M. *Electrodynamics*, 437–501 (Springer New York, New York, NY, 2003). URL https://doi.org/10.1007/978-0-387-21623-2_10.

[86] Popova-Gorelova, D., Küpper, J. & Santra, R. Imaging electron dynamics with time- and angle-resolved photoelectron spectroscopy. *Phys. Rev. A* **94**, 013412 (2016). URL https://link.aps.org/doi/10.1103/PhysRevA.94.013412.

[87] Einstein, A. Über einen die erzeugung und verwandlung des lichtes betreffenden heuristischen gesichtspunkt. *Annalen der Physik* **322**, 132–148 (1905). URL https://onlinelibrary.wiley.com/doi/abs/10.1002/andp.19053220607. https://onlinelibrary.wiley.com/doi/pdf/10.1002/andp.19053220607.

[88] Reinert, F. & Hüfner, S. Photoemission spectroscopy—from early days to recent applications. *New Journal of Physics* **7**, 97 (2005). URL https://dx.doi.org/10.1088/1367-2630/7/1/097.

[89] Siegbahn, K. & Edvarson, K. $\beta$-ray spectroscopy in the precision range of 1 : 105. *Nuclear Physics* **1**, 137–159 (1956). URL https://www.sciencedirect.com/science/article/pii/S0029558256800229.

[90] Siegbahn, K. Electron spectroscopy - an outlook. *Journal of Electron Spectroscopy and Related Phenomena* **5**, 3–97 (1974). URL https://www.sciencedirect.com/

science/article/pii/036820487485005X. The International Journal on Theoretical and Experimental Aspects of Electron Spectroscopy.

[91] Kobayashi, K. Hard x-ray photoemission spectroscopy. *Nuclear Instruments and Methods in Physics Research Section A: Accelerators, Spectrometers, Detectors and Associated Equipment* **601**, 32–47 (2009). URL https://www.sciencedirect.com/science/article/pii/S016890020802010X. Special issue in honour of Prof. Kai Siegbahn.

[92] Descostes, M., Mercier, F., Thromat, N., Beaucaire, C. & Gautier-Soyer, M. Use of xps in the determination of chemical environment and oxidation state of iron and sulfur samples: constitution of a data basis in binding energies for fe and s reference compounds and applications to the evidence of surface species of an oxidized pyrite in a carbonate medium. *Applied Surface Science* **165**, 288–302 (2000). URL https://www.sciencedirect.com/science/article/pii/S0169433200004438.

[93] Aziz, M. & Ismail, A. Chapter 5 - x-ray photoelectron spectroscopy (xps). In Hilal, N., Ismail, A. F., Matsuura, T. & Oatley-Radcliffe, D. (eds.) *Membrane Characterization*, 81–93 (Elsevier, 2017). URL https://www.sciencedirect.com/science/article/pii/B978044463776500005X.

[94] Roth, F. *et al.* Direct observation of charge separation in an organic light harvesting system by femtosecond time-resolved xps. *Nature Communications* **12**, 1196 (2021). URL https://doi.org/10.1038/s41467-021-21454-3.

[95] Liu, F. Time- and angle-resolved photoemission spectroscopy (tr-arpes) of tmdc monolayers and bilayers. *Chem. Sci.* **14**, 736–750 (2023). URL http://dx.doi.org/10.1039/D2SC04124C.

[96] Sobota, J. A., He, Y. & Shen, Z.-X. Angle-resolved photoemission studies of quantum materials. *Rev. Mod. Phys.* **93**, 025006 (2021). URL https://link.aps.org/doi/10.1103/RevModPhys.93.025006.

[97] Hüfner, S. *et al.* Photoemission spectroscopy in metals:: band structure-fermi surface–spectral function. *Journal of Electron Spectroscopy and Related Phenomena* **100**, 191–213 (1999). URL https://www.sciencedirect.com/science/article/pii/S036820489900047X.

[98] Zhang, H. *et al.* Angle-resolved photoemission spectroscopy. *Nature Reviews Methods Primers* **2**, 54 (2022). URL https://doi.org/10.1038/s43586-022-00133-7.

[99] Graus, M. *et al.* Electron-vibration coupling in molecular materials: Assignment of vibronic modes from photoelectron momentum mapping. *Phys. Rev. Lett.* **116**, 147601 (2016). URL https://link.aps.org/doi/10.1103/PhysRevLett.116.147601.

[100] Metzger, C. *et al.* Plane-wave final state for photoemission from nonplanar molecules at a metal-organic interface. *Physical Review B* **101**, 165421 (2020). URL https://link.aps.org/doi/10.1103/PhysRevB.101.165421. Publisher: American Physical Society.

[101] Maklar, J. *et al.* A quantitative comparison of time-of-flight momentum microscopes and hemispherical analyzers for time- and angle-resolved photoemission spectroscopy experiments. *Review of Scientific Instruments* **91** (2020). URL https://doi.org/10.1063/5.0024493. 123112, https://pubs.aip.org/aip/rsi/article-pdf/doi/10.1063/5.0024493/14882579/123112_1_online.pdf.

[102] Kutnyakhov, D. *et al.* Time- and momentum-resolved photoemission studies using time-of-flight momentum microscopy at a free-electron laser. *Review of Scientific Instruments* **91**, 013109 (2020). URL https://aip.scitation.org/doi/full/10.1063/1.5118777.

[103] Feibelman, P. J. & Eastman, D. E. Photoemission spectroscopy—correspondence between quantum theory and experimental phenomenology. *Phys. Rev. B* **10**, 4932–4947 (1974). URL https://link.aps.org/doi/10.1103/PhysRevB.10.4932.

[104] Damascelli, A. Probing the electronic structure of complex systems by arpes. *Physica Scripta* **2004**, 61 (2004). URL https://dx.doi.org/10.1238/Physica.Topical.109a00061.

[105] Hüfner, S. *Very high resolution photoelectron spectroscopy*, vol. 715 (Springer, 2007).

[106] Gadzuk, J. W. Surface molecules and chemisorption. ii. photoemission angular distributions. *Phys. Rev. B* **10**, 5030–5044 (1974). URL https://link.aps.org/doi/10.1103/PhysRevB.10.5030.

[107] Liebsch, A. Theory of angular resolved photoemission from adsorbates. *Phys.*

*Rev. Lett.* **32**, 1203–1206 (1974). URL https://link.aps.org/doi/10.1103/PhysRevLett.32.1203.

[108] Scheffler, M., Kambe, K. & Forstmann, F. Angle resolved photoemission from adsorbates: Theoretical considerations of polarization effects and symmetry. *Solid State Communications* **25**, 93–99 (1978). URL https://www.sciencedirect.com/science/article/pii/0038109878903654.

[109] Richardson, N. Comments on angle-resolved photoemission from oriented films of lead phthalocyanine on a cu100 surface. *Chemical Physics Letters* **102**, 390–391 (1983). URL https://www.sciencedirect.com/science/article/pii/0009261483870626.

[110] Bradshaw, A. M. & Woodruff, D. P. Molecular orbital tomography for adsorbed molecules: is a correct description of the final state really unimportant? *New Journal of Physics* **17**, 013033 (2015). URL https://dx.doi.org/10.1088/1367-2630/17/1/013033.

[111] Grobman, W. D. Angle-resolved photoemission from molecules in the independent-atomic-center approximation. *Phys. Rev. B* **17**, 4573–4585 (1978). URL https://link.aps.org/doi/10.1103/PhysRevB.17.4573.

[112] Puschnig, P. *et al.* Orbital tomography: Deconvoluting photoemission spectra of organic molecules. *Phys. Rev. B* **84**, 235427 (2011). URL https://link.aps.org/doi/10.1103/PhysRevB.84.235427.

[113] Dauth, M. *et al.* Angle resolved photoemission from organic semiconductors: orbital imaging beyond the molecular orbital interpretation. *New Journal of Physics* **16**, 103005 (2014). URL https://dx.doi.org/10.1088/1367-2630/16/10/103005.

[114] Ules, T. *et al.* Orbital tomography of hybridized and dispersing molecular overlayers. *Phys. Rev. B* **90**, 155430 (2014). URL https://link.aps.org/doi/10.1103/PhysRevB.90.155430.

[115] Puschnig, P. & Lüftner, D. Simulation of angle-resolved photoemission spectra by approximating the final state by a plane wave: From graphene to polycyclic aromatic hydrocarbon molecules. *Journal of Electron Spectroscopy and Related Phenomena*

**200**, 193 – 208 (2015). URL http://www.sciencedirect.com/science/article/pii/S0368204815001309.

[116] Aquilante, F. *et al.* Molcas 8: New capabilities for multiconfigurational quantum chemical calculations across the periodic table. *Journal of Computational Chemistry* **37**, 506–541 (2016). URL https://onlinelibrary.wiley.com/doi/abs/10.1002/jcc.24221. https://onlinelibrary.wiley.com/doi/pdf/10.1002/jcc.24221.

[117] Krylov, A. I. From orbitals to observables and back. *The Journal of Chemical Physics* **153** (2020). URL https://doi.org/10.1063/5.0018597. 080901, https://pubs.aip.org/aip/jcp/article-pdf/doi/10.1063/5.0018597/15577789/080901_1_online.pdf.

[118] Melania Oana, C. & Krylov, A. I. Dyson orbitals for ionization from the ground and electronically excited states within equation-of-motion coupled-cluster formalism: Theory, implementation, and examples. *The Journal of Chemical Physics* **127** (2007). URL https://doi.org/10.1063/1.2805393. 234106, https://pubs.aip.org/aip/jcp/article-pdf/doi/10.1063/1.2805393/15408065/234106_1_online.pdf.

[119] Ruckenbauer, M., Mai, S., Marquetand, P. & González, L. Photoelectron spectra of 2-thiouracil, 4-thiouracil, and 2,4-dithiouracil. *The Journal of Chemical Physics* **144** (2016). URL https://doi.org/10.1063/1.4941948. 074303, https://pubs.aip.org/aip/jcp/article-pdf/doi/10.1063/1.4941948/14753387/074303_1_online.pdf.

[120] Cederbaum, L. & Zobeley, J. Ultrafast charge migration by electron correlation. *Chemical Physics Letters* **307**, 205–210 (1999). URL https://www.sciencedirect.com/science/article/pii/S0009261499005084.

[121] Dutoi, A. D., Cederbaum, L. S., Wormit, M., Starcke, J. H. & Dreuw, A. Tracing molecular electronic excitation dynamics in real time and space. *The Journal of Chemical Physics* **132** (2010). URL https://doi.org/10.1063/1.3353161. 144302, https://pubs.aip.org/aip/jcp/article-pdf/doi/10.1063/1.3353161/16123918/144302_1_online.pdf.

[122] Hwang, J., Wan, A. & Kahn, A. Energetics of metal–organic interfaces: New experiments and assessment of the field. *Materials Science and Engineering: R: Reports*

**64**, 1–31 (2009). URL https://www.sciencedirect.com/science/article/pii/S0927796X08001228.

[123] Koch, N. Electronic structure of interfaces with conjugated organic materials. *physica status solidi (RRL) – Rapid Research Letters* **6**, 277–293 (2012). URL https://onlinelibrary.wiley.com/doi/abs/10.1002/pssr.201206208. https://onlinelibrary.wiley.com/doi/pdf/10.1002/pssr.201206208.

[124] Whitten, J. & Yang, H. Theory of chemisorption and reactions on metal surfaces. *Surface Science Reports* **24**, 55–124 (1996). URL https://www.sciencedirect.com/science/article/pii/0167572996800045.

[125] Ishii, H., Sugiyama, K., Ito, E. & Seki, K. Energy level alignment and interfacial electronic structures at organic/metal and organic/organic interfaces. *Advanced Materials* **11**, 605–625 (1999).

[126] Franco-Cañellas, A., Duhm, S., Gerlach, A. & Schreiber, F. Binding and electronic level alignment of $\pi$-conjugated systems on metals. *Reports on Progress in Physics* **83**, 066501 (2020). URL https://dx.doi.org/10.1088/1361-6633/ab7a42.

[127] Gerlach, A., Sellner, S., Schreiber, F., Koch, N. & Zegenhagen, J. Substrate-dependent bonding distances of ptcda: A comparative x-ray standing-wave study on cu(111) and ag(111). *Phys. Rev. B* **75**, 045401 (2007). URL https://link.aps.org/doi/10.1103/PhysRevB.75.045401.

[128] Hermann, K. & Bagus, P. S. Localized model for hydrogen chemisorption on the silicon (111) surface. *Phys. Rev. B* **20**, 1603–1610 (1979). URL https://link.aps.org/doi/10.1103/PhysRevB.20.1603.

[129] Deutsch, D., Natan, A., Shapira, Y. & Kronik, L. Electrostatic properties of adsorbed polar molecules: Opposite behavior of a single molecule and a molecular monolayer. *Journal of the American Chemical Society* **129**, 2989–2997 (2007). URL https://doi.org/10.1021/ja068417d. PMID: 17305341, https://doi.org/10.1021/ja068417d.

[130] Abbasi, A. & Scholz, R. Ab initio calculation of the dispersion interaction between a polyaromatic molecule and a noble metal substrate: Ptcda on ag (110). *The Journal of Physical Chemistry C* **113**, 19897–19904 (2009).

[131] Zaitsev, N. L., Nechaev, I. A., Höfer, U. & Chulkov, E. V. Adsorption geometry and electronic properties of flat-lying monolayers of tetracene on the ag(111) surface. *Phys. Rev. B* **94**, 155452 (2016). URL https://link.aps.org/doi/10.1103/PhysRevB.94.155452.

[132] Caplins, B. W., Suich, D. E., Shearer, A. J. & Harris, C. B. Metal/phthalocyanine hybrid interface states on ag(111). *The Journal of Physical Chemistry Letters* **5**, 1679–1684 (2014). URL https://doi.org/10.1021/jz500571z. PMID: 26270366, https://doi.org/10.1021/jz500571z.

[133] Banerjee, J. *et al.* Comparison of the periodic slab approach with the finite cluster description of metal–organic interfaces at the example of ptcda on ag(110). *Journal of Computational Chemistry* **39**, 844–852 (2018). URL https://onlinelibrary.wiley.com/doi/abs/10.1002/jcc.25159. https://onlinelibrary.wiley.com/doi/pdf/10.1002/jcc.25159.

[134] Staemmler, V. *The Cluster Approach for the Adsorption of Small Molecules on Oxide Surfaces*, 219–256 (Springer Berlin Heidelberg, Berlin, Heidelberg, 2005). URL https://doi.org/10.1007/b104404.

[135] Zaitsev, N. L., Nechaev, I. A., Echenique, P. M. & Chulkov, E. V. Transformation of the ag(111) surface state due to molecule-surface interaction with ordered organic molecular monolayers. *Phys. Rev. B* **85**, 115301 (2012). URL https://link.aps.org/doi/10.1103/PhysRevB.85.115301.

[136] Kitamura, M., Imada, T. & Arakawa, Y. Organic light-emitting diodes driven by pentacene-based thin-film transistors. *Applied Physics Letters* **83**, 3410–3412 (2003). URL https://doi.org/10.1063/1.1620676. https://pubs.aip.org/aip/apl/article-pdf/83/16/3410/7827958/3410_1_online.pdf.

[137] Klauk, H. *et al.* High-mobility polymer gate dielectric pentacene thin film transistors. *Journal of Applied Physics* **92**, 5259–5263 (2002). URL https://doi.org/10.1063/1.1511826. https://pubs.aip.org/aip/jap/article-pdf/92/9/5259/10622842/5259_1_online.pdf.

[138] Kitamura, M. & Arakawa, Y. Pentacene-based organic field-effect transistors. *Journal of Physics: Condensed Matter* **20**, 184011 (2008). URL https://dx.doi.org/10.1088/0953-8984/20/18/184011.

[139] Yoo, S., Domercq, B. & Kippelen, B. Efficient thin-film organic solar cells based on pentacene/C60 heterojunctions. *Applied Physics Letters* **85**, 5427–5429 (2004). URL https://doi.org/10.1063/1.1829777. https://pubs.aip.org/aip/apl/article-pdf/85/22/5427/13796428/5427_1_online.pdf.

[140] Yunus, Y. *et al.* Review of the common deposition methods of thin-film pentacene, its derivatives, and their performance. *Polymers* **14** (2022). URL https://www.mdpi.com/2073-4360/14/6/1112.

[141] Chan, W.-L. *et al.* Observing the Multiexciton State in Singlet Fission and Ensuing Ultrafast Multielectron Transfer. *Science* **334**, 1541–1545 (2011). URL https://science.sciencemag.org/content/334/6062/1541.

[142] Congreve, D. N. *et al.* External Quantum Efficiency Above 100% in a Singlet-Exciton-Fission–Based Organic Photovoltaic Cell. *Science* **340**, 334 (2013). URL http://science.sciencemag.org/content/340/6130/334.abstract.

[143] Kunzmann, A. *et al.* Singlet fission for photovoltaics with 130 % injection efficiency. *Angewandte Chemie International Edition* **57**, 10742–10747 (2018). URL https://onlinelibrary.wiley.com/doi/abs/10.1002/anie.201801041.

[144] Grimm, M. *et al.* Molecular orbital imaging beyond the first monolayer: Insights into the pentacene/Ag(110) interface. *Physical Review B* **98**, 195412 (2018). URL https://link.aps.org/doi/10.1103/PhysRevB.98.195412.

[145] Martins, M. *et al.* Monochromator beamline for FLASH. *Review of Scientific Instruments* **77**, 115108 (2006). URL https://aip.scitation.org/doi/abs/10.1063/1.2364148.

[146] Dunning, T. H. Gaussian basis sets for use in correlated molecular calculations. i. the atoms boron through neon and hydrogen. *J. Chem. Phys.* **90**, 1007–1023 (1989).

[147] Pritchard, B. P., Altarawy, D., Didier, B., Gibsom, T. D. & Windus, T. L. A new basis set exchange: An open, up-to-date resource for the molecular sciences community. *J. Chem. Inf. Model.* **59**, 4814–4820 (2019).

[148] Stöhr, M., Van Voorhis, T. & Tkatchenko, A. Theory and practice of modeling van der waals interactions in electronic-structure calculations. *Chem. Soc. Rev.* **48**, 4118–4154 (2019). URL http://dx.doi.org/10.1039/C9CS00060G.

[149] Hume-Rothery, W. & Reynolds, P. A high-temperature debye-scherrer camera, and its application to the study of the lattice spacing of silver. *Proceedings of the Royal Society of London, Series A: Mathematical and Physical Sciences (76,1906-)* **167**, 25–34 (1938).

[150] Momma, K. & Izumi, F. *VESTA3* for three-dimensional visualization of crystal, volumetric and morphology data. *Journal of Applied Crystallography* **44**, 1272–1276 (2011). URL http://dx.doi.org/10.1107/S0021889811038970.

[151] Wang, Y. L. *et al.* Structural evolution of pentacene on a Ag(110) surface. *Physical Review B* **69** (2004). URL https://link.aps.org/doi/10.1103/PhysRevB.69.075408.

[152] Peterson, K. A. & Puzzarini, C. Systematically convergent basis sets for transition metals. ii. pseudopotential-based correlation consistent basis sets for the group 11 (cu, ag, au) and 12 (zn, cd, hg) elements. *Theoretical Chemistry Accounts* **114**, 283–296 (2005).

[153] Peterson, K. A., Figgen, D., Dolg, M. & Stoll, H. Energy-consistent relativistic pseudopotentials and correlation consistent basis sets for the 4d elements Y–Pd. *The Journal of Chemical Physics* **126** (2007). URL https://doi.org/10.1063/1.2647019. 124101, https://pubs.aip.org/aip/jcp/article-pdf/doi/10.1063/1.2647019/13322340/124101_1_online.pdf.

[154] Hauschild, A. *et al.* Molecular distortions and chemical bonding of a large $\pi$-conjugated molecule on a metal surface. *Phys. Rev. Lett.* **94**, 036106 (2005). URL https://link.aps.org/doi/10.1103/PhysRevLett.94.036106.

[155] Duhm, S. *et al.* Pentacene on ag (111): correlation of bonding distance with intermolecular interaction and order. *ACS applied materials & interfaces* **5**, 9377–9381 (2013).

[156] Mercurio, G. *et al.* Adsorption height determination of nonequivalent c and o species of ptcda on ag(110) using x-ray standing waves. *Phys. Rev. B* **87**, 045421 (2013). URL https://link.aps.org/doi/10.1103/PhysRevB.87.045421.

[157] Cordero, B. *et al.* Covalent radii revisited. *Dalton Trans.* 2832–2838 (2008). URL http://dx.doi.org/10.1039/B801115J.

[158] Kokalj, A. Corrosion inhibitors: physisorbed or chemisorbed? *Corrosion Science* **196**, 109939 (2022). URL https://www.sciencedirect.com/science/article/pii/S0010938X21007071.

[159] Bauer, M. & Aeschlimann, M. Dynamics of excited electrons in metals, thin films and nanostructures. *Journal of Electron Spectroscopy and Related Phenomena* **124**, 225–243 (2002). URL http://www.sciencedirect.com/science/article/pii/S0368204802000567.

[160] Halasinski, T. M., Hudgins, D. M., Salama, F., Allamandola, L. J. & Bally, T. Electronic absorption spectra of neutral pentacene (c22h14) and its positive and negative ions in ne, ar, and kr matrices. *The Journal of Physical Chemistry A* **104**, 7484–7491 (2000). URL https://doi.org/10.1021/jp0011544.

[161] Zirzlmeier, J. *et al.* Singlet fission in pentacene dimers. *Proceedings of the National Academy of Sciences* **112**, 5325–5330 (2015). URL https://www.pnas.org/content/112/17/5325. https://www.pnas.org/content/112/17/5325.full.pdf.

[162] Küpper, J. *et al.* X-ray diffraction from isolated and strongly aligned gas-phase molecules with a free-electron laser. *Phys. Rev. Lett.* **112**, 083002 (2014). URL https://link.aps.org/doi/10.1103/PhysRevLett.112.083002.

[163] Rolles, D. *et al.* Femtosecond x-ray photoelectron diffraction on gas-phase dibromobenzene molecules. *Journal of Physics B: Atomic, Molecular and Optical Physics* **47**, 124035 (2014). URL https://dx.doi.org/10.1088/0953-4075/47/12/124035.

[164] Karamatskos, E. T. *et al.* Molecular movie of ultrafast coherent rotational dynamics of ocs. *Nature Communications* **10**, 3364 (2019). URL https://doi.org/10.1038/s41467-019-11122-y.

[165] Baumgärtner, K. *et al.* Multiplex movie of concerted rotation of molecules on a 2d material (2023). 2305.07773.

[166] Cheng, C.-H. *et al.* 1.1$\mu$m near-infrared electrophosphorescence from organic light-emitting diodes based on copper phthalocyanine. *Applied Physics Letters* **88** (2006). URL https://doi.org/10.1063/1.2206678. 213505, https://pubs.aip.org/aip/apl/article-pdf/doi/10.1063/1.2206678/14351802/213505_1_online.pdf.

[167] Hsiao, Y.-S., Whang, W.-T., Suen, S.-C., Shiu, J.-Y. & Chen, C.-P. Morphological control of cupc and its application in organic solar cells. *Nanotechnology* **19**, 415603 (2008). URL https://dx.doi.org/10.1088/0957-4484/19/41/415603.

[168] del Pino Rosendo, E. *et al.* Symmetry-breaking charge transfer and intersystem crossing in copper phthalocyanine thin films. *Phys. Chem. Chem. Phys.* **25**, 6847–6856 (2023). URL http://dx.doi.org/10.1039/D2CP05240G.

[169] Lelu, S., Novat, C., Graillat, C., Guyot, A. & Bourgeat-Lami, E. Encapsulation of an organic phthalocyanine blue pigment into polystyrene latex particles using a miniemulsion polymerization process. *Polymer International* **52**, 542–547 (2003). URL https://onlinelibrary.wiley.com/doi/abs/10.1002/pi.1029. https://onlinelibrary.wiley.com/doi/pdf/10.1002/pi.1029.

[170] Evangelista, F. *et al.* Electronic structure of copper phthalocyanine: An experimental and theoretical study of occupied and unoccupied levels. *The Journal of Chemical Physics* **126** (2007). URL https://doi.org/10.1063/1.2712435. 124709, https://pubs.aip.org/aip/jcp/article-pdf/doi/10.1063/1.2712435/13321952/124709_1_online.pdf.

[171] Stadler, C., Hansen, S., Kröger, I., Kumpf, C. & Umbach, E. Tuning intermolecular interaction in long-range-ordered submonolayer organic films. *Nature Physics* **5**, 153–158 (2009). URL https://doi.org/10.1038/nphys1176.

[172] Nicoara, N., Gómez-Rodríguez, J. M. & Méndez, J. Growth of ptcda films on various substrates studied by scanning tunneling microscopy and spectroscopy. *physica status solidi (b)* **256**, 1800333 (2019). URL https://onlinelibrary.wiley.com/doi/abs/10.1002/pssb.201800333. https://onlinelibrary.wiley.com/doi/pdf/10.1002/pssb.201800333.

[173] Stadtmüller, B., Kröger, I., Reinert, F. & Kumpf, C. Submonolayer growth of cupc on noble metal surfaces. *Phys. Rev. B* **83**, 085416 (2011). URL https://link.aps.org/doi/10.1103/PhysRevB.83.085416.

[174] Coleman, J. N. *et al.* Two-dimensional nanosheets produced by liquid exfoliation of layered materials. *Science* **331**, 568–571 (2011). URL https://www.science.org/doi/abs/10.1126/science.1194975. https://www.science.org/doi/pdf/10.1126/science.1194975.

[175] Jawaid, A. *et al.* Mechanism for liquid phase exfoliation of mos2. *Chemistry of Materials* **28**, 337–348 (2016). URL https://doi.org/10.1021/acs.chemmater.5b04224. https://doi.org/10.1021/acs.chemmater.5b04224.

[176] Huang, S.-M. *et al.* Aspects of symmetry and topology in the charge density wave phase of 1t–tise2. *New Journal of Physics* **23**, 083037 (2021). URL https://dx.doi.org/10.1088/1367-2630/ac1bf4.

[177] Rossnagel, K. On the origin of charge-density waves in select layered transition-metal dichalcogenides. *Journal of Physics: Condensed Matter* **23**, 213001 (2011). URL https://dx.doi.org/10.1088/0953-8984/23/21/213001.

[178] Mathur, N. D. *et al.* Magnetically mediated superconductivity in heavy fermion compounds. *Nature* **394**, 39–43 (1998). URL https://doi.org/10.1038/27838.

[179] Chen, P. *et al.* Charge density wave transition in single-layer titanium diselenide. *Nature Communications* **6**, 8943 (2015). URL https://doi.org/10.1038/ncomms9943.

[180] Mathias, S. *et al.* Self-amplified photo-induced gap quenching in a correlated electron material. *Nature Communications* **7**, 12902 (2016). URL https://doi.org/10.1038/ncomms12902.

[181] Pierloot, K., Dumez, B., Widmark, P.-O. & Roos, B. O. Density matrix averaged atomic natural orbital (ano) basis sets for correlated molecular wave functions. *Theoretica chimica acta* **90**, 87–114 (1995).

[182] de Oteyza, D. G. *et al.* Copper-phthalocyanine based metal–organic interfaces: The effect of fluorination, the substrate, and its symmetry. *The Journal of Chemical Physics* **133**, 214703 (2010). URL https://doi.org/10.1063/1.3509394. https://pubs.aip.org/aip/jcp/article-pdf/doi/10.1063/1.3509394/15433227/214703_1_online.pdf.

[183] Nardi, M. V. *et al.* Electronic properties of cupc and h2pc: an experimental and theoretical study. *Phys. Chem. Chem. Phys.* **15**, 12864–12881 (2013). URL http://dx.doi.org/10.1039/C3CP51224J.

[184] Day, P., Wang, Z. & Pachter, R. Calculation of the structure and absorption spectra of phthalocyanines in the gas-phase and in solution. *Journal of Molecular Struc-*

*ture: THEOCHEM* **455**, 33–50 (1998). URL https://www.sciencedirect.com/science/article/pii/S0166128098002383.

[185] Mastryukov, V., yu Ruan, C., Fink, M., Wang, Z. & Pachter, R. The molecular structure of copper- and nickel-phthalocyanine as determined by gas-phase electron diffraction and ab initio/dft computations. *Journal of Molecular Structure* **556**, 225–237 (2000). URL https://www.sciencedirect.com/science/article/pii/S0022286000006360.

[186] Karlström, G. *et al.* Molcas: a program package for computational chemistry. *Computational Materials Science* **28**, 222–239 (2003). URL https://www.sciencedirect.com/science/article/pii/S0927025603001095. Proceedings of the Symposium on Software Development for Process and Materials Design.

[187] Marom, N., Hod, O., Scuseria, G. E. & Kronik, L. Electronic structure of copper phthalocyanine: A comparative density functional theory study. *The Journal of Chemical Physics* **128** (2008). URL https://doi.org/10.1063/1.2898540. 164107, https://pubs.aip.org/aip/jcp/article-pdf/doi/10.1063/1.2898540/15410743/164107_1_online.pdf.

[188] Haidu, F. *et al.* Transport band gap opening at metal–organic interfaces. *Journal of Vacuum Science & Technology A* **32** (2014). URL https://doi.org/10.1116/1.4882857. 040602, https://pubs.aip.org/avs/jva/article-pdf/doi/10.1116/1.4882857/15987607/040602_1_online.pdf.

[189] Karacuban, H. *et al.* Substrate-induced symmetry reduction of cupc on cu(111): An lt-stm study. *Surface Science* **603**, L39–L43 (2009). URL https://www.sciencedirect.com/science/article/pii/S0039602809001241.

[190] Kröger, I. *et al.* Modeling intermolecular interactions of physisorbed organic molecules using pair potential calculations. *The Journal of Chemical Physics* **135** (2011). URL https://doi.org/10.1063/1.3665923. 234703, https://pubs.aip.org/aip/jcp/article-pdf/doi/10.1063/1.3665923/15446870/234703_1_online.pdf.

[191] Mukherjee, S. *et al.* Hot electrons do the impossible: Plasmon-induced dissociation of h2 on au. *Nano Letters* **13**, 240–247 (2013). URL https://doi.org/10.1021/nl303940z. PMID: 23194158, https://doi.org/10.1021/nl303940z.

[192] Zhang, Y. *et al.* Surface-plasmon-driven hot electron photochemistry. *Chemical Reviews* **118**, 2927–2954 (2018). URL https://doi.org/10.1021/acs.chemrev.7b00430. PMID: 29190069, https://doi.org/10.1021/acs.chemrev.7b00430.

[193] Khurgin, J. B., Petrov, A., Eich, M. & Uskov, A. V. Direct plasmonic excitation of the hybridized surface states in metal nanoparticles. *ACS Photonics* **8**, 2041–2049 (2021). URL https://doi.org/10.1021/acsphotonics.1c00167. https://doi.org/10.1021/acsphotonics.1c00167.

[194] Schönauer, K. *et al.* Charge transfer and symmetry reduction at the cupc/ag(110) interface studied by photoemission tomography. *Phys. Rev. B* **94**, 205144 (2016). URL https://link.aps.org/doi/10.1103/PhysRevB.94.205144.

[195] Smith, D. W. & Day, O. W. Extension of Koopmans' theorem. I. Derivation. *The Journal of Chemical Physics* **62**, 113–114 (2008). URL https://doi.org/10.1063/1.430253. https://pubs.aip.org/aip/jcp/article-pdf/62/1/113/8130439/113_1_online.pdf.

[196] Morrell, M. M., Parr, R. G. & Levy, M. Calculation of ionization potentials from density matrices and natural functions, and the long-range behavior of natural orbitals and electron density. *The Journal of Chemical Physics* **62**, 549–554 (2008). URL https://doi.org/10.1063/1.430509. https://pubs.aip.org/aip/jcp/article-pdf/62/2/549/11359341/549_1_online.pdf.

[197] Morrison, R. C. & Liu, G. Extended koopmans' theorem: Approximate ionization energies from mcscf wave functions. *Journal of Computational Chemistry* **13**, 1004–1010 (1992). URL https://onlinelibrary.wiley.com/doi/abs/10.1002/jcc.540130811. https://onlinelibrary.wiley.com/doi/pdf/10.1002/jcc.540130811.

[198] Davidson, E. R., Ortiz, J. V. & Staroverov, V. N. Complete-active-space extended Koopmans theorem method. *The Journal of Chemical Physics* **155** (2021). URL https://doi.org/10.1063/5.0058080. 051102, https://pubs.aip.org/aip/jcp/article-pdf/doi/10.1063/5.0058080/14111033/051102_1_online.pdf.

[199] Børve, K. J. & Thomas, T. The calculation of initial-state effects on inner-shell ionization energies. *Journal of Electron Spectroscopy and Related Phenomena* **107**,

155–161 (2000). URL https://www.sciencedirect.com/science/article/pii/S0368204800000980.

[200] Kleimann, C., Stadtmüller, B., Schröder, S. & Kumpf, C. Electrostatic interaction and commensurate registry at the heteromolecular f16cupc–cupc interface. *The Journal of Physical Chemistry C* **118**, 1652–1660 (2014). URL https://doi.org/10.1021/jp411289j. https://doi.org/10.1021/jp411289j.

[201] Stadtmüller, B., Henneke, C., Soubatch, S., Tautz, F. S. & Kumpf, C. Tailoring metal–organic hybrid interfaces: heteromolecular structures with varying stoichiometry on ag(111). *New Journal of Physics* **17**, 023046 (2015). URL https://dx.doi.org/10.1088/1367-2630/17/2/023046.

[202] Kröger, I., Stadtmüller, B. & Kumpf, C. Submonolayer and multilayer growth of titaniumoxide-phthalocyanine on ag(111). *New Journal of Physics* **18**, 113022 (2016). URL https://dx.doi.org/10.1088/1367-2630/18/11/113022.

[203] Felter, J., Franke, M., Wolters, J., Henneke, C. & Kumpf, C. Two-dimensional growth of dendritic islands of ntcda on cu(001) studied in real time. *Nanoscale* **11**, 1798–1812 (2019). URL http://dx.doi.org/10.1039/C8NR08943D.

[204] Schöck, M. *et al.* Chiral close-packing of achiral star-shaped molecules on solid surfaces. *The Journal of Physical Chemistry B* **110**, 12835–12838 (2006). URL https://doi.org/10.1021/jp0619437. PMID: 16805577, https://doi.org/10.1021/jp0619437.

[205] Mugarza, A. *et al.* Orbital specific chirality and homochiral self-assembly of achiral molecules induced by charge transfer and spontaneous symmetry breaking. *Phys. Rev. Lett.* **105**, 115702 (2010). URL https://link.aps.org/doi/10.1103/PhysRevLett.105.115702.

[206] Forster, M., Dyer, M. S., Persson, M. & Raval, R. Tailoring homochirality at surfaces: Going beyond molecular handedness. *Journal of the American Chemical Society* **133**, 15992–16000 (2011). URL https://doi.org/10.1021/ja202986s. PMID: 21882841, https://doi.org/10.1021/ja202986s.

[207] Chen, Y. *et al.* Single-molecule insights into surface-mediated homochirality in

hierarchical peptide assembly. *Nature Communications* **9**, 2711 (2018). URL https://doi.org/10.1038/s41467-018-05218-0.

[208] Laurent, G., Lacoste, D. & Gaspard, P. Emergence of homochirality in large molecular systems. *Proceedings of the National Academy of Sciences* **118**, e2012741118 (2021). URL https://www.pnas.org/doi/abs/10.1073/pnas.2012741118. https://www.pnas.org/doi/pdf/10.1073/pnas.2012741118.

[209] Reuner, M. & Popova-Gorelova, D. Attosecond imaging of photoinduced dynamics in molecules using time-resolved photoelectron momentum microscopy. *Phys. Rev. A* **107**, 023101 (2023). URL https://link.aps.org/doi/10.1103/PhysRevA.107.023101.

[210] Wörner, H. J. *et al.* Charge migration and charge transfer in molecular systems. *Structural Dynamics* **4** (2017). URL https://doi.org/10.1063/1.4996505. 061508, https://pubs.aip.org/aca/sdy/article-pdf/doi/10.1063/1.4996505/13838431/061508_1_online.pdf.

[211] Fassioli, F., Dinshaw, R., Arpin, P. C. & Scholes, G. D. Photosynthetic light harvesting: excitons and coherence. *Journal of The Royal Society Interface* **11**, 20130901 (2014). URL https://royalsocietypublishing.org/doi/abs/10.1098/rsif.2013.0901. https://royalsocietypublishing.org/doi/pdf/10.1098/rsif.2013.0901.

[212] Engel, G. S. *et al.* Evidence for wavelike energy transfer through quantum coherence in photosynthetic systems. *Nature* **446**, 782–786 (2007). URL https://doi.org/10.1038/nature05678.

[213] Wang, L., Allodi, M. A. & Engel, G. S. Quantum coherences reveal excited-state dynamics in biophysical systems. *Nature Reviews Chemistry* **3**, 477–490 (2019). URL https://doi.org/10.1038/s41570-019-0109-z.

[214] Breidbach, J. & Cederbaum, L. S. Migration of holes: Formalism, mechanisms, and illustrative applications. *The Journal of Chemical Physics* **118**, 3983–3996 (2003). URL https://doi.org/10.1063/1.1540618. https://pubs.aip.org/aip/jcp/article-pdf/118/9/3983/10850368/3983_1_online.pdf.

[215] Kuleff, A. I., Breidbach, J. & Cederbaum, L. S. Multielectron wave-packet

propagation: General theory and application. *The Journal of Chemical Physics* **123** (2005). URL https://doi.org/10.1063/1.1961341. 044111, https://pubs.aip.org/aip/jcp/article-pdf/doi/10.1063/1.1961341/13644474/044111_1_online.pdf.

[216] Remacle, F. & Levine, R. D. An electronic time scale in chemistry. *Proceedings of the National Academy of Sciences* **103**, 6793–6798 (2006). URL https://www.pnas.org/doi/abs/10.1073/pnas.0601855103. https://www.pnas.org/doi/pdf/10.1073/pnas.0601855103.

[217] Kuleff, A. I., Lünnemann, S. & Cederbaum, L. S. Electron-correlation-driven charge migration in oligopeptides. *Chemical Physics* **414**, 100–105 (2013). URL https://www.sciencedirect.com/science/article/pii/S030101041200095X. Attosecond spectroscopy.

[218] Dutoi, A. D., Wormit, M. & Cederbaum, L. S. Ultrafast charge separation driven by differential particle and hole mobilities. *The Journal of Chemical Physics* **134** (2011). URL https://doi.org/10.1063/1.3506617. 024303, https://pubs.aip.org/aip/jcp/article-pdf/doi/10.1063/1.3506617/13039905/024303_1_online.pdf.

[219] Remacle, F. & Levine, R. D. Attosecond pumping of nonstationary electronic states of lih: Charge shake-up and electron density distortion. *Phys. Rev. A* **83**, 013411 (2011). URL https://link.aps.org/doi/10.1103/PhysRevA.83.013411.

[220] Mignolet, B., Levine, R. D. & Remacle, F. Control of electronic dynamics visualized by angularly resolved photoelectron spectra: A dynamical simulation with an ir pump and xuv attosecond-pulse-train probe. *Phys. Rev. A* **89**, 021403 (2014). URL https://link.aps.org/doi/10.1103/PhysRevA.89.021403.

[221] Kuleff, A. I. & Cederbaum, L. S. Ultrafast correlation-driven electron dynamics. *Journal of Physics B: Atomic, Molecular and Optical Physics* **47**, 124002 (2014). URL https://dx.doi.org/10.1088/0953-4075/47/12/124002.

[222] Calegari, F. *et al.* Charge migration induced by attosecond pulses in bio-relevant molecules. *Journal of Physics B: Atomic, Molecular and Optical Physics* **49**, 142001 (2016). URL https://dx.doi.org/10.1088/0953-4075/49/14/142001.

[223] Lara-Astiaso, M. *et al.* Attosecond pump–probe spectroscopy of charge dynamics in tryptophan. *The Journal of Physical Chemistry Letters* **9**, 4570–4577 (2018). URL https://doi.org/10.1021/acs.jpclett.8b01786. PMID: 30044916, https://doi.org/10.1021/acs.jpclett.8b01786.

[224] Zinchenko, K. S. *et al.* Sub-7-femtosecond conical-intersection dynamics probed at the carbon k-edge. *Science* **371**, 489–494 (2021). URL https://www.science.org/doi/abs/10.1126/science.abf1656. https://www.science.org/doi/pdf/10.1126/science.abf1656.

[225] Nelson, T. R. *et al.* Coherent exciton-vibrational dynamics and energy transfer in conjugated organics. *Nature Communications* **9**, 2316 (2018). URL https://doi.org/10.1038/s41467-018-04694-8.

[226] Rafiq, S. & Scholes, G. D. From fundamental theories to quantum coherences in electron transfer. *Journal of the American Chemical Society* **141**, 708–722 (2019). URL https://doi.org/10.1021/jacs.8b09059. PMID: 30412671, https://doi.org/10.1021/jacs.8b09059.

[227] Arnold, C., Vendrell, O. & Santra, R. Electronic decoherence following photoionization: Full quantum-dynamical treatment of the influence of nuclear motion. *Phys. Rev. A* **95**, 033425 (2017). URL https://link.aps.org/doi/10.1103/PhysRevA.95.033425.

[228] Matselyukh, D. T., Despré, V., Golubev, N. V., Kuleff, A. I. & Wörner, H. J. Decoherence and revival in attosecond charge migration driven by non-adiabatic dynamics. *Nature Physics* **18**, 1206–1213 (2022). URL https://doi.org/10.1038/s41567-022-01690-0.

[229] Jenkins, A. J., Vacher, M., Twidale, R. M., Bearpark, M. J. & Robb, M. A. Charge migration in polycyclic norbornadiene cations: Winning the race against decoherence. *The Journal of Chemical Physics* **145** (2016). URL https://doi.org/10.1063/1.4965436. 164103, https://pubs.aip.org/aip/jcp/article-pdf/doi/10.1063/1.4965436/13766007/164103_1_online.pdf.

[230] Despré, V. *et al.* Attosecond hole migration in benzene molecules surviving nuclear motion. *The Journal of Physical Chemistry Letters* **6**, 426–431 (2015). URL

https://doi.org/10.1021/jz502493j. PMID: 26261959, https://doi.org/10.1021/jz502493j.

[231] Kowalewski, M., Bennett, K., Dorfman, K. E. & Mukamel, S. Catching conical intersections in the act: Monitoring transient electronic coherences by attosecond stimulated x-ray raman signals. *Phys. Rev. Lett.* **115**, 193003 (2015). URL https://link.aps.org/doi/10.1103/PhysRevLett.115.193003.

[232] Popova-Gorelova, D. & Santra, R. Imaging interatomic electron current in crystals with ultrafast resonant x-ray scattering. *Phys. Rev. B* **92**, 184304 (2015). URL https://link.aps.org/doi/10.1103/PhysRevB.92.184304.

[233] Hollstein, M., Santra, R. & Pfannkuche, D. Correlation-driven charge migration following double ionization and attosecond transient absorption spectroscopy. *Phys. Rev. A* **95**, 053411 (2017). URL https://link.aps.org/doi/10.1103/PhysRevA.95.053411.

[234] Despré, V., Golubev, N. V. & Kuleff, A. I. Charge migration in propiolic acid: A full quantum dynamical study. *Phys. Rev. Lett.* **121**, 203002 (2018). URL https://link.aps.org/doi/10.1103/PhysRevLett.121.203002.

[235] Yuan, K.-J. & Bandrauk, A. D. Ultrafast x-ray photoelectron imaging of attosecond electron dynamics in molecular coherent excitation. *The Journal of Physical Chemistry A* **123**, 1328–1336 (2019). URL https://doi.org/10.1021/acs.jpca.8b12313. PMID: 30669842, https://doi.org/10.1021/acs.jpca.8b12313.

[236] Inhester, L., Greenman, L., Rudenko, A., Rolles, D. & Santra, R. Detecting coherent core-hole wave-packet dynamics in N2 by time- and angle-resolved inner-shell photoelectron spectroscopy. *The Journal of Chemical Physics* **151** (2019). URL https://doi.org/10.1063/1.5109867. 054107, https://pubs.aip.org/aip/jcp/article-pdf/doi/10.1063/1.5109867/9666099/054107_1_online.pdf.

[237] Khalili, K. *et al.* Simulation of time-resolved x-ray absorption spectroscopy of ultrafast dynamics in particle-hole-excited 4-(2-thienyl)-2,1,3-benzothiadiazole. *Structural Dynamics* **7** (2020). URL https://doi.org/10.1063/4.0000016. 044101, https://pubs.aip.org/aca/sdy/article-pdf/doi/10.1063/4.0000016/13838570/044101_1_online.pdf.

[238] Mauger, F. m. c. *et al.* Charge migration and attosecond solitons in conjugated organic molecules. *Phys. Rev. Res.* **4**, 013073 (2022). URL https://link.aps.org/doi/10.1103/PhysRevResearch.4.013073.

[239] Heinecke, E., Hartmann, D., Müller, R. & Hese, A. Laser spectroscopy of free pentacene molecules (I): The rotational structure of the vibrationless S1←S transition. *The Journal of Chemical Physics* **109**, 906–911 (1998). URL https://doi.org/10.1063/1.476631. https://pubs.aip.org/aip/jcp/article-pdf/109/3/906/10795069/906_1_online.pdf.

[240] Grimme, S. & Parac, M. Substantial errors from time-dependent density functional theory for the calculation of excited states of large $\pi$ systems. *ChemPhysChem* **4**, 292–295 (2003). URL https://chemistry-europe.onlinelibrary.wiley.com/doi/abs/10.1002/cphc.200390047. https://chemistry-europe.onlinelibrary.wiley.com/doi/pdf/10.1002/cphc.200390047.

[241] Coto, P. B., Sharifzadeh, S., Neaton, J. B. & Thoss, M. Low-lying electronic excited states of pentacene oligomers: A comparative electronic structure study in the context of singlet fission. *Journal of Chemical Theory and Computation* **11**, 147–156 (2015). URL https://doi.org/10.1021/ct500510k. PMID: 26574213, https://doi.org/10.1021/ct500510k.